ABSTRACT

Title of Document: NANOELECTRONIC MATERIALS

Tracy Lyons Moore, Doctor of Philosophy, 2010

Directed By: Professor Ellen D Williams, Physics Department

This thesis explores fabrication methods and characterization of novel materials used in field effect transistors, including metallic nanowires, carbon nanotubes, and graphene.

Networks of conductive nanotubes are promising candidates for thin film electrode alternatives due to their desirable transparency, flexibility, and potential for large-scale processing. Silver nanowire and carbon nanotube networks are evaluated for their use as thin film electrode alternatives. Growth of silver nanowires in porous alumina membranes, dispersion onto a variety of substrates, and patterning is described. Metallic carbon nanotubes are suspended in aqueous solutions, airbrushed onto substrates, and patterned. The conductivity and transparency of both networks is evaluated against industry standards.

Graphene is a two dimensional gapless semimetal that demonstrates outstanding room temperature mobilities, optical transparency, mechanical strength, and sustains large current densities, all desirable properties for semiconductors used

in field effect transistors. Graphene's low on/off ratio and low throughput fabrication techniques have yet to be overcome before it becomes commercially viable.

Silicon oxide substrates are common dielectrics in field effect transistors and instrumental in locating mechanically exfoliated graphene. The morphology of two different silicon oxides have been studied statistically with atomic force microscopy and scaling analysis. Tailoring the physical properties of these substrates may provide a control of graphene's electrical properties.

A silicon oxide substrate may also be chemically altered to control the properties of graphene. I have modified silicon oxide with self-assembled monolayers with various terminal groups to control the field near the graphene. I characterize the monolayers with atomic force microscopy, x-ray photospectroscopy, and contact angles. I characterize graphene on these substrates using Raman microscopy and transport measurements.

Finally, I examine low frequency noise in graphene field effect transistors on conventional silicon oxide substrates. As devices become smaller, the signal to noise ratio of these devices becomes important. Low frequency noise occurs on long time scales and must be controlled for device stability. I measure novel behavior of low frequency noise in multiple graphene devices. The noise may be described electron-hole puddles in the graphene that are caused by trapped charges near the surface of silicon oxide.

NANOELECTRONIC MATERIALS

By

Tracy L Moore

Dissertation submitted to the Faculty of the Graduate School of the
University of Maryland, College Park, in partial fulfillment
of the requirements for the degree of
Doctor of Philosophy
2010

Advisory Committee:
Professor Ellen D Williams, Chair
Professor Michael Fuhrer
Professor Janice Reutt-Robey
Professor Robert Anderson
Assistant Professor John Cumings

Dedication

To my parents Karen and Ed Moore, my brother David Moore, and Tommy Willis for their constant support.

Acknowledgements

I am grateful to Professor Ellen Williams for her guidance throughout my graduate career. She has provided me with support, encouragement, and wisdom both personally and professionally. She advised me in determining research projects, connected me to professional contacts, and helped me locate a physician. Her compassion and knowledge helped me decide to attend the University of Maryland and guided me through the completion of my research.

I also thank Professor Michael Fuhrer for his time and for the use of his lab facilities. His assistance with my study of low frequency noise played an instrumental role in helping me describe this difficult phenomenon. His knowledge of graphene is vast and discussions with him have helped me get through many research hurdles.

Dr. Enrico Rossi has also graciously provided me with exclusive access to the results of his theoretical simulations. Many experimentalists would have benefited from these results and I am grateful for his help and kindness. Throughout my graduate career both Dr Vince Ballarotto and Dr. Dan Hines have been willing to offer ideas, edit documents, and help me practice presentations with short notice.

I also appreciate the support and sacrifices made by my close friends Jackie Skapik, Sarah Zehner, and Andrew Tunnell. Their material possessions, time, and sympathy were given to me freely and regularly. I also thank my friends Charles Ruggiero, Renae Irvine, and Mariel Kerr.

My classmates and friends Andrew Pomerance, Matt Beeler, Nick and Shaela Mecholsky, Joe Tuggle, Ken Griggs, and my first friend at Maryland, Dan Lenski, have made life more fun in addition to helping me with classwork. My labmate Vinod

Sangwan assisted me with experiments and made time in the lab more enjoyable. I have enjoyed the company of Mihaela Ballarotto and appreciated her insights.

I am grateful to so many labmates and colleagues who shared knowledge with me and cut down my research struggles including David Tobias, Chenggang Tao, Jianhao Chen, Brad Conrad, Mahito Yamamoto, Liang Li, Adrian Southard, Sungjae Cho, Shudong Xiao, Chaun Jang, Alexandra Curtin, Enrique Cobas, Masa Ishigami, Michelle Groce, Kristen Burson, and Jake Tosado. I also appreciate the support of Margaret Lukomska, Linda O'Hara, and Jane Hessing.

Table of Contents

List of Tables

List of Figures

Chapter 1: Introduction

Nanomaterials are materials that have physical dimensions on the order of a nanometer. These materials have a high ratio of surface area to bulk compared to this ratio in conventional materials. Often, a nanomaterial will demonstrate unique behaviors caused exclusively by its physical size. For example, nanomaterials such as fullerenes, carbon nanotubes, or graphene all behave electrically and physically differently from their parent graphite. Graphene is classified as a semimetal while carbon nanotubes are semiconducting or metallic and bulk graphite is also a semimetal, but with a different band structure than graphene. Large surface area makes such materials ideal for certain applications including chemical sensing.

Nanomaterials have been researched heavily for years and are now becoming implemented in a variety of applications. Nanowire arrays were being fabricated from a variety of semiconductors and metals beginning in the early 90's. Carbon nanotubes were fabricated by carbon vapor deposition in the early 90's as well. Quantum dots for quantum computing applications were being made in the 80's. And, most recently, a single layer of graphite, labeled graphene, was controllably isolated in 2004.

The recently established national nanotechnology initiative lists 25 government agencies that are involved in research on some nanotechnology topic[1]. Furthermore, they outline nanotechnology applications that will impact clean energy and water, pollution reduction, and improved materials[1]. Some examples of nanotechnology applications are include drug delivery by carbon nanotubes, graphene for efficient alternative energy storage ultracapacitors, graphene for low power

consumption fast circuit components, and nanorust for removing arsenic from water[1]. Even new policies are being discussed to regulate the applications of these nanotechnologies and their effects on the environment[2].

This dissertation investigates a variety of novel nanomaterials for their use as electrode or semiconductor alternatives in electronic devices like thin film field effect transistors. Some desirable properties for future transistors include transparency, flexibility, and small size. Nanomaterials including silver nanowires, carbon nanotubes, and graphene were fabricated and their physical and electrical properties were measured.

Metallic nanowires and carbon nanotubes were studied for their possible use as electrodes in flexible thin film transistors. Silver nanowires were grown electrochemically in porous alumina membranes. Membranes were dissolved yielding suspensions on nanowires in water. Nanowires were dispersed onto transparent substrates including glass and different plastics. The resistance as a function of nanowire network concentration, or optical transparency, was measured. Commercially available metallic carbon nanotubes were also suspended in water-based solutions using soaps and polymers as suspending agents. Suspensions were also dispersed onto transparent substrates such as glass and plastic. Some suspending agents interfere with electrical conduction. Finally the resistance as a function of bending radius was measured for the nanotube networks suspended on plastics. I found that carbon nanotube networks have lower resistance for similar network transparency to silver nanorwires. Furthermore, carbon nanotube networks are flexible; network resistance barely changes up to small bending radii.

The morphology of silicon oxide substrates has also been statistically studied for the silicon oxide's use as dielectrics in thin film field effect transistors. Typically in a field effect transistor, the semiconductor is deposited on top of the dielectric so the dielectric morphology will affect the interface between the dielectric and the semiconductor, and, in some cases, the morphology of the semiconductor as well. Atomic force microscope images of the oxide surface were taken in ambient conditions and height-height correlation functions were computed. Commercially available thermally deposited silicon oxide as well as an ultra-thin oxide were studied. I found that controlling the density of steps on the ultra-thin oxide may provide a means of controlling the morphology of the atomically thin semimetal graphene.

Next, I review background information pertaining to graphene. Since its experimental realization in 2004, graphene research has flooded the literature. Graphene's band structure and unique raman spectrum are explained. Finally, certain graphene research is highlighted including research related to charged-impurity scattering in graphene.

I describe my research with the goal of separating graphene from the silicon oxide substrate on which it is almost exclusively exfoliated and studied. I achieved this goal by depositing a self-assembled monolayer on the silicon oxide before exfoliation of graphene on this surface. This procedure allowed the thin film interfere condition that maximizes graphene contrast on certain substrates to be retained, while altering the chemical properties of the silicon oxide substrate. The morphologies of the self-assembled monolayers were studied with atomic force microscopy and

height-height correlation functions as well as contact angle measurements and x-ray photospectroscopy. Graphene was mechanically exfoliated on these monolayers. On some monolayers, graphene's raman spectrum was altered in a similar manner to the spectrum of heavily doped graphene. Finally, transport measurements were found to exhibit little variation over a wide temperature range.

Lastly, I have measured low-frequency noise in graphene field effect transistors. Low frequency noise is important for long time scale behavior of electronic components. Low frequency noise is traditionally described by Hooge's empirical law; no satisfactory universal explanation of this behavior has been provided. I have measured low-frequency noise behavior in multiple four-probe graphene devices. Noise measured at low carrier densities deviates from Hooge-like behavior. A model of charged impurities on the graphene describe the measured results well.

Chapter 2: Nanowire and Carbon Nanotube Networks for Use as Transfer Printed Electrodes

Thin Film Transistors (TFTs) are currently used in sensors, micro electro mechanical systems, and electronic displays. Speed, size, and power consumption optimization of TFTs is a topic of current interest[3]. Flexible and transparent electronics are also being studied for their potential applications including flat panel displays, radio frequency IDs, and e-paper.

Many groups have considered assembly and conduction issues for metallic (and semiconducting) nanowires. In order to study the electrical properties of nanowires they must have electric contacts. Assembly concerns are varied as nanowires may be grown in many different manners, some more conducive to assembly than others. For example, palladium wires may be grown between two photolithographically defined palladium electrodes as demonstrated by Cheng *et al.*, resulting in single nanowires in well defined locations[4]. Another approach that yields single nanowires in precise locations is electrochemical growth or evaporation[5] along the sidewall of a photoresist pattern. Some assembly attempts include chemical patterning of a substrate to selectively promote/discourage adhesion[6], contacting individual wires with precisely placed electrodes using a focused ion/electron beam deposition technique[7], and generating dielectrophoretic forces on nanowires in solution[8,9]. Modeling of the behavior of nanowires under dielectrophoretic forces has also been performed by Liu *et al.*[10]. In our study, the placement and orientation of

individual nanowires was not controlled. Instead, a random network of nanowires was drop cast from solution and the network was patterned later.

The electrical properties of Au nanowires have also been investigated by many of the same groups that study methods for assembling and contacting these wires. Valizadeh *et al.*[7] and Smith *et al.*[8] measured I-V characteristics for a single Au nanowire in order to determine the resistivity of the wire. Valizadeh *et al.* deposited Pt contacts at four separate points on a single 200 nm diameter wire using focused ion/electron beam deposition and determined the wire resistivity to be ~2.9 x 10^{-6} Ωm , two orders of magnitude worse than bulk Au[7]. Smith *et al.*. evaporated Ti contacts onto individual 350 nm diameter wires after positioning these wires with dielectrophoretic forces and performed many measurements on individual nanowires of different lengths of the resistance between the ends of each nanowire[8]. They then calculated the resistivity of a single Au nanowire to be ~2.9 x 10^{-8} Ωm by plotting the resistance as a function of length and multiplying by the cross-sectional area of the wire. This resistivity is comparable to that of bulk Au. Smith *et al.* also determined the resistivity of 70 nm diameter Au nanowires to be ~4.5 x 10^{-8} Ωm in the same manner[8]. Boote *et al.* measured the resistance of individual 175 nm diameter, 4 μm long Au nanowires to be 35 Ω per wire[9]. Furthermore, they determined the "melting point" of these Au nanowires, the point at which they no longer conduct, to be 6.5 mA[9]. The use of a metallic nanowire with a sub 30 nm diameter has even been used as the active channel of a MOSFET[11]. The study reported here investigates the resistivity of a network of nanowires.

The feasibility of using conducting silver nanowire networks and airbrushed carbon nanotube networks as electrodes in TFTs printed onto plastic substrates has been investigated. To accomplish this, silver nanowires with diameters of 200 nm and lengths of 10 microns have been fabricated electrochemically in porous alumina membranes. During fabrication, the nanowire crystallinity was considered and methods for achieving the highest degree of crystallinity were studied and employed. Networks of these nanowires were drop cast and printed into polyethylene terephthalate (PET) in controllable patterns. The conductance of these networks as a function of network concentration and elemental surface composition has been measured. Alternately, commercially available metallic carbon nanotubes were airbrushed onto silicon oxide substrates and printed onto plastics. Nanowire/tube networks are advantageous compared to conventional solid thin film electrodes because they will cause fewer, smaller stress patterns when printed onto plastic substrates. Our measurements indicate nanowire networks will also have slightly higher power consumption due to a maximum conductance that is half the conductance of Molybdenum Tungsten (MoW), the current industry standard for thin film transistor liquid crystal displays[3].

2.1 Ag Nanowire Growth

A review of electrochemical deposition and the literature concerning single crystal nanowires was used as the basis for developing the nanowire fabrication process, and is presented here. Factors affecting, and techniques for measuring, the conductance of a metal are reviewed, and the relationship to power consumption is

presented. Finally, a brief review of the XPS experimental technique used to study the elemental surface composition of the nanowires is given.

2.1.1 Electrochemistry Background

The silver nanowires used to make these networks were fabricated electrochemically in alumina template pores. Electrochemical deposition is the process by which an element is removed from a solution and deposited on a conducting substrate[12].

A basic electrochemical cell consists of a battery or power source and two conducting electrodes in contact with an electrolytic chemical solution. The electrode upon which one or more component(s) of the solution will deposit is the working electrode, the other is the common, or counter electrode. The common electrode may give metal ions or electrons to the solution depending on its composition. If an inert metal such as platinum is used as the common electrode, only electrons are exchanged with the electrolytic solution and reduction or oxidation of ions in the solution is the result[12]. A given electrochemical cell will therefore have a specific equilibrium potential (between the two electrodes) that depends upon the electrodes used, the chemical composition of the solution, the temperature and the concentration of the solution. This equilibrium potential may be calculated by the Nernst equation,

$$E = E_0 + \frac{RT}{zF} \ln \frac{[Ox]}{[Red]}, \qquad (2.1)$$

where R is the gas constant, T is the temperature, z is the number of electrons involved in the reaction, F is the Faraday number, and [Ox] ([Red]) is the activity of the oxidized (reduced) product in the solution, which may be approximated by its

concentration[12]. E_0 is the standard electrode potential, a measured quantity which depends on solution and electrode compositions and may be found in many electrochemistry reference texts[12].

When a potential greater than the equilibrium potential is applied to an electrochemical cell, a current will flow through the cell and the deposition of material from the electrolytic solution may occur[12]. The overpotential, η, is the difference between the amount of potential resulting in current flow, *E(I)*, and the equilibrium potential, E,

$$\eta = E(I) - E\,. \tag{2.2}$$

There are four processes involved in the current flow that may be effected by this overpotential; charge transfer, diffusion, chemical reaction, and crystallization[12]. In addition to understanding the electrochemical cell and all its components, an understanding of the deposition mechanism is required to control the crystallinity of deposit. Nucleation and growth are the primary deposition mechanisms.

Nucleation on the working electrode is governed by the equation:

$$N = N_0(1 - e^{-At})\,, \tag{2.3}$$

where N_0 is the total number of possible nucleation sites, A is the nucleation rate constant, and t is time[12]. The two limits of this equation are $N \cong N_0$, the case of instantaneous nucleation at every site, and $N \cong A \cdot N_0 \cdot t$, the case where N grows as a function of time, referred to as progressive nucleation[12]. The growth of these nuclei is also of interest because a complete description of deposition depends on both these phenomena and their interaction. Multiple growth models, both 2D and 3D, exist and the rate of growth of each is distinct. Simultaneous nucleation and growth may occur.

The overall current-time relationship will then depend on these descriptions which are complicated by overlapping growth from different nuclei[12]. Deposition of perfect crystalline layers depends on the variables that affect the nucleation and growth rates like the total time of the deposition, the size and weight of an adatom, and the concentration of the ions in solution. More crystalline deposition is achieved if the electrochemical solution is heated and stirred and at a low overpotential[12].

Two groups have reported fabrication of single-crystal silver nanowires using different electrochemical deposition conditions and recipes. Sauer *et al.*. reported that a deposition pulse followed by a pulse of the opposite charge, which discharges the double layer, is essential to create single-crystal wires. The necessary pulse shapes are shown in Fig. 2.1, reproduced from Sauer *et al.*.[13]

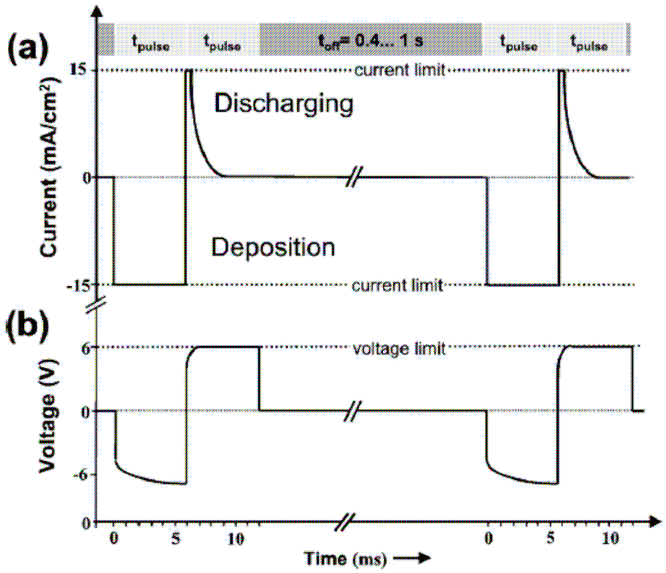

Figure 2.1: Pulse parameters used by Sauer *et al*. to yield single crystal silver nanowires. Taken from reference[13].

Later, Wang *et al.*. fabricated single-crystal silver, copper, and gold nanowires with a specific, constant, low overpotential[14]. They observed a 2D nucleation and growth mechanism at these overpotentials. The degree of crystallinity of the resulting

nanowires depended on their, uncontrollable, direction of growth[14]. Single crystal nanowires result from growth in the [100] and [110] directions, whereas primary or secondary twin defects or stacking defects were observed for growth in all other directions[14].

2.1.2 Nanowire Fabrication

Nanowires were fabricated via electrochemical deposition into commercially available anodic aluminum oxide membrane pores. The resulting wires were extracted from the membranes and drop cast onto silicon to form networks and these were printed into PET. The conductance of these networks was measured before and after printing and during the printing process.

An electrochemical cell was prepared by affixing a working electrode to a commercially available membrane and selecting a suitable counter electrode. Nanowires were fabricated using many different deposition parameters guided by the literature discussed above. The technique by which the nanowires were harvested was varied to try to control the surface composition of the nanowires.

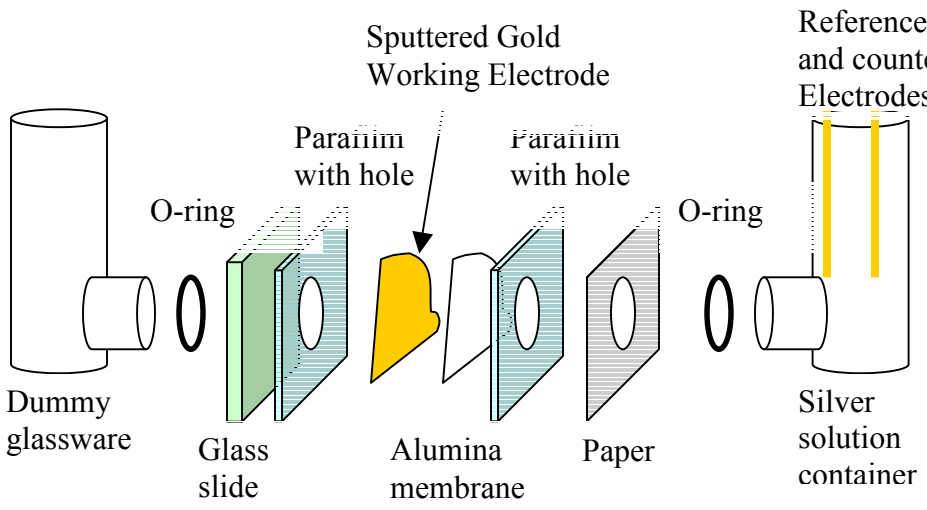

Figure 2.2: Cartoon of experimental setup of the electrochemical cell used. Heat was used to attach from the glass slide to the paper and a metal clamp was used to hold the glassware and o-rings in place around the membrane.

A schematic drawing of the experimental electrochemical cell is shown in Fig 2.2. A thin layer of gold was sputtered onto Whatman commercial alumina membranes with pore diameters of 200 nm. Sputtering was performed in an AJA sputterer or Denton desk vacuum II at 5-50x10^{-3} Torr at a rate of 50 nm per minute. Evaporation is not a suitable technique for creating a gold film on an alumina template because, as observed using an SEM, the evaporated gold will not cover the membrane pores.

Next, the membrane was encased in parafilm as shown in Figure 2.2 to allow leak-proof contact with a silver solution. This was accomplished by folding a parafilm square into fourths and punching a hole through the folded parafilm using a die and punch set. The brittle 25mm diameter membrane was then quartered and one quarter was lightly placed in the middle of the four layers of parafilm. A slender piece of folded copper tape, used to make an electrical contact to the gold film, was

positioned to extend beyond the length of the parafilm. A hole of the same size was made in a piece of plain paper using the die and punch set. The parafilm and membrane were placed on top of a glass slide with the gold covered side of the membrane facing the glass slide. The paper with hole was aligned with the hole on the other side of the parafilm and a glass slide was placed over this side as well. The whole sandwich was heated using a heat gun while pressure was applied to it until the parafilm wet the glass surface. The sandwich was flipped over and the heating with pressure was performed again. Upon cooling, only the glass slide that was in contact with the paper could be removed from the sandwich, the result is pictured in Fig. 2.3 a). This structure was then clamped between two specially made pieces of glassware like the one shown in Fig. 2.3 b) with o-rings to help seal as shown in Fig. 2.3 c).

(a) (b) (c)

Figure 2.3: Electrochemical cell and individual components are shown. a) Alumina membrane that has been surrounded by parafilm and stabilized by a glass slide (not visible). Copper tape makes electrical contact to the working electrode gold film on the opposite (not visible) side of the membrane. b) specialty glassware. c) Complete electrochemical cell including common electrode and potentiostat connections.

The electrochemical cell was made in the specialty glassware using silver solution and two 4mm by 20mm pieces of Alpha Aesar platinum sheet as the counter and reference electrodes. These electrodes were isolated from each other with tubular pieces of plastic cut from pipette tips. A potentiostat was used to control the

electrochemical reaction performed between the counter, reference, and working (sputtered gold film) electrodes.

Three different silver solutions were investigated with different electrochemical deposition conditions. The first silver solution was $AgNO_3$ and sulfuric acid H_2SO_4. Nanowires were deposited when a constant voltage of -0.6 V was applied to the working electrode. The crystallinity of these wires was not measured, but they are believed to demonstrate a very low degree of crystallinity. A second silver solution was made according to Sauer[13]. A 105 g/l solution of potassium thiocyanate (KSCN) was made by stirring with a stirring rod and heating to approximately 40 degrees. When the KSCN was dissolved, 8.5 g/l of silver sulfate was added to the solution, while stirring and heating was continued. This solution was left stirring and heated overnight, until the silver sulfate was dissolved. Finally 200 g/l ammonium citrate was added under the same conditions to adjust the ph of the solution to 4.5 (as reported by reference)[13]. The final silver solution used to deposit nanowires was made by adding 2% Difco gelatin by weight to a commercial silver bath solution, 1025 RTU, made by Technic Inc. Then the solution was diluted with water according to the ratio 1:1. To dissolve the gelatin it was necessary to heat to approximately 50 ° C and stir the solution.

Three different pulse configurations were used to deposit nanowires into the membranes from the solution as described by Sauer *et al*.[13]. However, the most crystalline wires were produced by deposition with a constant voltage (Sample U), described in more detail in section 2.1.4. Sample U was used for the remainder of the work discussed in this chapter.

The nanowires were harvested from the membrane in which they were grown by cracking the brittle membrane into pieces and dissolving those pieces in a 3M sodium hydroxide solution for 10 minutes. The sodium hydroxide was decanted, taking care not to remove the wires, and the vial containing the remaining wires was refilled with water. The wires attached to the gold film (working electrode) were sonicated in solution to disperse them. Then the vials were put in a centrifuge at 6000 rpm for 2 minutes to separate the wires from the water in which they were suspended. The water was removed with a pipette and fresh water was put in the vial. The wires were rinsed three times in this manner.

Some samples were also etched with 5 $x10^{-4}$ M potassium cyanide (KCN) solution. The water was decanted from these samples after centrifugation and the KCN solution was added. The wires were agitated by sonication at 2 minute intervals and then centrifuged again after 10 minutes and the KCN was removed. The wires were rinsed 3 times as described previously.

2.1.3 Nanowire Characterization

Some nanowires were fabricated under pulsed conditions when the duration and magnitude of the positive and negative pulse were not identical. “Modular galvano” mode was used to make a negative constant current pulse and then make a positive linearly decreasing current pulse. The conditions used for this setting were -10 mA negative current for 0.1 s, then 10 mA decreasing at -6 mA/s to 0 mA, finally a rest time of 0.5 s (sample N in Table 2.1). Other depositions were made with the same pulse shape and different parameter values. These depositions are shown in Table 2.1. The opposite modular galvano values used for sample N were also used (a

positive current and then an increasing negative current), and will be referred to as sample M. Deposition condition O was also used while heating the solution to 45 degrees C during deposition, labeled sample R. Also some of the product of samples N and O were annealed at 385 degrees C, while still in their alumina template. These will be referred to as samples S and T respectively.

Sample Label	Negative *I* (mA)	Duration of Neg *I* (ms)	Positive *I* (mA)	*dI/dt* (mA/ms)	Rest Time
N	-10	100	10	-1.7	0.5
O	-10	6	10	-1.7	0.6
P	-10	30	10	-25	0.6
Q	-10	150	10	-12.5	0.6

Table 2.1: Modular Galvano electrodeposition parameters for multiple depositions.

The commercial silver solution was deposited into membrane pores in chronoamperometry mode using a potential of -1.2 V for 2 minutes and followed by a potential of -0.9 V for 10 minutes. This will be referred to as sample U. Many depositions were performed at the sample U deposition conditions and these nanowires were used in the remainder of the work discussed in this paper.

All fabrication attempts alternating identical positive and negative voltage or current pulses did not yield nanowires. Samples N-U, fabricated with modular galvano or a constant overpotential, are shown in Fig. 2.4. For the silver sulfate solution, shorter pulses result in more uniform wires. Deposition parameters (rate) had less effect than solution composition; the commercially made silver solutions yielded uniform, long nanowires.

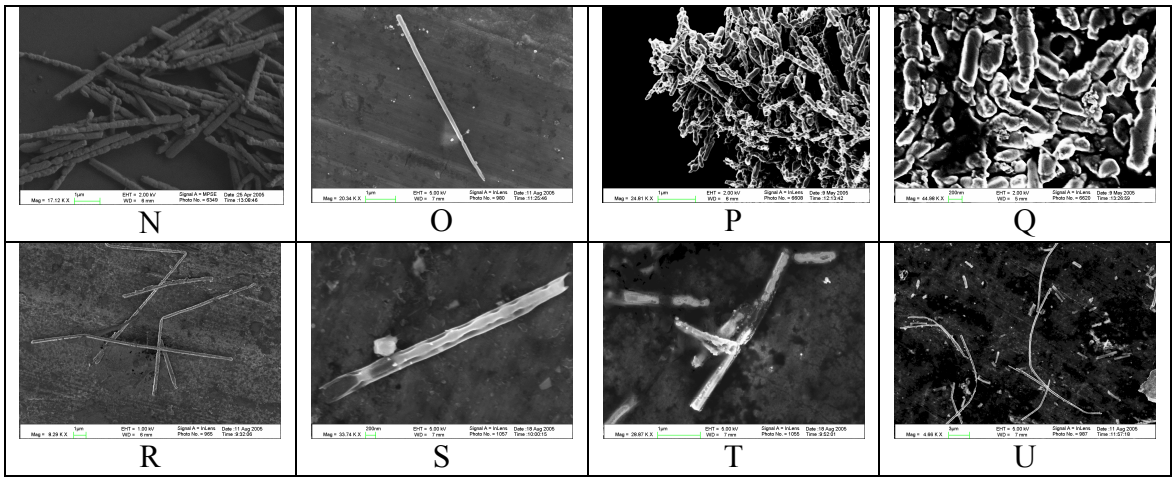

Figure 2.4: Scanning electron microscope images of nanowires grown using different solutions and deposition conditions.

Some of the previous samples were etched in KCN after harvesting from alumina membrane by NaOH dissolution. These KCN etched wires are shown in Fig. 2.5. Electron diffraction patterns were taken of these KCN etched wires with a transmission electron microscope (TEM). An electron diffraction pattern of sample U (Fig. 2.6) is identical to diffraction patterns reported by Wang *et al.*. Therefore, sample U is probably single crystal with twin boundaries by comparison with Wang.

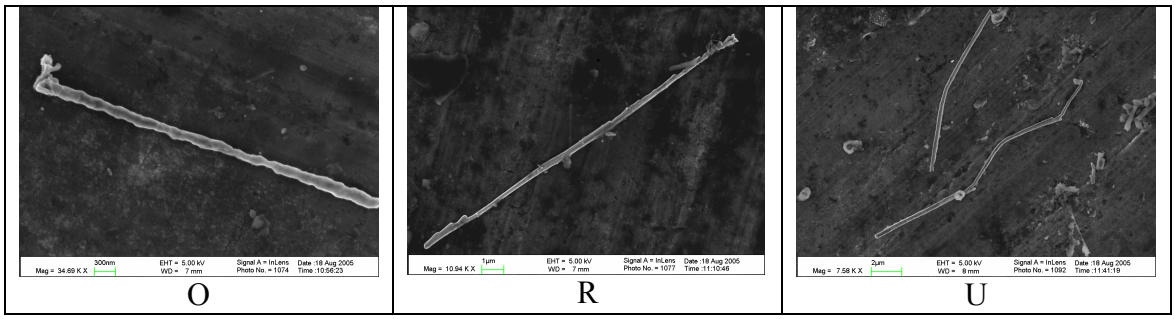

Figure 2.5: Samples O, R, and U after a 10 minute etch in KCN solution.

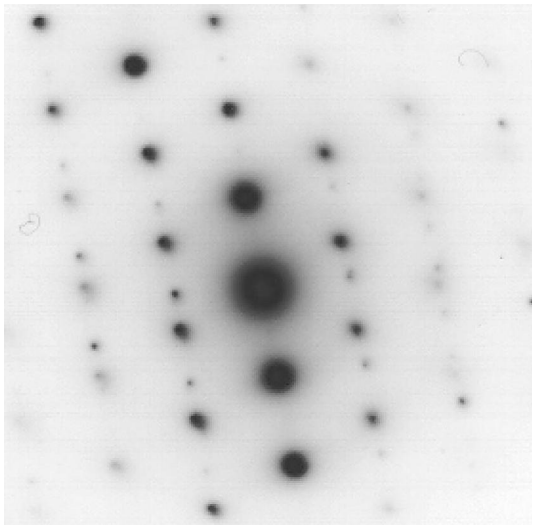

Figure 2.6: Electron diffraction pattern of sample U acquired with a TEM.

X-ray photoelectron spectroscopy (XPS) was performed on sample U before etching and after etching for a number of different NaOH exposure times. The Kratos axis 165 spectrometer was used to perform these measurements with a magnesium K-alpha x-ray source and a power of 250 watts. The sample holders, onto which the nanowires were drop cast directly, were made of stainless steel. A sample depth of approximately 8 nm was probed. The silver binding energy lines that were analyzed were the 367 eV and 373 eV lines corresponding to Ag *3d 5/2* and Ag *3d 3/2* electrons.

XPS studies were performed by the University of Maryland, College Park Department of Chemistry and Biochemistry XPS facility to compare the KCN etched and the unetched (NaOH dissolution only) wires. Elements detected by the scan were oxygen, carbon, aluminum, and silver. The XPS substrates were stainless steel so silver and aluminum signals were not caused by the stainless steel sample holder and it may be concluded that both are present on the wire surface. The atomic concentration of silver atoms was determined and the results are shown in Table 2.2.

The function of the NaOH exposure is to remove the aluminum oxide membrane in which the wires were deposited. The purpose of the KCN exposure is to clean all other elements off the surface of the wires after dissolution of the membrane by stripping the outer layers of silver from the wires. We found that the amount of silver on the surface of the wires depends on the amount of time the wires are left in the initial NaOH solution and whether or not they are etched with KCN. Results shown in Table 2.2 indicate that exposure to NaOH for 1 hour greatly increases the amount of silver at the nanowire surface. However, a 10 minute KCN exposure decreases the amount of silver at the nanowire surface.

Sample Description	10 min NaOH	1 hour NaOH	24 hours NaOH	10 min NaOH + 10 min KCN	1 hour NaOH + 10 min KCN	24 hours NaOH + 10 min KCN
Ag Atomic Concentration (% relative)	0.4	7.1	3.3	0.7	0.7	0

Table 2.2: XPS data indicates that a small percentage of the nanowire surface is pure silver.

2.1.4 Nanowire Results

Nanowires with twin boundaries, but otherwise single crystalline, were produced at constant, low overpotentials via a 2D growth mechanism with a slow nucleation rate. Harvesting the nanowires with NaOH initially (in the first 10 minutes) removes the aluminum oxide from the original membrane increasing the Ag signal visible by XPS, e.g. it cleans the surface. But eventually (over the course of 24 hours) continual exposure to the NaOH solution increases the amount of non-silver atoms at the nanowire surface, dirtying the nanowire surface. Cleaning the nanowires

with KCN increases the amount of silver atoms at the nanowire surface only if the nanowires have been exposed to the NaOH solution for a very short period of time.

Sauer *et al.*. created nanowires under pulsing deposition conditions, shown in Fig. 2.1 because they believed these conditions discharged the capacitive "electrical double layer" that forms at the interface between electrode and solution. We found that, only for specific non-constant discharge pulse shapes, like those described by Sauer, were we able to grow wires. We believe that identical positive and negative pulse shapes do not result in a discharge of the capacitive layer but a removal of the deposited material. We believe Sauer *et al.* were depositing approximately one monolayer at a time via instantaneous nucleation, where nucleation occurs at all lattice sites simultaneously and immediately, although we were unable to fully reproduce his results. We suspect that our poorer quality bulbous wires (Fig. 2.4 M, P, and Q), grown under longer deposition times, grew by rapid 3D spherical growth combined with less rapid nucleation.

Wang *et al.* characterized the overpotential values that could yield single crystal or twin boundary nanowires for a given, commercial solution. They found that the lowest overpotentials that caused deposition were the best overpotential for growing single-crystalline wires. They propose a 2D growth mechanism and a slow nucleaction rate at these overpotentials. We were able to make nanowires with grains of single crystallinity using their technique as is shown by the TEM pattern in Fig. 2.6. We conclude that the wires grown are single crystal with twin boundaries by comparison of the TEM diffraction patterns obtained with the electron diffraction patterns presented by Wang *et al.*.

We propose that etching the nanowires with KCN removes silver oxide or other impurities from their surface which may have accumulated there during the growth into the alumina templates or the NaOH etching of the alumina templates. We have observed that the conductances of etched nanowires are much higher than the conductances of unetched wires. We have also observed that etching causes strong aggregation of nanowires. Furthermore, we suspect that the KCN etch dissolves silver much quicker than it dissolves the surface elements we wish to remove from the silver wires since fewer wires are observed after etching than were present before.

XPS studies showed that etching does increase the amount of silver at the surface of the wire if the time the wires spent in the NaOH solution, which dissolves the alumina membrane, is small. When wires are exposed to NaOH for longer times the amount of silver at the surface of the wires following KCN etch decreases. A possible explanation for this result is that the KCN etches the silver faster than it removes oxygen or alumina or other elements from the surface of the wires and so, if more wires have exposed silver, those wires may be etched completely away.

We have found that wires not exposed to KCN have very low conductance. A surface treatment recipe that yields wires with high conductances is a 1 hour exposure to NaOH followed by a 1 minute exposure to KCN with a concentration of 1.3×10^{-4} M. The smaller KCN etch time and concentration help decrease nanowire aggregation observed for stronger KCN etches but still dramatically improve the conductance. XPS studies of nanowires exposed to NaOH for 1 hour followed by 1 min KCN exposure have not been performed.

2.1.5 Conclusions

Nanowire fabrication attempts yielded a wide range of results from highly crystalline nanowires to no nanowires at all. We also determined that the manner of harvesting the wires affects the elemental surface structure of the nanowires. The nanowire fabrication process resulted in nanowires of different degrees of crystallinity. The most crystalline were those produced at constant, low overpotential.

2.2 Ag Nanowire Networks

Silver nanowire networks were studied for use as electrodes in thin film transistors. The networks were studied to determine if they could be highly conductive, patternable, printable to plastic substrates, and reduce stresses in these plastic substrates compared to conventional metal thin film electrodes.

The most crystalline Ag nanowires fabricated according to procedures in the previous section were cast into networks. We found that application of small amounts of pressure or temperature drastically increases the conductance of the networks. We also found that conductance of a network depends on the network concentration. Nanowire networks were fabricated by placing a drop, or drop casting, nanowires in solution onto silicon wafers. Factors affecting the uniformity of the networks were studied. The networks were printed into plastic and the conditions for achieving the most complete transfer of network were studied. Finally, techniques for printing the networks into controllable patterns were also investigated.

2.2.1 Conductance Background

A constant electric field, ***E***, applied across a conductor will induce a current density, ***J***, given by $\mathbf{J} = \sigma \times \mathbf{E}$, where the constant of proportionality, sigma, is defined as the electrical conductivity[15]. Conductivity is an inherent property of a material that depends most strongly on the number of free carriers (electrons or holes) in the material[15]. At room temperature, silver has the highest conductivity of any metal[15].

Resistivity, the inverse of conductivity, may be measured directly with a four-probe technique. Four probes may be placed in a specific pattern on a uniform sheet of known thickness of the material to be measured. A current may be passed through two of the probes while measuring the voltage across the other two. Van der Pauw measurements are taken by placing four probes at the corners of a square sample[16]. Additionally, a co-linear probe geometry was theorized for infinite samples. Correction factors have been tabulated so precise resistivities may be determined for finite samples for multiple sample geometries[17].

From a two-terminal resistance measurement of a material and its dimensions, a corresponding sheet resistance and/or resistivity may also be determined. The relationship between these quantities is given by

$$R = \frac{\rho L}{A}, \qquad (2.7)$$

where ρ is the resistivity of the material, L is the distance across which voltage is applied, and A is the cross sectional area of the sample. Or, the sheet resistance is given by $R_S = \frac{\rho}{t}$, where t is the thickness. Sheet resistance has units of ohms per

square where the dimensions of this square are irrelevant. Also, the power, P, associated with a given current I, and resistance, R, is $P = I^2 R$.

Conductance may be determined using two point or, more robust, four point probe measurement techniques. Both measurement techniques were performed on a network if possible for the sample configuration. In all cases, the four probe measurements taken were of the co-linear probe configuration since the sample geometry was not conducive to the Van der Pauw geometry[17].

2.2.2 Network Fabrication

Suspending nanowires in water and drop casting them onto thick silicon oxide layers yields the most uniform nanowire network. The most complete transfer of a nanowire network from a silicon wafer to a PET substrate occurs when transfer printing at 300 psi, 120 degrees C for 3 minutes. We found that one patterning method, printing from a silicon wafer patterned with mesas and trenches, yields clean, controllable network patterns in the PET.

Silver nanowire networks were drop cast onto different substrates including glass and silicon wafers with different thickness oxide layers (300 nm, 500 nm, and 300 μm) to determine which substrate would result in most uniform networks. Surfaces with greater hydrophobicity are ideal for drop casting the most uniform nanowire networks from a nanowire suspension in water. A drop of nanowire solution on a hydrophilic surface quickly wets the surface and results in dense patches of nanowires near the center of the drop and fewer wires near the edge of the drop. For very hydrophobic surfaces the drop edge is pinned and the contact angle slowly decreases as the solvent evaporates. The nanowires fall out of solution before all the

solvent can evaporate resulting in an almost uniform nanowire network. Mild 'Coffee stain' effects, a high density ring at the outer edge of the drop circling a low density ring just inside this edge, can be observed on these hydrophobic substrates. The inner ¾ radius of the network is mostly uniform, however. Three samples were prepared on each substrate and it was observed that the thickest, 300 μm, oxidized silicon wafer is the most hydrophobic surface (discussed in more detail in Chapter 5.4) and the resulting networks were observed to be more uniform. This surface was used to drop cast all nanowire networks in the remainder of this work.

Ag nanowires were also suspended in different solvents to determine which suspension resulted in the most uniform nanowire network upon solvent evaporation onto a 300 μm oxided silicon wafer. Solvents investigated were water, methanol, isopropyl alcohol, ethanol, acetone, and hexane. The IPA, acetone, methanol and ethanol nanowire suspensions quickly wet the oxided silicon surface due to their low liquid surface tensions. The nanowires in hexane would not suspend in the solution, they immediately aggregated into a sphere. Nanowires suspended in water were cast into the most uniform networks.

Silver nanowire networks were drop cast onto 300 μm thermally oxided silicon wafers and printed onto poly(methyl methacrylate) (PMMA) on PET at different heats and pressures. The best conditions for printing into PMMA is 120° C for 3 minutes with a pressure of at least 300 psi. The number of residual wires, and therefore the quality of the print, varied negligibly between pressures of 300 psi to 600 psi. Printing the nanowires at temperatures less than 120° C resulted in worse transfers to the PMMA substrate.

Three different attempts were made to pattern nanowire networks. The first was pattering a silicon wafer with areas of different hydrophobicity to direct the nanowire solution to certain areas. This was achieved by defining a photolithographic pattern in a resist on a silicon oxide substrate. The wafer with patterned photoresist was placed in a chamber that was evacuated to 200 milliTorr. Tridecafluorotetrahydrooctyltrichlorosilane (Gelest) was introduced in the evacuated chamber and the wafer was exposed to this chemical for two minutes. The hydrophobic molecule self-assembled on the silicon oxide substrate. The chamber was vented, the wafer was removed, and the photoresist was cleaned from the wafer surface. The resulting wafer was patterned with hydrophilic and hydrophobic regions corresponding to where the photoresist coated the wafer and the chemical coated the wafer respectively. The Ag nanowire solution was drop cast onto this wafer and results are shown in Fig 2.7 a). Patterning was moderately successful only when the hydrophilic area to be covered in wires was large enough to host a μL of nanowire solution, since one μL is the approximate minimum volume of the solution limited by the surface tension of water. Fig. 2.7 (a) shows an enlarged optical image of a chemically patterned surface where the hydrophilic areas are 3mm squares separated by a distance of 100 microns. The corners of the patterned area were not wet by the nanowire suspension. Furthermore, if a drop spanned the 100 micron gap, nanowires will remain in the gap after the water has evaporated. Patterns with less hydrophilic surface area (Fig 2.7 (b)) result in completely unpatterned networks.

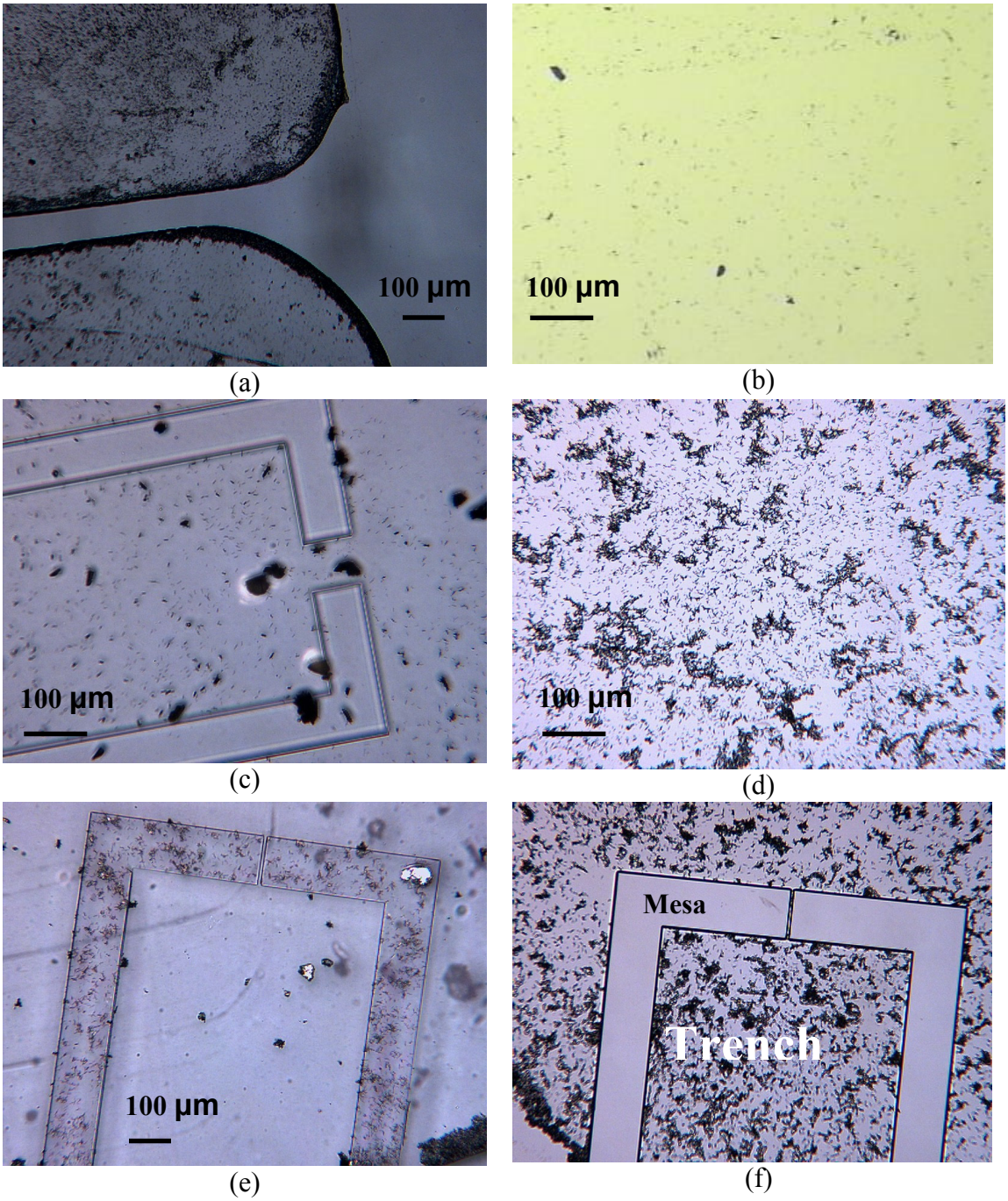

Figure 2.7: Optical images of nanowires on (a-b) chemically patterned silicon wafers, (c) PDMS stamp and (d) corresponding silicon, and (e) successfully patterned PET and corresponding (f) silicon wafer with height differential. The gap region is smallest in (e) and (f) but remains well defined with this technique.

A second patterning effort was to create a polydimethylsiloxane (PDMS) stamp of different heights that would selectively remove nanowires from a silicon

surface. This was done by photolithographically patterning a silicon wafer with photoresist. The wafer was etched in an reactive ion etcher (RIE) plasmatherm plasma enhanced chemical vapor depositor (PECVD) to a depth of approximately 0.5 microns. PDMS was poured on the wafer and cured. The Ag nanowire solution was drop cast onto a different, blank, silicon wafer and the solvent was evaporated. Then the PDMS stamp was pressed onto the nanowire network so that the higher stamp areas completely wet the nanowire/silicon surface. The stamp was removed and some nanowires were removed from the silicon wafer with it. Attempts to pattern networks using a PDMS stamp to remove nanowires from a silicon surface were completely unsuccessful as demonstrated in Fig. 2.7 (c-d). The desired result of this attempt was a patterned nanowire network on silicon (Fig. 2.7 (d)). So few wires were removed from the silicon that no pattern at all is visible.

The final patterning attempt used another plasma etched silicon wafer which was created as previously described. The Ag nanowire solution was drop cast onto the etched wafer and the network coated both the wafer's mesas and trenches. These networks were printed into PET against silicon blanks at 400 psi, 120º C for 3 minutes. The height profile of the printed network on the PET was undesirably large (1000 nm). So, the patterned network on PET was pressed between two silicon blanks at the same printing conditions reducing its height profile to 50 nm.

The attempt to pattern networks using a height differential while printing was successful. In Fig. 2.7 (e-f) the residual networks left only in the trenches of the etched silicon wafer is shown in (f) and in (e) the transfer of only nanowires from the silicon's mesas onto PET may be seen. This patterning method allows patterning of

small areas (limited by the length of the nanowires). It can be seen from Fig. 2.7 (e) that the gap is well defined, no wires cross the gap or hang off its edges. At higher network concentrations the gap region becomes increasingly less well defined.

2.2.3 Nanowire Network Conductance Measurements

Printing Ag nanowire networks drastically increases their conductance for all concentrations. Higher concentrations are more conductive. In situ studies revealed that either applying pressure of at least 7 psi or increasing the temperature of the network above 120 degrees C drastically improves the network conductivity.

Nanowire networks were prepared by diluting a very dense solution of Ag nanowires to five different relative concentrations; X, X/3, X/4, X/10, and X/20. These concentrations were drop cast onto silicon oxide wafers as previously described. Two 500 nm thick gold electrodes were evaporated through a shadow mask with a gap width of 100 microns between them as shown in Fig. 2.8. The resistance between the two gold electrodes was measured with a Fluke multimeter.

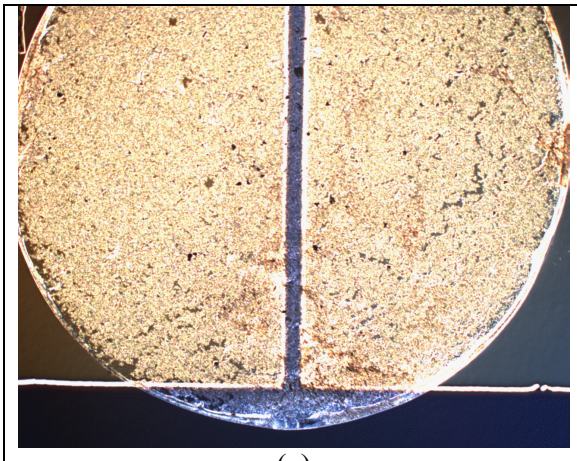

(a)

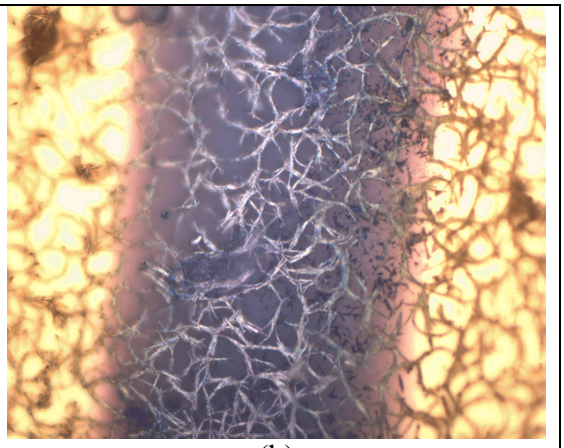

(b)

Figure 2.8: Evaporated gold contacts over drop cast nanowire network at two magnifications.

The five concentrations of nanowire networks were also printed from a thermally oxidized silicon wafer onto PET at 500 psi, 170° C for 3 minutes with a silicon blank behind the PET. The four-probe and a two-probe sheet resistance of these networks was measured using a Cascade probe station and Keithley current sources and voltage detectors. Each four-probe measurement was performed four times, with all probes in different, co-linear, radially centered locations on each sample. The resistivities of each network were calculated. Two probe measurements were also taken at different radii. 160 data points were accumulated for each concentration network. These resistances were converted to conductances and the average value of each is shown in Fig 2.9.

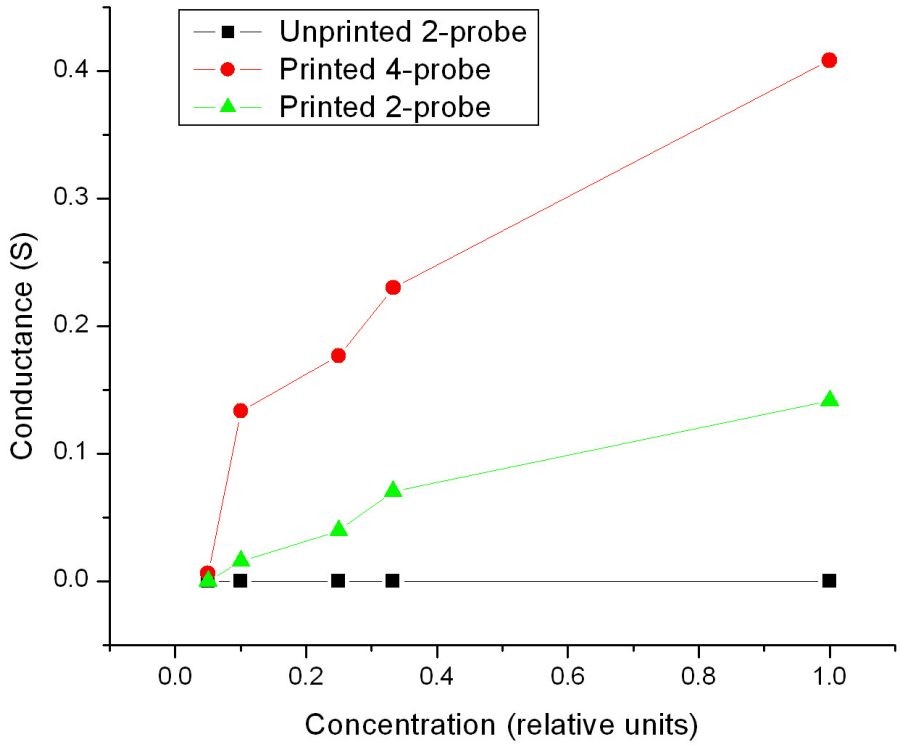

Figure 2.9: Conductance of printed and unprinted networks. Printing a nanowire network greatly increases its conductance.

Conductance as a function of pressure only was investigated for the most dense nanowire network, concentration X. 3 mm square gold electrodes a distance of 100 microns apart were evaporated onto a silicon wafer pretreated with tridecafluoro-tetrahydrooctyl-trichlorosilane (Gelest) and these electrodes were printed onto PET at 500 psi, 170 ° C for 3 minutes. The PET/electrode subassembly and a silicon wafer with nanowire network X were place in the transfer printing machine. Silver paint was used to fix wires to the gold contacts on the PET and one of the machine's two vacuum sealing rubber sheets was altered to allow the wires through it so electrical contact can be made inside the vacuum and measured outside the vacuum. The resistance between the electrodes on PET was measured by a Fluke multimeter as a function of pressure as it was pressed onto the nanowire network on silicon. The pressure range studied was 0-500 psi at room temperature. The resulting measured conductance as a function of the applied pressure is shown in Fig 1.10. It can be seen that increasing the pressure from 7 psi to 500 psi caused very little variation in the conductance, only a 0.004 S difference. Investigating the conductance change in the pressure range of 0 to 7 psi was not possible with the machine used to take these measurements since it is not accurate enough to decipher small pressure variations in this range. Upon venting and separating, the nanowire network remained on the silicon wafer; it did not transfer to the PET.

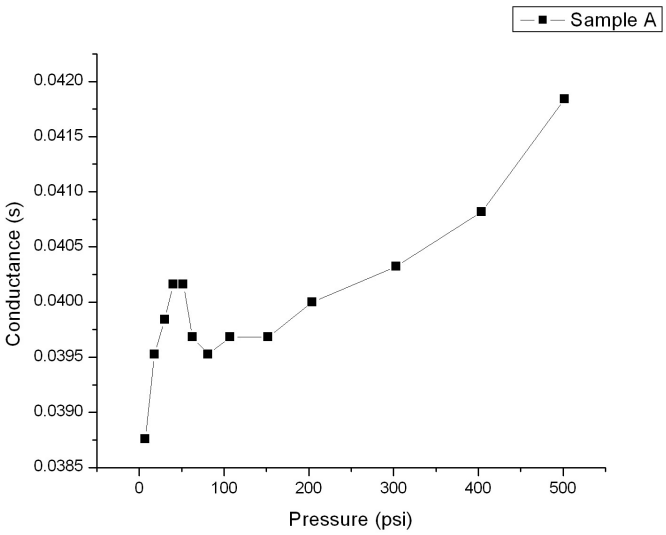

Figure 2.10: Conductance as a function of pressure at room temperature. Increasing the pressure between 7 and 500 psi only increases the conductance of the network by about 0.004 S.

The conductance as a function of temperature was also investigated for network concentration X. A silicon wafer with 3 mm square gold electrodes evaporated onto it was placed in a VWR 1415M oven. A drop cast nanowire network was placed between the two contacts. Wires that extended outside the oven were attached to the gold contacts with silver paint. No pressure was applied to this sample. The oven's temperature was increased in approximately 20° increments every 30 minutes from 40° to 180° C. The resistance between the gold electrodes was measured as a function of temperature. The sample was cooled and the resistance of the network on the silicon wafer after heating was measured again by a two-probe measurement with the multimeter. Fig 2.11 shows the conductance of this sample increases sharply around 140° C.

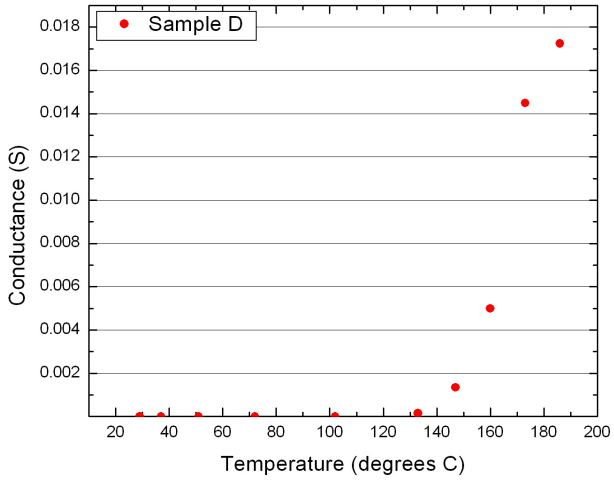

Figure 2.11: Conductance as a function of temperature at 0 psi.

The conductance of the nanowire networks on their drop cast, silicon substrate after elevating temperature and/or pressure for all samples was measured after cooling and/or relieving applied pressure. In all cases results were similar to the last measured conductance during the experiment. Increasing the pressure or temperature to which a nanowire network is exposed will increase its conductance dramatically but increasing both pressure and temperature creates the largest conductances.

Height profiles of highly conductive networks were measured using a profilometer and compared to those of conventional metal films (Fig 2.12). The overall height variation for the printed 200 nm Au film electrode and the Ag nanowire network electrode are comparable; both range approximately 600 nm. The nanowire networks are made of nanowires with diameters of 200 nm so this electrode is actually much thicker than the thin film electrode (to achieve comparable conductances). For a more similar measurement, nanowires of smaller diameter should be fabricated but alumina membranes with smaller pore sizes are not

commercially available. Increasing the aspect ratio of the nanowires would also help reduce dramatic height variations in the plastic substrate after printing. However, sonication breaks the nanowires into lengths of approximately 10 microns and is crucial to suspending the wires.

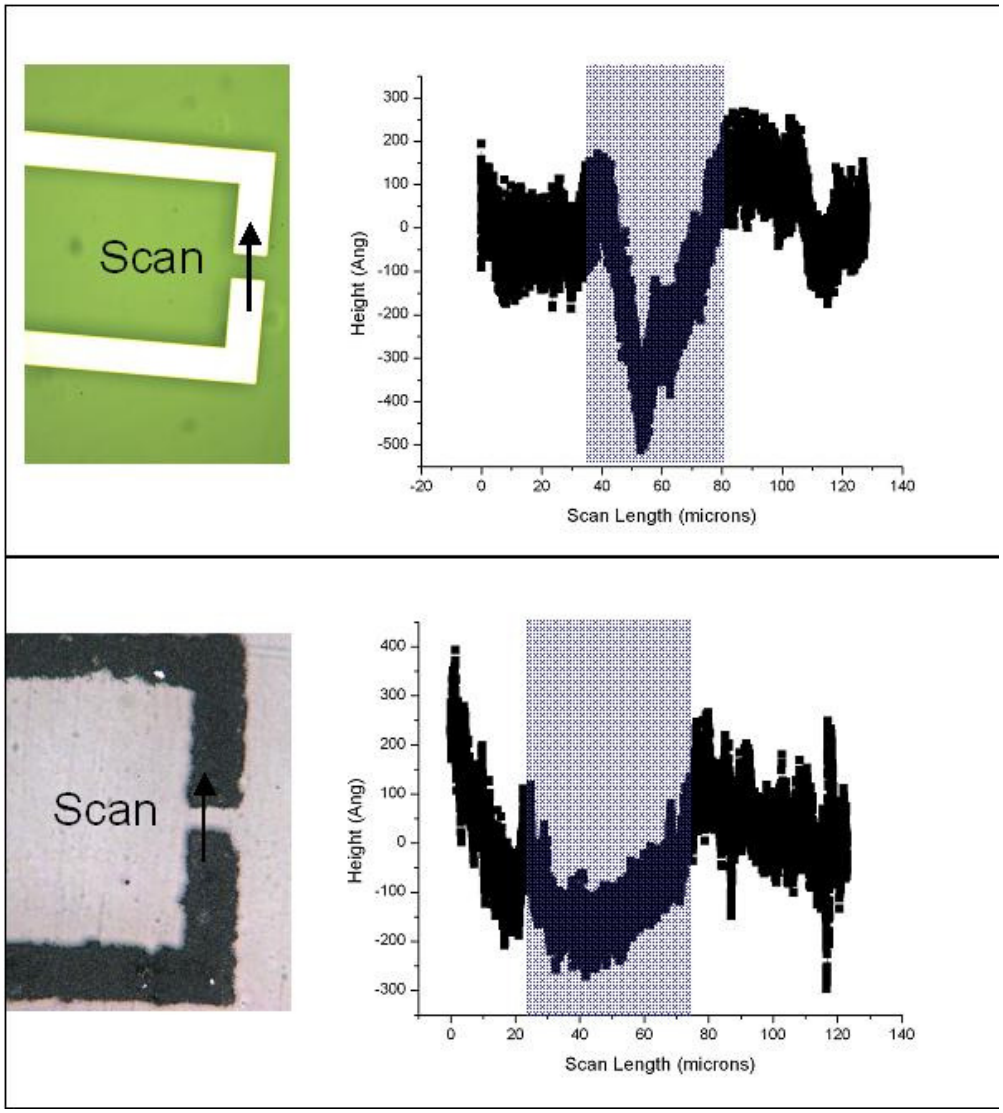

Figure 2.12: Height Profiles of (a) a conventional Au thin film electrode and (b) a Ag nanowire network electrode after printing to a PET substrate.

2.2.4 Conclusions

Nanowire network uniformity was found to be somewhat controllable. The nanowires we fabricate were massive enough to precipitate from solution within

minutes. Many more patterning options would be available and fabrication of uniform networks would be trivial if the wires remained better suspended. Since the wires precipitate quickly, we found that putting the networks on a hydrophobic surface was crucial to the formation of a uniform network. On such surfaces, the water will make a sharp contact angle with the surface and the position of the edge of the drop will not change much as the water is evaporated away. Since the wires in a drop on a hydrophobic surface are disturbed very little during the evaporation process, they form a uniform network, unlike the network formed on a hydrophilic surface which consists of multiple 'coffee stains' or rings where the drop edge was pinned before it jumped to a smaller radius.

We found that either temperatures above 140° C or pressures higher than 7 psi cause significant improvement in the conductance of the network. We suspect that the drop cast nanowires are sitting loosely on top of each other and upon application of a small amount of pressure they come into intimate contact with each other. Heating may improve the conductance of the networks by removing unwanted elements from the surface of the wires.

We found that the maximum conductivity we can obtain for a nanowire network printed onto a plastic substrate is 2.7×10^6 S/m. This conductivity is approximately an order of magnitude lower than the conductivity of bulk silver. We believe the lower conductivity is due to high contact resistance between the wires caused by impurities on the nanowire surfaces. The conductivity of MoW, the alloy currently used as electrodes for most industry applications, is $5\text{-}6.7 \times 10^6$ S/m. Twice as much power would be lost in devices fabricated with nanowire network electrodes

than is currently lost in metallic electrodes. The benefits the nanowire networks offer, smaller stress-flow patterns when printed onto plastic substrates, could compensate for this small power loss over small distances.

2.3 Carbon Nanotube Networks

Ag nanowire networks would improve in conductivity and cause fewer stresses in plastic substrates if their aspect ratios (diameter to length) were higher than 50. Commercially available metallic carbon nanotubes (CNTs) demonstrate aspect ratios that are an order of magnitude higher due to their mechanical strength. CNTs are also much less massive and therefore have the potential to create better suspensions. Carbon nanotube networks were investigated for their use as transparent electrodes that could be fabricated on plastic substrates.

2.3.1 Carbon Nanotube Background

A carbon nanotube is the 1D form of graphite; it is a sheet of carbons sharing *sp2* bonds in a honeycomb configuration that has been rolled into a cylinder and capped on both ends. Carbon nanotubes were "discovered" in 1991 when they were first imaged by high-resolution transmission electron microscopy[18]. Since then CNT growth by chemical vapor deposition has been perfected and their electrical properties have been studied. CNTs can be either semiconducting or metallic depending on their chirality but are highly conductive in both forms[19]. Metallic CNT networks as a thin film material are studied in this chapter.

2.3.2 Airbrushing Carbon Nanotube Netoworks

Bulk single-walled CNTs that were fabricated by the high pressure carbon monoxide (HiPCO) growth process were purchased from Carbon Nanotechnology, Inc. Bulk CNTs were dispersed in water but precipitated quickly unless also dispersed with sodium dodecyl sulfate (SDS). SDS was 1% the total weight of the dispersion. Dispersions were sonicated for 30 minutes and then airbrushed using a commercially available Aztek airbrush (A470 airbrush kit) onto different substrates. Nanotubes would aggregate on the substrate unless it was heated to 150º C to encourage rapid evaporation of the water in which the tubes were suspended. Airbrushing directly onto most plastic substrates was not possible because the heat caused the plastics to warp. Therefore CNTs were airbrushed onto silicon oxide substrates and transfer printed at 120º C and 300 psi onto PET. The thickness of the CNT film could be controlled by the concentration of tubes in water as well as the amount of time of airbrushing.

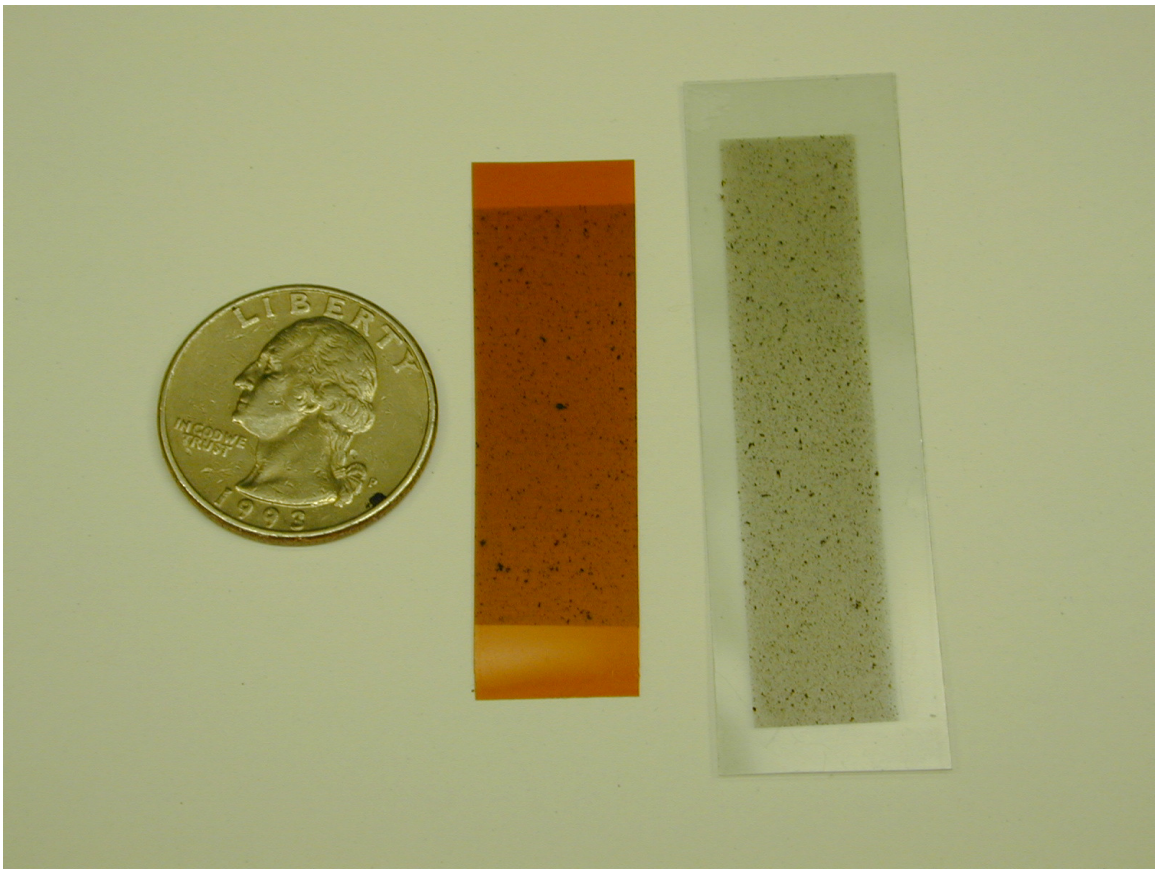

Figure 2.13: CNT networks were airbrushed onto silicon oxide substrates and then transfer printed onto plastic substrates kapton (left) and PET (right).

We were able to pattern nanotubes by covering the SiO_2 substrate with a shadow mask and airbrushing directly onto it. Often, bleeding under the shadow mask would occur and make detailed patterns or small features difficult to achieve. The height stamp method described for use with Ag nanowires was also effective for printing small features and detailed patterns of airbrushed CNTs. Airbrushed CNT networks are not compatible with photolithographic patterning because they are easily removed from a substrate upon submersion in a liquid – a necessary step in photolithography.

2.3.3 Transparency

CNT networks of minimum size 2 cm x 2 cm were airbrushed onto glass slides and silicon oxide substrates. The networks on SiO_2 were printed onto PET. Network thickness was roughly controlled by repeated spraying. A two terminal resistance for each network was measured and the sheet resistance was calculated. The transmission of light of a wavelengths ranging from 400-800 nm was measured using a UV-VIS spectrometer over network areas of 2 cm x 2 cm. The average transparency over all wavelengths was similar to the transparency at 550 nm. Fig. 2.17 shows the sheet resistance as a function of transparency for many networks. Glass substrates are less transparent than PET coated with indium tin oxide. No bare PET substrates were available. It can be seen from Fig. 2.14 that sheet resistances increase rapidly above transparencies of about 0.75. Therefore a CNT network density that is 70-75% transparent maximizes conductivity and transparency.

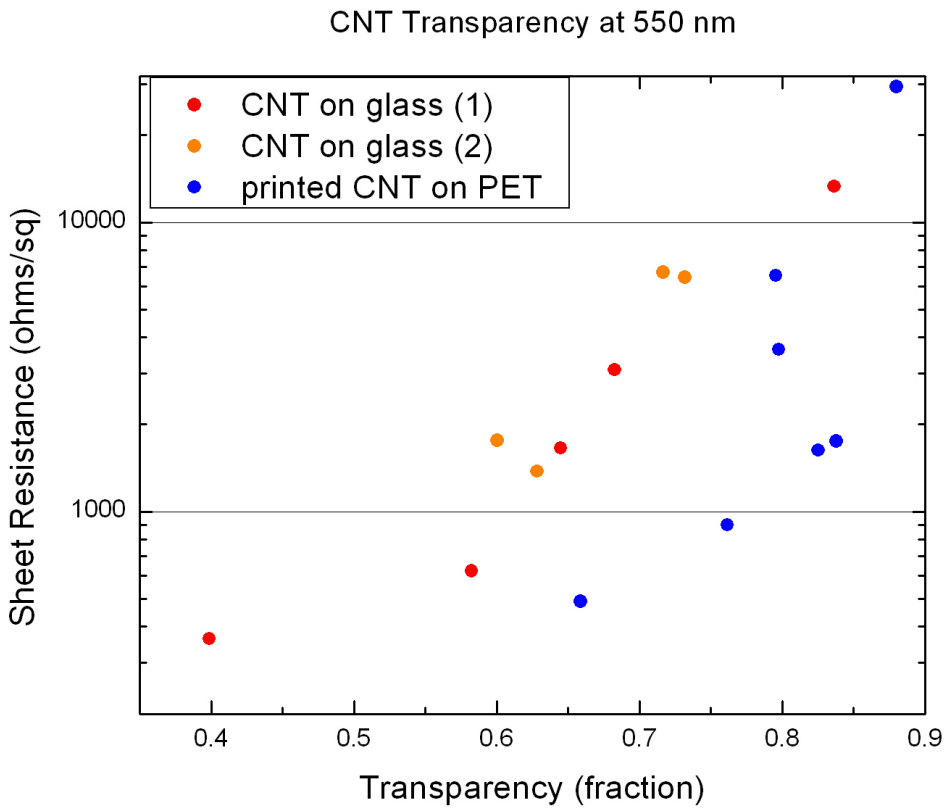

Figure 2.14: Sheet resistance is measured as a function of transparency for many different CNT networks on substrates glass and PET.

2.3.4 CNT Network Flexibility

CNT networks were printed onto PET and kapton substrates. Their transparency and original sheet resistance were measured as described. Then the networks on plastic substrates were bent around cylinders with different radii of curvature starting with the largest radius and working towards the smallest. The PET was always directly in contact with the cylinder; the cylinder did not disturb the CNT network. Electrical measurements were taken while the CNT network was remained bent (strained) and after it was relaxed again. The network sheet resistance while bent is shown in Fig. 2.15 for two different CNT networks. The relaxed sheet resistance

was similar to the strained sheet resistance until a radius of curvature of about 5 mm was achieved.

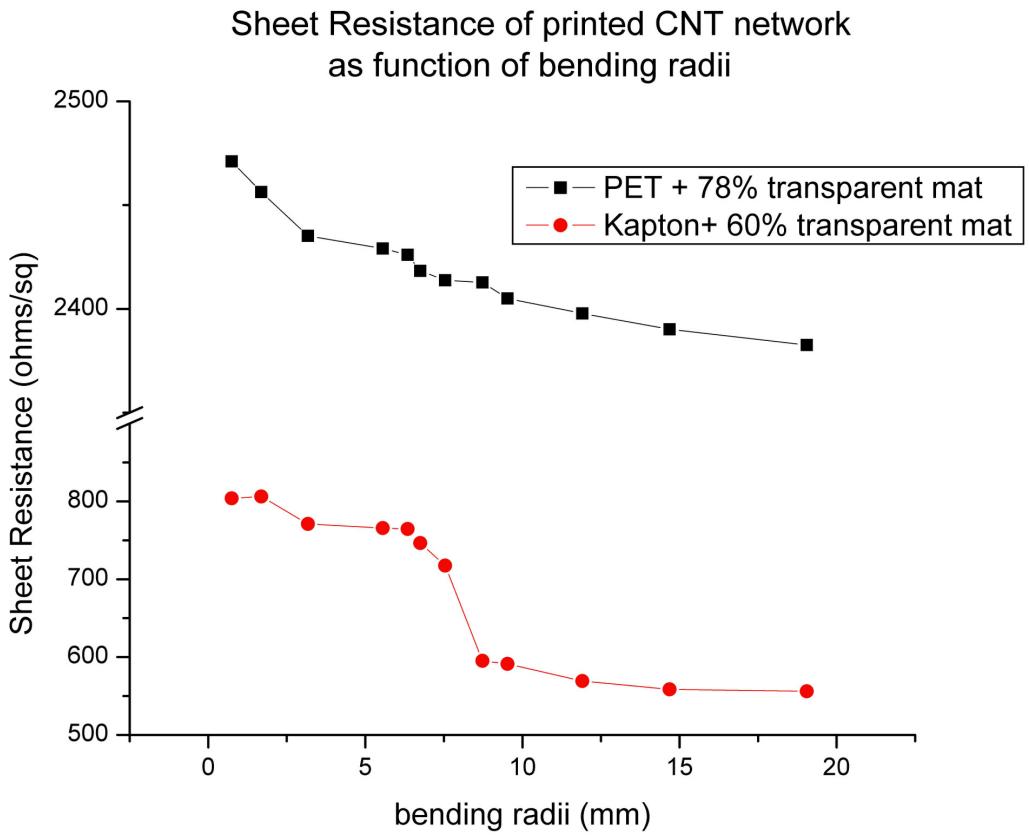

Figure 2.15: Sheet resistance of strained CNT networks. The strain was accomplished by bending the network on a plastic substrate around cylinders of different radii.

2.3.5 Polymer Wrapping

CNT networks on PET substrates are mostly transparent while demonstrating high conductivities. Other groups have seen improved conductivity of similar CNT networks by wrapping CNTs in certain polymers in aqueous suspension[20,21]. These groups found that hydrophobic polymers such as polyaniline, polyvinyl pyrrolidone (PVP) and polystyrene sulfonate will spontaneously wrap themselves around carbon nanotubes in order to minimize their energy when all are placed in water and heated.

The polymer is the suspending agent for the CNTs and, when deposited on a substrate, the polymer will interfere with CNT electrical behavior in some way. These groups report that the polymer wrapping process can be reversed by changing the suspending liquid[21].

We have created CNT suspensions of 50 mg/L as opposed to the suspensions in SDS that are studied in the rest of this chapter whose concentration is 2000 mg/L. We have added 1% by weight SDS, polyvinylpyrrolidone (PVP), poly-alpha-methylstyrene (PAMS), and polystyrene (PS) and heat and sonication. Fig. 2.16 shows that all polymers suspend this small concentration of CNTs better than SDS. These suspensions were drop cast on SiO_2, and Au electrodes were sputtered onto all networks with a gap length of 2 mm between electrodes. The resistance was measured and the sheet resistance of each network was calculated and is shown in Table 2.3. PS and PAMS decrease the sheet resistance by 2-3 orders of magnitude though it is not clear if the decreased resistance is merely caused by a better dispersion of the network allowing it to more quickly overcome the percolation threshold. In the future, SEM images and UV-VIS spectra could be measured to help elucidate the cause of improved in sheet resistance.

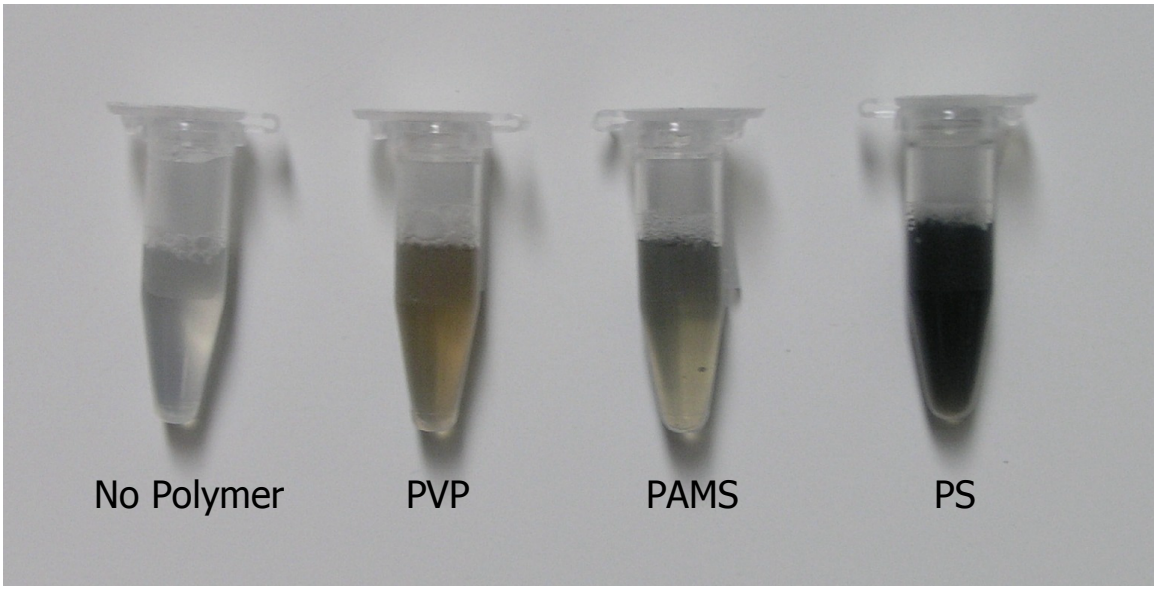

Figure 2.16: 50 g/L wt% CNT suspended in water and SDS (vial labeled no polymer) or certain hydrophobic polymers. It is not apparent that CNTs have been suspended in the no polymer solution but in all others the change in liquid color indicates CNTs are suspended.

Polymer	None	PVP	PAMS	PS
Sheet Resistance (kΩ/Sq)	10600	13200	67.2	7.2

Table 2.3: The sheet resistance of networks of CNTs wrapped with polymers.

Chapter 3: Height Correlations of Ultrathin and Commercial SiO_2

Atomic Force Microscopy was used to measure the statistical characteristics of the roughness of silicon oxide surfaces in the context of their use as substrates for thin film transistors. The two silicon oxide surfaces studied were a commercial thermal oxide (300 nm thick) and the native thin oxide (~1nm thick) resulting from oxidation of atomically clean silicon at room temperature. The average root mean square (rms) height variation σ of the thin oxide is determined by the local step density of the silicon substrate, and varies over a range of 0.09 - 0.19 nm, with the average $\sigma_{nat} = 0.10 \pm 0.02$ nm, significantly smaller than that of the thick thermal oxide $\sigma_{therm} = 0.18 \pm 0.03$ nm. The roughness characteristics were quantified via height-height correlation functions and Fourier analysis. The height-height correlations for both types of surface have limited regions of power-law dependence. The effective roughness exponents for the thin oxide are smaller than for the thick oxide, and decrease monotonically with step density. Fourier analysis shows that the height variation amplitude is only 0.002 - 0.003 nm at wavelengths around 1 nm. This corresponds to a smallest local radius of curvature of 10 nm or more, unlikely to perturb transport in supported graphene.

3.1 Correlation Function Background and Literature

Silicon oxide is widely used in experimental physics and materials science research. When the oxide is used as the gate dielectric for thin film transistors (TFTs), its surface morphology is important for materials such as graphene or pentacene,

whose electrical properties depend strongly on local environment[22-24]. Furthermore, commercially available 300 nm thermal silicon oxide is one of very few substrates upon which graphene may be easily, optically identified[25]. Since most graphene transistors have been fabricated with this 300 nm gate dielectric, there is theoretical interest in quantifying the substrate morphology to provide a basis for quantifying its possible impact on graphene transport characteristics[26,27,28,29]. Ultimately, tailoring the silicon oxide substrate morphology may be one method for controlling the properties of graphene[30]. Here we show that is possible to obtain SiO_2 surfaces with roughness less than normal thermal oxides by using ultrathin native oxides grown on clean, well-characterized Si substrates. We also provide a quantitative description of the roughness for use in quantifying its impact on TFT performance. The roughness of the Si/SiO_2 interface has been studied extensively[31-34]. The results universally show that the interface roughness is determined by the roughness of the Si surface prior to a thermal oxidation process, even to the point of preserving the original stepped surface structure at the atomic scale. Fewer studies report the characteristics of the oxide/air interface, but for thick thermal oxides, the top surface is found to be considerably rougher than the Si/oxide interface[22,24,32] with typical rms roughness of 0.3 nm or more.

However, the growth of the ultra-thin (1-2 nm) native oxide upon room-temperature exposure of clean silicon to oxygen, yields oxides with surfaces conformal with the original Si substrate[22,33,35]. On these oxide surfaces, the structural roughness will be limited by atomic scale surface features such as steps and kinks[36,37]. Thus by control of the original Si substrate structure, the surface of the oxide can be

tailored[38]. Here we characterize the statistical roughness of such ultrathin oxide surfaces in the context of the underlying step structure using correlation function and Fourier analysis of the height profiles determined from atomic force microscopic imaging. We quantify the variation of the correlation functions and wavelength-dependent amplitude with step density, yielding quantitative descriptions of the local structural curvatures that are important in determining the impact of the roughness on graphene transport.

3.2 Experimental Procedure

Two types of silicon oxide surfaces were studied; a silicon wafer with a 300 nm thick thermal oxide as supplied by Silicon Quest International, and a wafer with a native oxide approximately 1 nm thick. The 300 nm oxide was degreased with acetone, methanol, and IPA prior to measurement. The ultra-thin oxide was prepared by resistively heating a Si wafer in UHV[39], slowly cooling , and oxidizing by oxygen exposure at room temperature[40]. The initial Si(111) surface has a factory quoted miscut angle of 0.5 degrees toward the $[2\bar{1}\bar{1}]$ direction. All measurements were taken on the 1 nm oxide no more than 2 months after sample preparation. Local variations in step density can be found around pinning sites on the surface[41].

AFM images were measured under ambient conditions with a Digital Instruments Nanscope IIIa operated in tapping mode. All measurements were taken using nanoscope control software with a number of different silicon nitride tips. Image size is 200 nm x 200 nm with 512 lines per image and 512 points per line unless otherwise specified. The scan rate, 0.5 Hz, was also constant for all images. Many data sets ranging from 7-30 AFM images were taken for each set of conditions

considered. All the data in one set were taken with the same AFM tip. Within each data set the AFM tip is moved 500 nm vertically and/or horizontally between sequential images. The images measured in different data sets may be much further away from each other, up to millimeters. Image size, tip, and oxide thickness were all varied to investigate the effect all these parameters have on the height-height correlation function.

All images were saved using a full offline planefit. All saved images were processed using SPIP software plane correction. A global correction was performed by fitting the images to a 3rd order polynomial and subtracting the fit from the original image to give a corrected image. Then a line-wise correction was performed by fitting a 0th degree polynomial to each line scan and subtracting the fitted line-scan from the original line scan to give the final height profiles ***z(r)***. Images that continued to show scan artifacts after correcting were discarded.

Characterization of the oxide morphology historically was done using diffraction techniques, and more recently using real space imaging [32,34,36,42,43], both of which can be used to evaluate the height-height correlation function, defined in one-dimension as

$$G(x) = \left\langle \left(z(x_0 + x) - z(x_0)\right)^2 \right\rangle , \qquad (3.1)$$

where the brackets indicate an average over the entire ensemble of initial height positions x_0. For non-equilibrium surfaces, the morphology is often found to be self-affine, with the correlation function initially increasing as a power law in distance and then saturating at lengths greater than the correlation length ζ [24,43,44],

$$x << \xi \qquad G(x) = ax^{2H} \qquad (3.2a)$$

$$x > \xi \qquad G(x) = 2\sigma^2 \qquad (3.2b)$$

where σ is the rms roughness defined as the standard deviation of the height [43,44]. Due to noise and resolution limits, fitting the data to a power law form, Eqn. 3.2a, is only possible over a limited length scale, as a result (see discussion) we characterize the limited power-law dependence by an effective roughness exponent, $2H_{eff}$. While the roughness exponent is a useful parameter for comparing different oxide characteristics, quantification of the roughness characteristics is more directly accomplished using the measured roughness height profile ***z(r)*** in a Fourier transform to characterize the roughness spectrum *A(q)*.

For each corrected image, the height-height correlation function defined by Eqn. 3.1 was computed, with the *x* direction defined as the image scan direction, and evaluated for power law behavior using a log-log display. Where power-law behavior was observed, the correlations functions were fit to Eq. 3.2a, $G = a * x^{2H}$ with a and *2H* the fitting parameters. The exact data range fit was different for every group of correlation functions but was larger than an x range of 3 nm in all cases. At larger distances the correlation functions become flat and were fit to a horizontal line as per Eqn. 3.2b. The intersection of the two fits, was used to define the correlation length. To evaluate the statistical variance of the observations, the correlation function for each image was fit and then the average of these fit parameters for all images was taken. For comparison, all the correlation functions in a data set were averaged and one fit was performed for the averaged data set. The resulting fit parameters for the averages of all images were similar to the average of the fit parameters calculated for individual images and will not be discussed further.

Logarithmic fits were also performed on all data sets but were not found to be substantially better than the power-law fits in any case. For the 1 nm silicon oxide wafers, 1d height-height correlation functions were also computed for a variety of discrete directions; parallel to the step direction, perpendicular to the step direction and for a variety of directions in between. The same power-law fit was performed for all scan directions for each image.

3.3 Correlation Parameter Results and Analysis

For the thin oxide data samples, four data sets were acquired in the same approximate area on the same 1 nm oxide surface with the same tip. After each data set was acquired a different (clean SiO_2 surface) was measured with the same tip as a method to assess any variation in the tip property. The data sets were acquired in the order a, b, c, and finally d. A standard image from each of these data sets is shown in Figure 3.1, steps are visible in all images. The fit parameters *a* and *2H*, the correlation length, and the rms roughness shown in Table 3.1. The average values of $2H, \sigma$, and ξ are 0.24, 0.097 nm, and 36.3 nm respectively. However the variation between the values measured for different areas on the surface is larger than the standard deviation on the values for any one data set. These variations may be due to the tip slowly deteriorating as it scans. However, since the variations are not monotonic with image order, they are more likely caused by real variations in the surface of the 1 nm oxide between different locations.

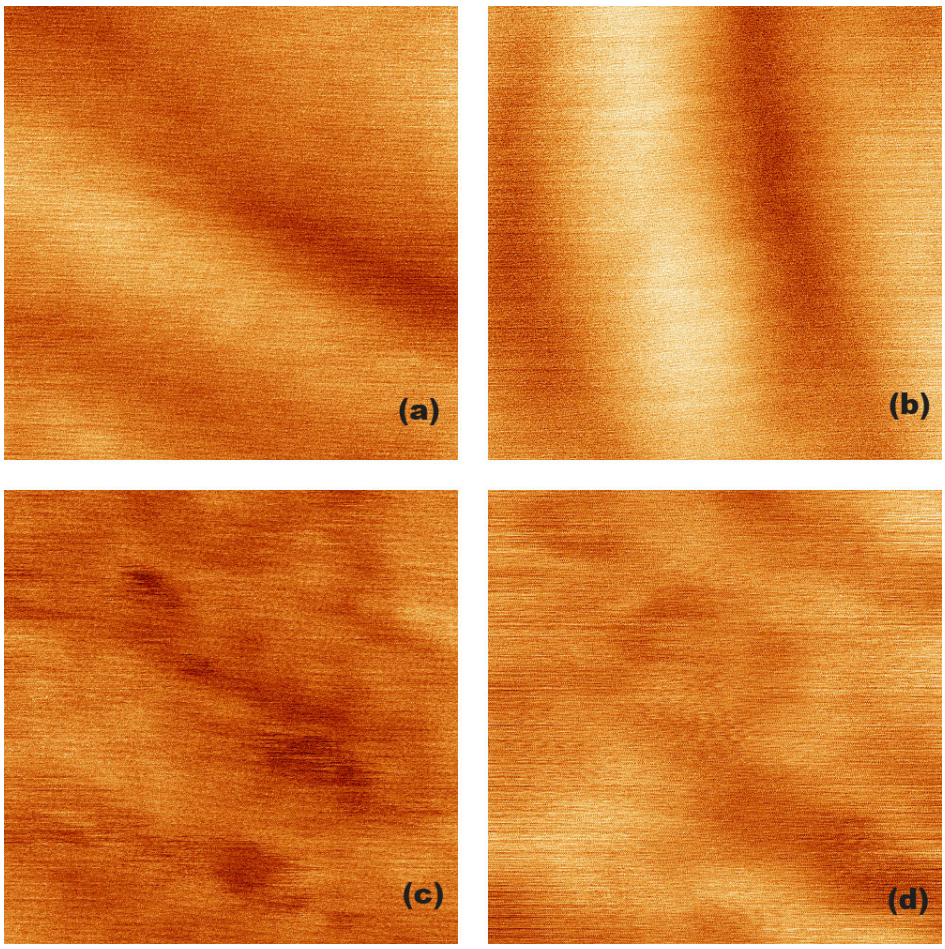

Figure 3.1: Four 200 nm square AFM images for a native oxide surface, measured with the same AFM tip. Each image is one of a larger data set, with the data sets taken within a 1 mm square area on the sample. The scan direction for all images is horizontal. The step direction for each image varies but images (a), (c), and (d) have an approximate step direction of 140 degrees (counter-clockwise) from the (+) x-direction and image (b) has an approximate step direction of 100 degrees (counter-clockwise) from the (+) x-direction.

Data Set	a	2H	RMS roughness (nm)	Correlation length (nm)
a	0.00689 ± 0.00099	0.186 ± 0.087	0.082 ± 0.009	41.8 ± 10.6
b	0.00576 ± 0.00138	0.308 ± 0.098	0.094 ± 0.008	41.4 ± 5.8
c	0.0127 ± 0.0038	0.247 ± 0.044	0.117 ± 0.014	25.8 ± 4.7
d	0.00798 ± 0.00131	0.236 ± 0.057	0.096 ± 0.006	36.3 ± 4.7
Average a:d ± standard devation	0.00833 ± 0.00305	0.244 ± 0.050	0.097 ± 0.014	36.3 ± 7.5

Table 3.1: The average fit parameters (Eqs. 3.2a and 3.2b) and standard deviation for correlation functions computed for data sets for the native oxide as shown in Figure 1. Each data set contains at least 7 AFM images all measured with the same AFM tip on the same surface.

To evaluate the variation in fitting parameters that may arise from variability in the AFM tip, for data sets taken with different tips on the same oxide surface, four different tips of resonant frequencies 382, 384, 387 and 393 kHz were used to scan the same approximate area on the same 300 nm oxide surface. Figure 3.2 shows a typical image from each data set and the fit parameters are summarized in Table 3.2. All tips used to acquire this data were new. The average values of the fit parameters from all data sets were again computed. For an example fit parameter, ξ, the standard deviation of the data set averages is 2.84 nm. This value is comparable to the standard deviation of each image from the data set averages; 2.50, 2.82, 4.12, and 1.87 nm. We see that there is little difference between the standard deviations for data sets taken with different tips and those taken with the same tip. Unlike the thin oxide, the thick oxide has limited variation in its statistical roughness in different areas, despite the use of different tips. Therefore, we conclude that variation in tip frequency and

corresponding scanning parameters are not the origin of the large variability observed for the thin oxide.

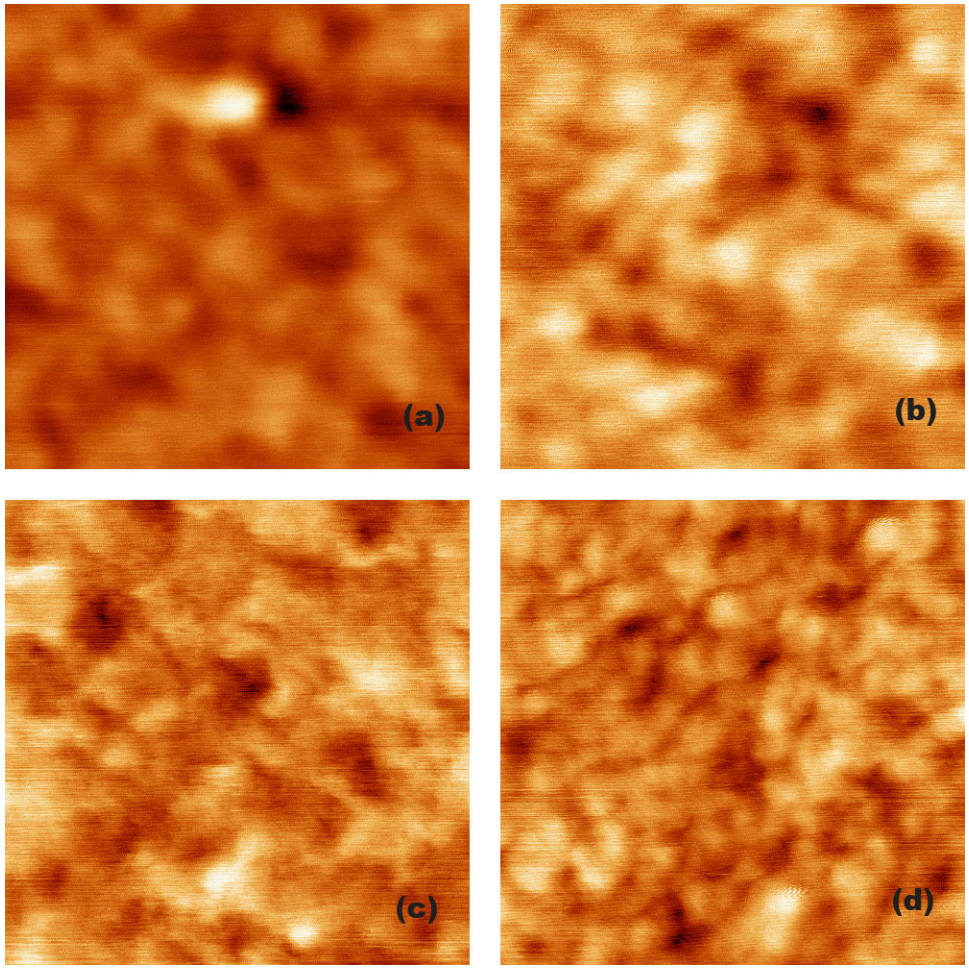

Figure 3.2: One 200 nm square AFM image is shown from each data set taken using tips of resonant frequency (a) 382 kHz, (b) 384 kHz, (c) 387 kHz, (d) 393 kHz on the same 300 nm oxide surface. All data sets were taken within 1 square mm of each other.

AFM tip	a	2H	RMS roughness (nm)	Correlation length (nm)
(a) 382 kHz	0.00224 ± 0.00037	1.07 ± 0.08	0.157 ± 0.017	18.1 ± 2.5
(b) 384 kHz	0.00270 ± 0.00043	0.854 ± 0.126	0.130 ± 0.020	19.3 ± 2.8
(c) 387 kHz	0.00276 ± 0.00120	0.957 ± 0.064	0.148 ± 0.012	19.7 ± 4.1
(d) 393 kHz	0.00693 ± 0.00614	0.983 ± 0.156	0.195 ± 0.015	13.5 ± 1.9
Average (a):(d) standard devation	0.00366 ± 0.00219	0.967 ± 0.091	0.157 ± 0.027	17.7 ± 2.8

Table 3.2: The average fit parameters (Eqs. 3.2a and 3.2b) and standard deviation for correlation functions computed for data sets shown in Figure 3.2 for the 300 nm thermal oxide. Each data set contains at least 7 AFM images, taken in different areas of the surface using different AFM tips.

The effect of the scan size on correlation functions was also studied. In a 200 nm AFM image, real physical features occur slowly and infrequently, thus these images are dominated by noise. So, 200 nm and 500 nm square AFM images were compared on both the 300 nm and 1 nm oxides. A sample image from each data set is shown in Figure 3.3. The fit parameters for the correlation functions for each data set are shown in Table 3.3. Larger images for both oxide thicknesses exhibit slightly larger root mean square (RMS) roughness and correlation length. The most striking difference between all the data sets, however, is the large standard deviation on the roughness exponent, *2H*, for the 200 nm scan size on the 1 nm oxide surfaces. For 200 nm scan sizes the number of steps captured in a given image differs, sometimes dramatically, from image to image. We have observed between 1 and 8 steps per 200 nm image but for all 500 nm images the number of steps is larger and more constant.

The effect of steps on the correlation function will be discussed in greater detail below.

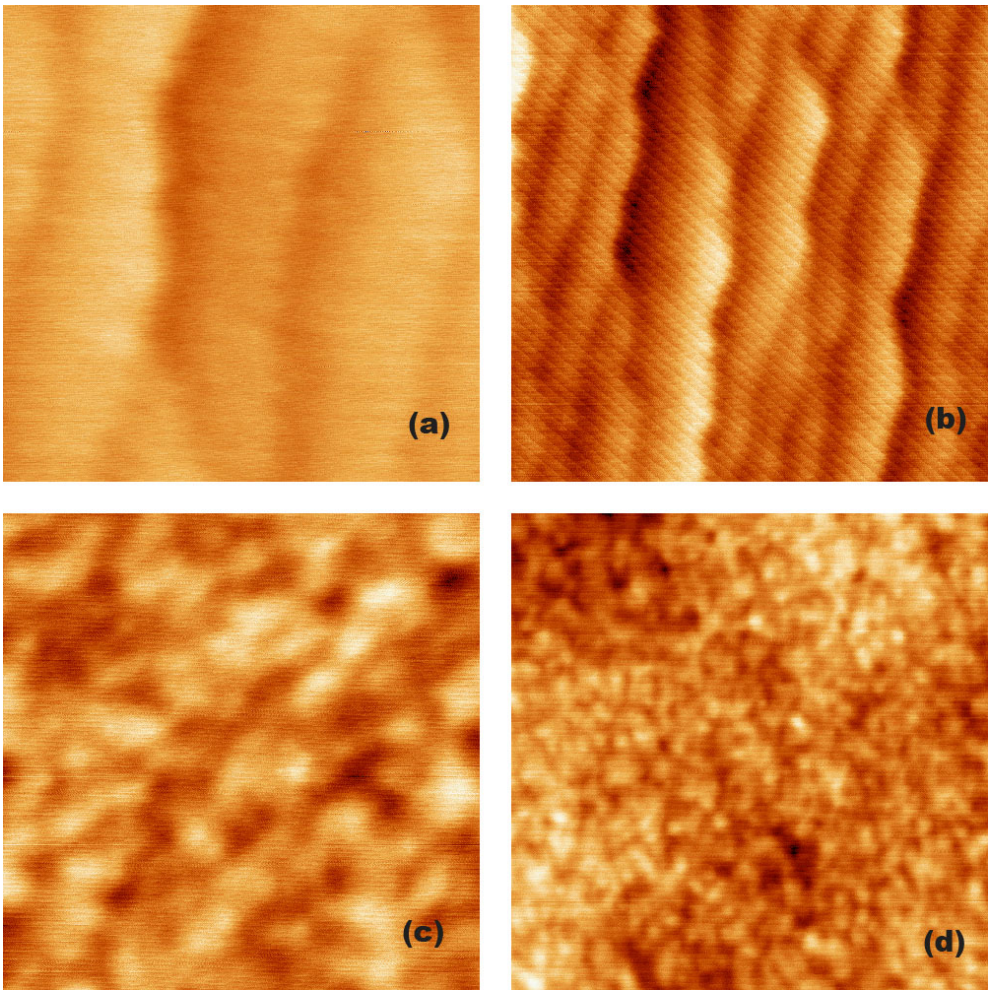

Figure 3.3: A sample image from each data set for images; (a) 1 nm oxide surface, 200 nm^2 image size with tip 1, (b) 1 nm oxide surface, 500 nm^2 image with tip 1, (c) 300 nm oxide surface, 200 nm^2 image with tip 2, (d) 300 nm oxide surface, 500 nm^2 image with tip 2. The step edge direction is approximately 90 degrees from the x-axis scan direction for all images in each data set.

image size	a	2H	RMS roughness (nm)	Correlation length (nm)
(a) 200nm	0.00115 ± 0.00027	0.947 ± 0.143	0.112 ± 0.016	26.4 ± 2.2
(b) 500 nm	0.000784 ± 0.000108	1.07 ± 0.07	0.139 ± 0.016	38.2 ± 8.2
(c) 200 nm	0.00251 ± 0.00026	1.11 ± 0.05	0.166 ± 0.012	16.1 ± 1.2
(d) 500 nm	0.00232 ± 0.00025	1.20 ± 0.04	0.203 ± 0.012	19.6 ± 1.6

Table 3.3: The average fit parameters (Eqs. 3.2a and 3.2b) and standard deviation for correlation functions computed for data sets shown in Figure 3.3. Data sets (a) and (b) were taken with the same tip on the 1 nm oxide. Images in (a) are 200x200 nm^2, images in (b) are 500 x500nm^2. Data sets (c) and (d) are taken with the same tip on the 300 nm oxide. Images in (c) are 200x200 nm^2, images in (d) are 500x500 nm^2.

Finally, the oxide surfaces were compared by measuring the two different oxide surfaces with same tip consecutively and then repeating the measurement four times with four different tips (labeled tips 3-6). All correlation functions calculated from the data measured with tip 3 are shown in Figure 3.4 and the fit parameters for all data taken with all tips are shown in Table 3.4.

Figure 3.4a displays the correlation functions (Eq. 3.1) that were computed for the individual images of a single data set for the thermal oxide surface. There is little variation between correlation functions in this graph. For this data set, the average roughness parameters and their standard deviations are an rms roughness, σ_{therm} = 0.18 ± 0.03 nm, effective roughness exponent, $2H_{eff}$ = 0.97 ± 0.11 nm, and a correlation length, ξ_{therm} = 15.9 ± 2.8 nm. The red bars (thick oxide) in the histograms (Figs. 3.4 c and d) show the variability observed over many such data sets. The 300 nm oxide surface is classified as a self-affine surface due to the value of the scaling exponent, 1.0 [36].

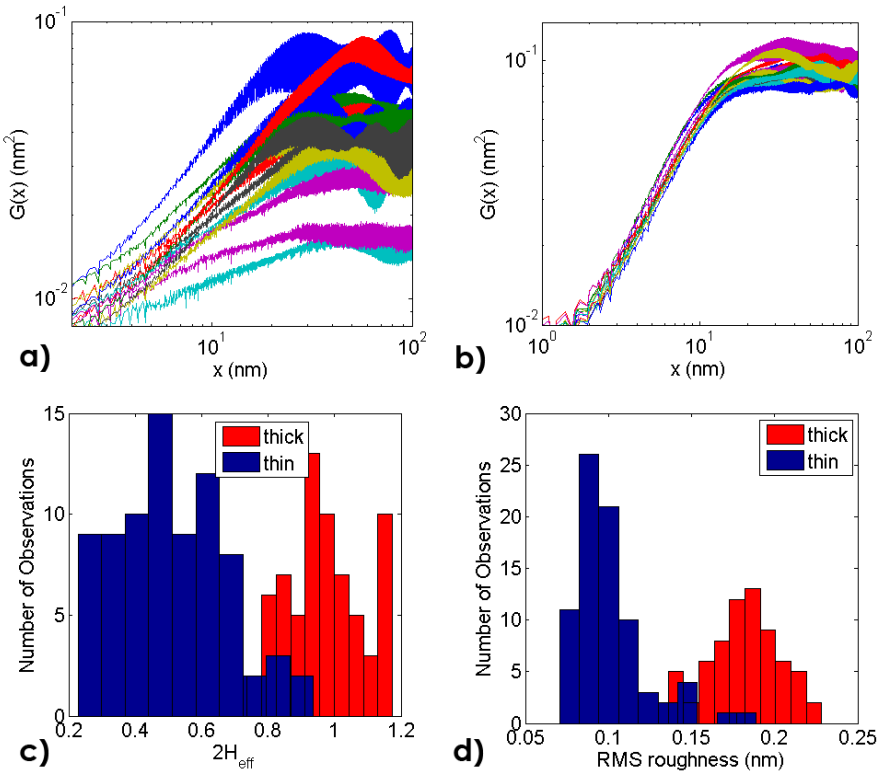

Figure 3.4: The correlation functions, *G(x)*, calculated for individual images in a single data set, for (a) the 300 nm oxide, average values: $2H_{eff} = 0.98 \pm 0.12$, $\sigma = 0.18 \pm 0.03$ nm, $\xi = 15.9 \pm 2.8$ nm, and (b) the 1 nm oxide, average values: $2H_{eff} = 0.52 \pm 0.12$, $\sigma = 0.10 \pm 0.02$ nm, $\xi = 23.9 \pm 2.0$ nm. Tabulation of the results for many such images in histogram form; total number of thin oxides samples in histograms are 79, total number of thick oxide samples are 68. (c) effective roughness exponent, $2H_{eff}$, and (d) RMS roughness, σ, for the thin oxide (blue bars) and the thermal oxide (red bars). The averages over all the measurements shown in the histogram for the thick oxide are: $\sigma_{therm} = 0.18 \pm 0.03$ nm, $2H_{therm} = 0.97 \pm 0.11$ nm.

	a	2H	RMS roughness (nm)	Correlation length (nm)
300 nm oxide Tip 3	0.00465 ± 0.00032	1.14 ± 0.03	0.210 ± 0.008	13.3 ± 1.0
300 nm oxide Tip 4	0.00213 ± 0.00022	1.00 ± 0.06	0.146 ± 0.010	19.9 ± 0.8
300 nm oxide Tip5	0.00529 ± 0.00118	0.964 ± 0.061	0.185 ± 0.011	14.6 ± 0.9
300 nm oxide Tip 6	0.00600 ± 0.00154	0.840 ± 0.053	0.173 ± 0.011	16.0 ± 1.5
300 nm oxide average tip3-6 ± Standard dev.	0.00452 ± 0.00168	0.986 ± 0.123	0.179 ± 0.027	15.9 ± 2.8
1 nm oxide Tip3	0.00494 ± 0.00146	0.642 ± 0.223	0.135 ± 0.028	23.3 ± 4.5
1 nm oxide Tip 4	0.00329 ± 0.00089	0.527 ± 0.115	0.0941 ± 0.0112	25.4 ± 4.1
1 nm oxide Tip5	0.00283 ± 0.00044	0.560 ± 0.103	0.0928 ± 0.0102	25.5 ± 3.9
1 nm oxide Tip 6	0.00573 ± 0.00110	0.357 ± 0.082	0.0918 ± 0.0088	21.3 ± 2.9
1 nm oxide average tip 3-6 ± Standard dev.	0.00420 ± 0.00137	0.521 ± 0.120	0.103 ± 0.021	23.9 ± 2.0

Table 3.4: The average fit parameters (Eqs. 3.2a and 3.2b) and standard deviation for correlation functions computed for data sets not previously shown. Correlation functions corresponding to tip 3 are shown in Figure 3.4. All data sets were taken within 1 mm^2 of each other for the 1 nm oxide and within 4 mm^2 of each other for the 300 nm oxide. The scan direction for all data sets is the *x*-axis. The step directions for the 1 nm oxide are; tip 3, ~50 degrees counter-clockwise (CCW) from the positive *x* direction; tip 4, ~50 degrees CCW from the positive x direction; tip 5, ~60 degrees CCW from the positive x direction; and tip 6, ~ 50 degrees CCW from the positive *x* direction.

The dependence of the thin oxide characteristics on the local step density of the silicon substrate is illustrated for a data set taken in a region of substantial variability on the scale of the 200 nm squared AFM image measured with position displacements of 500 nm. There is a large variability in statistical roughness from

position to position, as is shown in Fig. 3.4 b), a data set of correlation functions, *G(x),* taken on a thin oxide surface. The step densities corresponding to the individual correlation functions shown in Figure 3.4b vary between 1 step in 200 nm and 1 step in 20 nm. The scan orientation direction is about 50 degrees with respect to the step direction for all images. For the 1nm oxide data set, the average roughness parameters and their standard deviations are an RMS roughness, σ_{therm} = 0.10 ± 0.02 nm, effective roughness exponent, $2H_{eff}$ = 0.52 ± 0.12 nm, and a correlation length, ξ_{therm} = and 23.9 ± 2.0 nm. The variability shown in Figure 3.4b is reflected in the large variability across data sets as shown by the blue histogram bars (thin oxide) in Figs 3.4c and d. On average, the 1 nm oxide has a lower RMS roughness by 0.08 nm and longer correlation length by 8.0 nm indicating that the 1 nm oxide is a smoother surface than the commercial oxide.

Although, on average, the roughness exponent is distinctly different for the two types of oxide, there is significant variation in the fit parameters for the 1 nm oxide surface. There is also a significant variation in the number of steps on the 1 nm oxide surface for a 200 nm image size. There is only 1 step in some images and as many as 8 steps in others. A strong dependence of roughness exponent on step number is observed when images are categorized in terms of the number of steps that are present, images with 5-8 steps have scaling exponents of 0.65-0.95 and RMS roughness of 0.13-0.19 nm, images with 2-4 steps have scaling exponents of 0.4-0.6 and rms roughness of 0.09-0.14 nm, and images with only 1 step have scaling exponents of 0.2-0.3 and rms roughness of 0.08-0.09 nm. These data may be represented differently by measuring the total step length, the sum of all the

individual step lengths, in each 200 nm square AFM image. Figure 3.5 b) shows the effective exponent and rms roughness as a function of the total step length in an image. The $2H_{eff}$ value and the roughness both increase roughly linearly with increasing net step length, with ranges of ~ 0.3 - 0.9 and ~ 0.08 nm - 0.18 nm respectively.

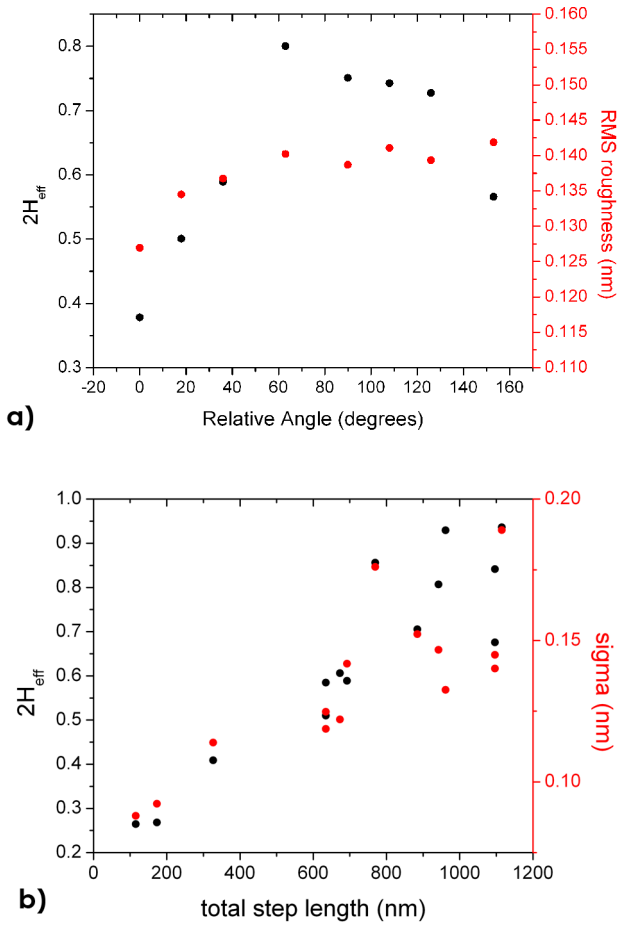

Figure 3.5: Correlation of step density with roughness characteristics. a) Effective exponent as a function of measurement angle with respect to the step edge. Angles relative to the average step orientation, with 0 degrees parallel to the step edge. b) Effective exponent vs. the sum of the length of all steps in an image.

The density of steps affecting the one-dimensional correlation function can also be varied depending on the relative orientation of the x-direction of Eq. 3.1, and

the step edges. To corroborate the effects of step density, correlation functions were also calculated in discreet directions perpendicular and parallel to the step direction and for a variety of angles in between for two sample images from the data set taken with tip 3 on the 1 nm oxide (Table 3.4). Figure 3.6 shows an image of an AFM scan with only 1 step and an AFM scan with 7 steps and the corresponding 1d correlation functions for a variety of directions (angle 1 = 63° from horizontal, angle 2 = 45° from horizontal, angle 3 = 27° from horizontal, angle 4 = horizontal, angle 5 = 27° from horizontal, angle 6 = 45° from horizontal, angle 7 = 63° from horizontal, angle 8 = vertical). For the image with 7 steps we can see a large difference in the correlation function in slope, correlation length, and RMS roughness. For the image with only 1 step all *1d* correlation functions are more similar. Fits were also performed on these *1d* correlation functions and the fit parameter *2H* is graphed as a function of angle number in Figure 3.5a. From this analysis it is clear that the 1 nm oxide surface is smooth, or facetted, on each step terrace (directions parallel to the step) and the correlation function behavior is rough, or self-affine, when measuring perpendicular to step directions.

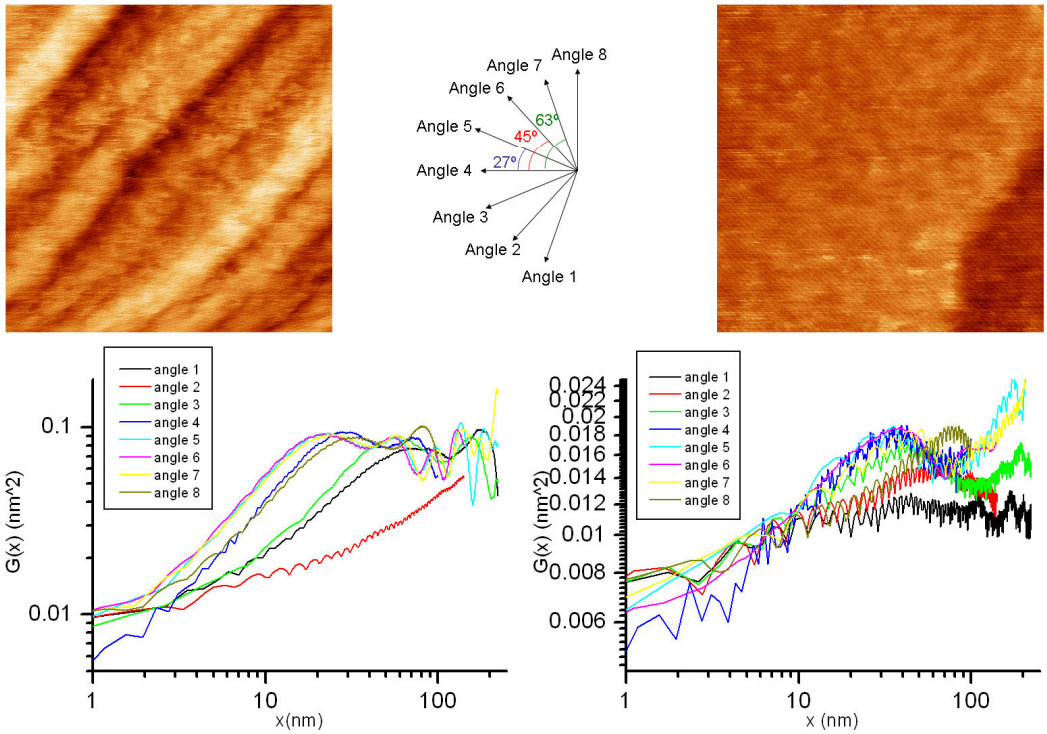

Figure 3.6: *1d* height-height correlation functions for an image with many steps (left) and 1 step (right) are shown at a variety of angles. Both images are from the data set listed in Table 3.4, tip 3. For the left image angle 2 is parallel to step direction and angle 6 is perpendicular to step direction. For the right image angle 1 is parallel to step direction and angle 5 is perpendicular to it. For the left image, the fit for the scan direction parallel to the step direction is *2H*~0.44. For the right image, the fit for the scan direction parallel to the step direction is *2H*~0.20.

3.4 Discussion and Conclusions

The thermal oxide surfaces have uniform, isotropic roughness across large areas of the surface with an average rms roughness of 0.18 ± 0.03 nm. Their correlation functions show power-law behavior over a limited length scale, with an effective roughness exponent of ~1, as is expected for self-affine surfaces[45]. As expected, the thin oxide is much smoother than the 300 nm thick commercial oxide as shown by smaller effective roughness exponents ($2H_{eff}$) and rms roughness values (σ), and longer correlation lengths (ξ). For the stepped thin oxide, step density is found to strongly affect the roughness of the surface, causing variations in effective

roughness exponent from ~ 0.2 at the smallest step density to a value comparable to that of the thick thermal oxide, ~ 0.9, at the largest step density. Extrapolating the dependence of rms roughness on step density yields a limiting roughness of ~0.09 nm for a thin oxide region devoid of steps. At the highest step densities the roughness approaches that of the thick thermal oxide (~0.2 nm).

Data	Total Step Length (nm)	$2H_{eff}$	σ (nm)	ξ (nm)	A	b	A_{min} (nm)
Thin 8 steps	1050	0.93	0.19	20	0.0056	1.20	0.0027
Thin 4 steps	700	0.58	0.12	22	0.0057	1.00	0.0021
Thin 1 step	50	0.26	0.09	30	0.0042	0.88	0.0021
Thick C	-	1.14	0.20	13	0.0053	1.40	0.0023
Thick A	-	1.00	0.15	21	0.0039	1.22	0.0025
Thick B	-	1.09	0.22	15	0.0059	1.35	0.0028

Table 3.5 - Analysis of images for three thin-oxide samples with different step densities, and the thick oxide sample. The effective correlation function exponent $2H_{eff}$, surface roughness σ and correlation length ξ are shown in comparison with the parameters of the Fourier analysis, prefactor A and exponent b, where $A(q) = Aq^{-b}$, along with the limiting amplitude A_{min} observed at large q.

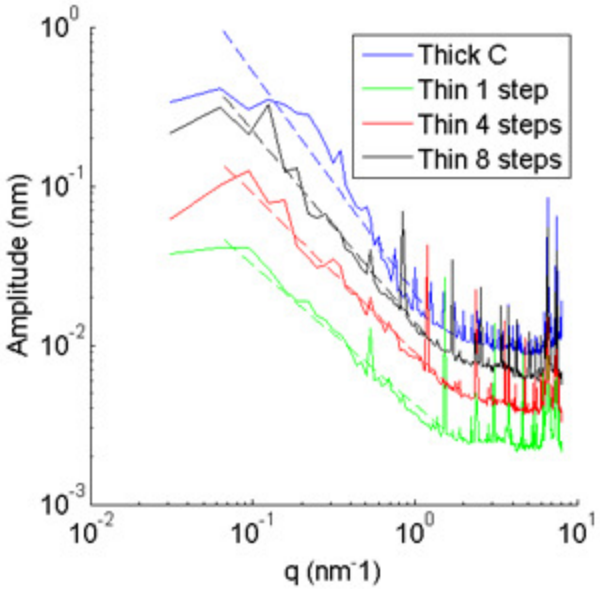

Figure 3.7: Amplitude vs. wave-vector for three thin-oxide samples with different step densities and the thick oxide sample. Dashed lines are fits corresponding to data of the same color. Curves are shown with rigid offsets for clarity; Thin 1 step offset 0, Thin 4 steps offset 0.2, Thin 8 steps offset 0.4, and Thick C offset 0.6.

While the correlation functions provide an empirical basis for comparing the characteristics of different surfaces, the range of power law behavior is limited to one factor of 10 or less variation in distance. Thus a full scaling description [43] is not justified, and a more direct investigation of the underlying structure is needed. To accomplish this, we have carried out one-dimensional Fourier transforms of the images to extract the amplitude of the roughness as a function of the wavelength. The results are listed in Table 3.5 and illustrated in Fig. 3.7 for three thick-oxide surfaces, and three thin oxide surfaces with different step densities. At large wavevector q (wavelengths less than ~4 nm), the decreasing measured amplitude saturates at A_{min}~0.002-0.003nm, most likely due to instrumental limitations. With decreasing q, the amplitude varies as Aq^{-b}, and thus as $A'\lambda^{b}$, where the exponent b is measured to be monotonically increasing with the measured roughness exponent $2H_{eff}$. The dependence of the amplitude on wavevector can be used to determine the local

curvature of the substrate, believed to be important for understanding graphene transport [29,46]. Using the minimum measured amplitudes (last column of Table 3.6) at the maximum wavevector sampled q_{max} = 8.04 nm^{-1}, a lower limit for the smallest local radius of curvature is obtained as $\rho_{ll} = 1/A_{\min} q^2 = 5.7 - 6.3nm$. By extrapolating the power-law region to q_{max} to estimate the true smallest amplitude A_{ext}, $\rho_{ul} \approx 1/A_{ext} q^{-b+2}$, an upper estimate for the minimum local radius of curvature range is found, with a range of 22 - 54 nm for the different oxide surfaces. The general result is that the curvatures imposed by the surface are very gentle - much larger than the radius of a carbon nanotube for instance. The results indicate that native substrate roughness is not likely to perturb the transport characteristics of supported graphene. However, controlling substrate roughness by use of oriented step bunches [47], controlled etching [48], or ultimately by lithographic patterning [49] may provide interesting control effects for graphene or organic electronic TFTs on the substrate.

Chapter 4: Graphene Background

4.1 Physical Structure

Graphene is a 2D lattice of *sp2*-bonded carbon atoms with a repeating hexagonal structure as shown in Figure 4.1. Graphene has two distinct atoms per unit cell, shown in this figure at locations A and B. The graphene unit vectors, also pictured, are

$$\vec{a}_1 = \frac{\sqrt{3}a}{2}\hat{x} + \frac{a}{2}\hat{y}$$

$$\vec{a}_2 = -\frac{\sqrt{3}a}{2}\hat{x} + \frac{a}{2}\hat{y}$$

where a is the lattice constant, for graphene a=0.142 nm[50]. Graphite is composed of many layers of graphene stacked on top of each other with an interlayer distance of $c/2$ = 0.335 nm[50]. The natural stacking of graphene layers within graphite is the A site stacked directly above the B site in consecutive layers with no rotation between consecutive graphene layers[15]. Turbostratic graphite, which has no order between graphene layers, has also been synthesized[50].

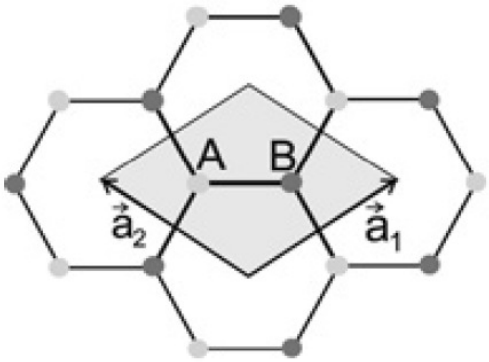

Figure 4.1: 2D graphene lattice is shown with filled gray and black dots as carbon atoms. Each atom shares *sp2* bonds with its nearest neighbors in plane and has a weak out of plane π orbital. Atoms located at A and B are distinct. The unit cell is shaded gray. Taken from reference[50].

4.2 Fabrication of Graphene

Graphene was first observed on SiO_2 substrates with optical microscopy in 2003[[51]]. Graphene had not been previously experimentally realized due to its low optical contrast. The added path length difference caused by SiO_2 substrates allows interference to occur that, for oxide thicknesses of 90 and 300 nm, maximizes graphene's contrast[25]. Typically, graphene is isolated by mechanical exfoliation; the procedure of rubbing a piece of highly ordered graphite on a SiO_2 substrate and shearing single or multiple layers of graphene from the bulk[51,52]. Fabricating graphene by mechanical exfoliation yields high quality samples but has low throughput.

Many other routes of graphene fabrication by different growth mechanisms are being pursued at this time. Epitaxial growth of graphene on 6H polytype silicon carbide substrates is performed by heating the SiC in ultra-high vacuum, which causes the silicon atoms to sublimate from the substrate[53]. The graphene quality is controlled by applying a contrary silicon flux to control the rate of thermal decomposition[53]. Graphene is also being grown by chemical vapor deposition on a

number of metals including nickel[54], copper[55], and ruthenium[56]. The growth mechanism on each of these metals depends on the pressure and temperature used and perfecting each technique to yield high quality, large domain size, single-layer samples is a topic of current research.

Production of graphene nanoribbons (GNR) has been accomplished by "unzipping" carbon nanotubes, slicing them lengthwise so they unroll[57]. GNR differ from graphene in band structure because scattering is dominated by the nanoribbon edges[57]. This method is interesting because controlling the physical dimensions and edge termination (zig-zag or armchair) of these GNR allows control of their transport properties. For example, armchair nanoribbons have bandgaps, a desirable property of graphene for transistor applications[58]. Additionally, some groups have attempted intercalation of graphite with calcium or potassium molecules[59]. Graphene can be fabricated from a graphite intercalation compound if the intercalation molecule is exposed to an enviroment that causes it to release enough energy to separate graphite into individual sheets[59].

4.3 Electronic Structure

Graphene's electronic properties are dictated by its band structure. The band structure of graphene was calculated using the tight binding approximation long before graphene was physically realized[60]. The tight-binding approximation assumes that, in the vicinity of each lattice point, the lattice Hamiltonian can be approximated by the Hamiltonian of a single atom located at that lattice point[15]. Wavefunction solutions to the Schrodinger equation must vanish at distances equal to the lattice

constant (Slater-Koster scheme) and the periodicity of the entire lattice must be imposed[15].

Graphene's reciprocal lattice vectors are given by

$$\vec{b}_1 = \frac{2\pi}{\sqrt{3}a}\hat{x} + \frac{2\pi}{a}\hat{y}$$

$$\vec{b}_2 = -\frac{2\pi}{\sqrt{3}a}\hat{x} + \frac{2\pi}{a}\hat{y}$$

and the lattice constant in reciprocal space is $4\pi/\sqrt{3}a$ [[61]]. Only electrons that are not *sp2*-bound, and are therefore covalently bound in the out of plane p_z bonds, contribute to transport in graphene so only these electrons are considered[61]. Also, for ease, only nearest neighbor interactions are allowed[61]; this will turn out to be a good approximation near the K point of the Brillouin zone where the Fermi surface of the charge neutral graphene lies[58]. To solve the tight-binding model the secular equation, $\det[H - ES] = 0$, is solved for $E_i(\boldsymbol{k})$ at high symmetry lattice points (specific $\boldsymbol{k}$)[61]. The Hamiltonian is defined by $H_{ij}(\vec{k}) \equiv \langle \Phi_i | H | \Phi_j \rangle$ and the overlap intergral matrix is defined by $S_{ij}(\vec{k}) = \langle \Phi_i | \Phi_j \rangle$ where Φ_i are Bloch wavefunctions and $i, j = 1,...,n$ and n is the total number of wavefunctions[61]. Because there are only 2 atoms per unit cell, the Hamiltonian and overlap matrix are 2 x 2, $H = \begin{pmatrix} H_{AA} & H_{AB} \\ H_{BA} & H_{BB} \end{pmatrix}$, and describe hopping between lattice sites A and B (nearest neighbors)[61]. H_{AA} and H_{BB} are equal to the energy of the $2p_z$ orbital at each site, E_{2p}. The off-diagonal matrix elements of H are related by $H_{BA} = H_{AB}^*$ and account for the 3 nearest neighbors;

$H_{AB} = t(e^{i\vec{k}\cdot\vec{R}_1} + e^{i\vec{k}\cdot\vec{R}_2} + e^{i\vec{k}\cdot\vec{R}_3}) = te^{ik_x a/3} + 2te^{-ik_x a/2\sqrt{3}} \cos\left(\frac{k_y a}{2}\right)$ where $t \approx$ -3.0 eV[61].

Since the wavefunctions will be normalized, the diagonal elements of the overlap matrix will equal 1; $S_{AA} = S_{BB} = 1$[61]. And because the tight-binding approximation requires wavefunctions to vanish at distances of their nearest neighbor, $S_{AB} = S_{BA} \sim 0$[61]. Given these values of *H* and *S*, the secular equation can be solved for ***E(k)*** to give

$$E(\vec{k}) = \pm t\sqrt{1 + 4\cos\left(\frac{\sqrt{3}ak_x}{2}\right)\cos\left(\frac{ak_y}{2}\right) + 4\cos^2\left(\frac{ak_y}{2}\right)} \qquad (4.1)$$

where the sign denotes the transport of holes or electrons[61]. Graphene's dispersion relation is plotted in Fig. 4.2. In its ground state, the Fermi energy occurs at E=0 at the 6 infinitesimal points where the conduction (red) and valence (blue) bands meet. Applying a gate voltage to graphene shifts the Fermi level and results in electron or hole conduction.

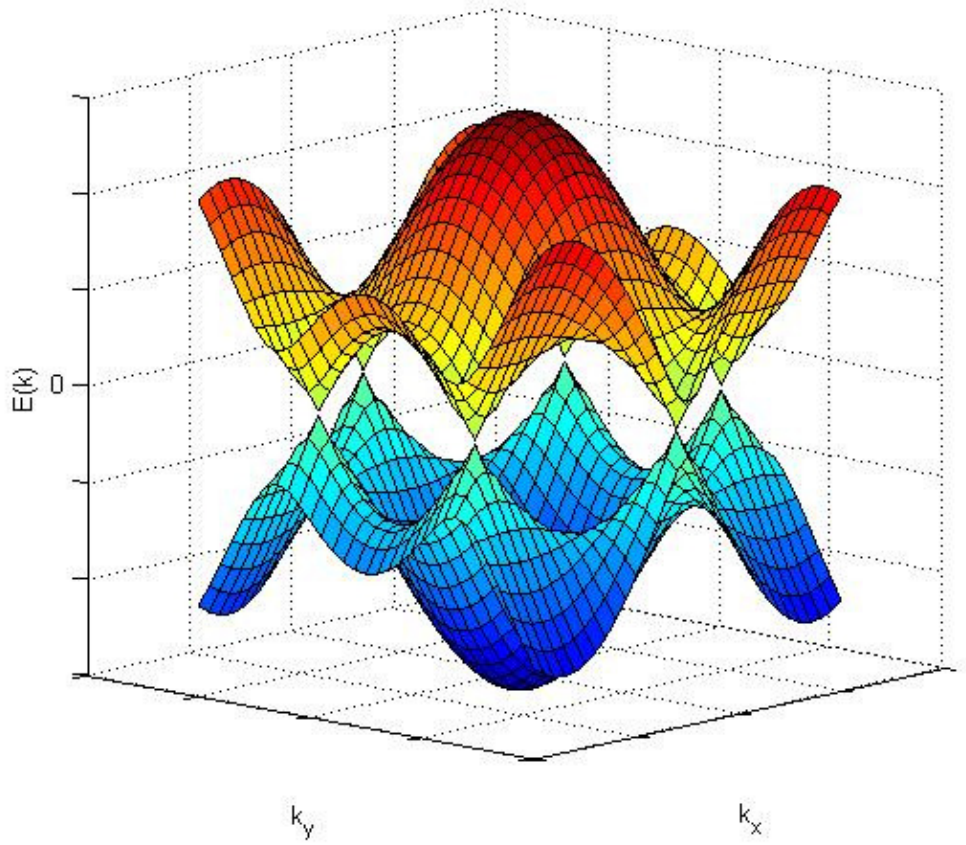

Figure 4.2: Graphene's dispersion relation *E(**k**)* is shown.

Graphene's measured dispersion relation, *E(**k**)*, has been measured with angle-resolved photoemission spectroscopy to match the calculated one (Eq 4.1)[62]. The band structure can also be measured by changing the local potential by using a gate. This will change the Fermi energy and therefore the density of carriers in the graphene. The black data in Fig. 4.3 are graphene's conductivity as a function of gate voltage in UHV as measured by Chen[63]. The data is symmetric for electron and holes and linear as predicted from Eqn 4.1[58]. Colored lines represent the addition of charged impurities (potassium) onto the graphene and have the effect of decreasing

the conductivity and broadening the region of minimum conductivity[63]. Graphene conductivity as a function of gate voltage differs from the calculated dispersion relation at its plateau of minimum conductivity, instead of a sharp point. The plateau is caused by trapped charges in the silicon oxide substrate that cause electron or hole puddles in the graphene and create a finite minimum conductivity[64,65]. Graphene also has very high mobilities similar to those of its parent graphite[51].

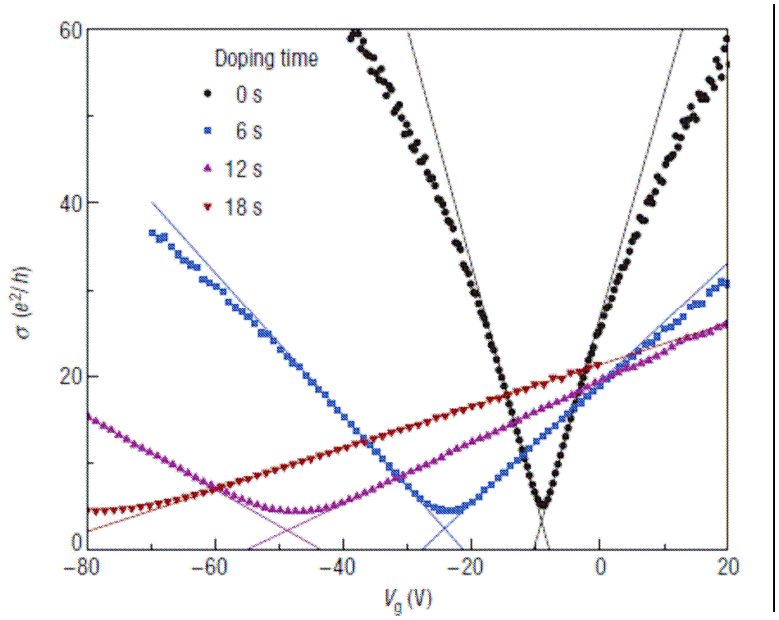

Figure 4.3: Conductivity as a function of gate voltage is shown for a pristine piece of graphene in ultra-high vacuum (black line). Potassium impurities are added to the chamber and the conductivity decreases. Taken from Chen[63].

4.3 Raman Spectroscopy of Graphite and Graphene

Identifying single-layer graphene from 2 or more layers is a major challenge in graphene fabrication since each graphene layer is only 3 angstroms thick. Graphene can be identified optically by measuring its unique contrast on SiO_2 substrates of known thickness[25]. However, ellipsometery must be used to identify oxide thickness precisely and contrast must be measured quantitatively, reducing the

ease of optical identification. Atomic force microscopy can be used to count subsequent layers on graphene's surface, but a typical height measurement of the first graphene layer on SiO_2 is anywhere from 1-1.6 nm due to different forces of interaction between graphene, SiO_2 and the AFM tip[24]. Scanning tunneling microscopy[24], transmission electron microscopy[66], and photoemission electron microscopy[67] all image graphene but are not conducive to micromechanical exfoliation on silicon oxide substrates and/or damage graphene. Raman microscopy is the only non-destructive spectroscopic technique that allows differentiation between graphene and bi-multilayers[68].

Raman scattering occurs when photons scatter inelastically from a material. Unlike Rayleigh scattering, where the incident photon and scattered photon have identical energy, Raman scattering occurs when the incident photon changes the vibrational, rotation, or electronic energy of a material and the scattered photon leaves the molecule with a different energy[69]. When the scattered photon has a lower energy than the incident photon the Raman scattering process is referred to as the Stokes process; when the scattered photon has higher energy than the incident the process is anti-Stokes[69]. In crystals, only discrete phonon modes, or lattice vibrations, may absorb energy from the incident photon[15]. The inelastic scattering process involving the incident and scattered photon and the absorption or emission of a phonon must conserve energy and crystal momentum ($\mathbf{k}$)[15].

The Raman spectrum of graphene differs dramatically from the spectrum of 2 or more layers in its G' (also called 2D) peak located around 2650 cm^{-1} as shown in Figure 3.4 (c)[68]. The G' peak for graphene can be well described by a single

Lorentzian peak shape. However, 2 or more layers have a G' peak that better resembles a sum of 4 Lorentzians. This peak is associated with zone boundary phonons involved in fourth order processes referred to as "double resonance"[68]. The double resonance process involves 4 virtual transitions shown in Fig. 4.4 a) and b) in the order $a \to b \to c \to b \to a$ [68]. A photon of laser energy ε_L is absorbed by an electron of wave vector **k** located near the K point of the Brillouin zone ($a \to b$)[50]. Then a phonon of wave vector **q** inelastically scatters this photon to a circle around the K' point where the photon's new wave vector is **q**+**k** ($b \to c$)[50]. An opposite phonon scatters the electron back to the circle surrounding K where its wave vector returns to **k** ($c \to b$)[50]. Lastly, the electron recombines with a hole and emits a photon ($b \to a$)[50].

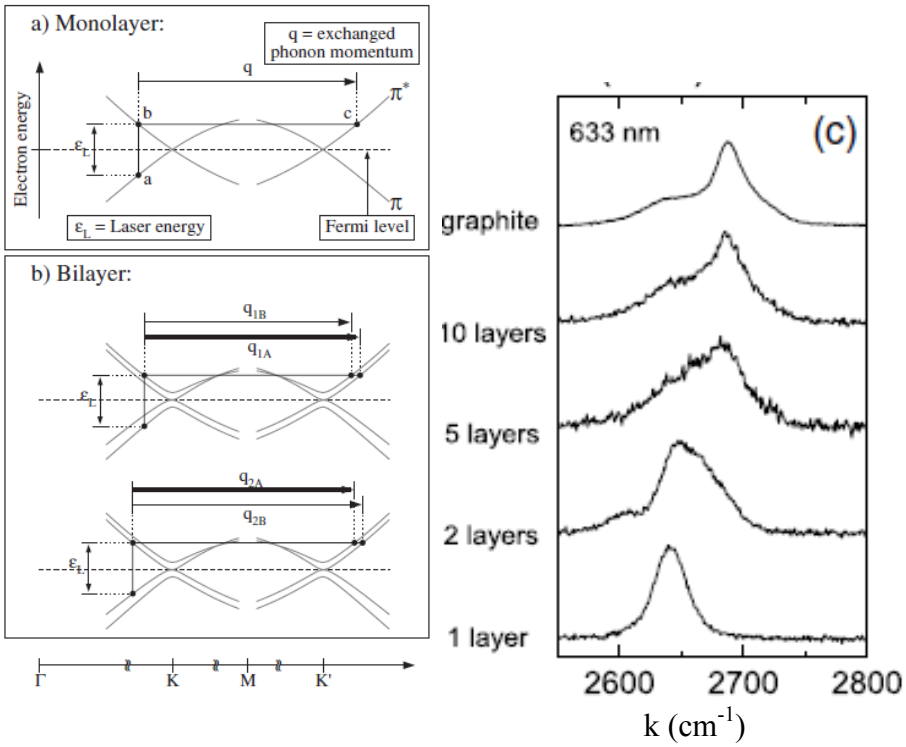

Figure 4.4: Double resonance phonon process which causes G' Raman peak for a) graphene and b) bilayer. (c) Evolution of Raman spectra from graphene to graphite. Taken from Ferrari[70].

Another peak located around 1580 cm^{-1} also appears in graphene and multi-layer spectrum. This G peak is related to the doubly degenerate (in-plane transverse optical and in-place longitudinal optical) phonon modes at the Brillouin zone center, also known as the E_{2g} mode referring to the symmetry at this point (Γ)[50]. Figure 4.5 (b) shows the phonon modes of graphene at points of high symmetry in the graphene Brillouin zone as well as a spatial depiction of these points (a). This G peak decreases in intensity only in graphene's spectrum, but the change is less quantitative than the change in the shape of the G' peak[68]. A third peak can appear in the Raman spectrum of graphitic materials located around 1350 cm^{-1}. This peak is associated with a graphene edge, or defects[68].

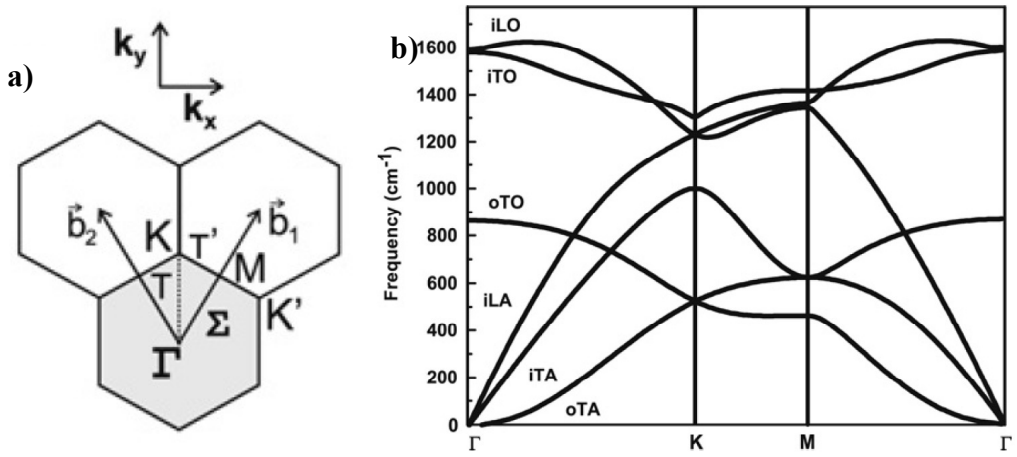

Figure 4.5: a) graphene reciprocal space is shown with the first Brillouin zone shaded grey. Points of high symmetry Γ, K, K', and M are noted. (b) All phonon modes of graphene are shown between points of high symmetry; i = in plane, T = transverse, L = longitudinal, O = optical, and A = acoustic. Figures taken from Dresselhaus[50].

Chapter 5: Self-Assembled Monolayers as a Graphene Substrate

5.1 Introduction to Self Assembled Monolayers

Self assembled monolayers (SAMs) are defined as "highly ordered molecular assemblies that form spontaneously by chemisorption of functionalized molecules and organize themselves laterally, most commonly by van der Waals interactions between monomers" [71]. A SAM is typically composed of a long chain of molecules with a functional group on one or both ends. When one of the functional groups bonds with a complimentary substrate, the monolayer self-assembles in order to accommodate the maximum number of molecules bound to the substrate. When all bonding sites are occupied a monolayer has self assembled as shown in Fig. 5.1.

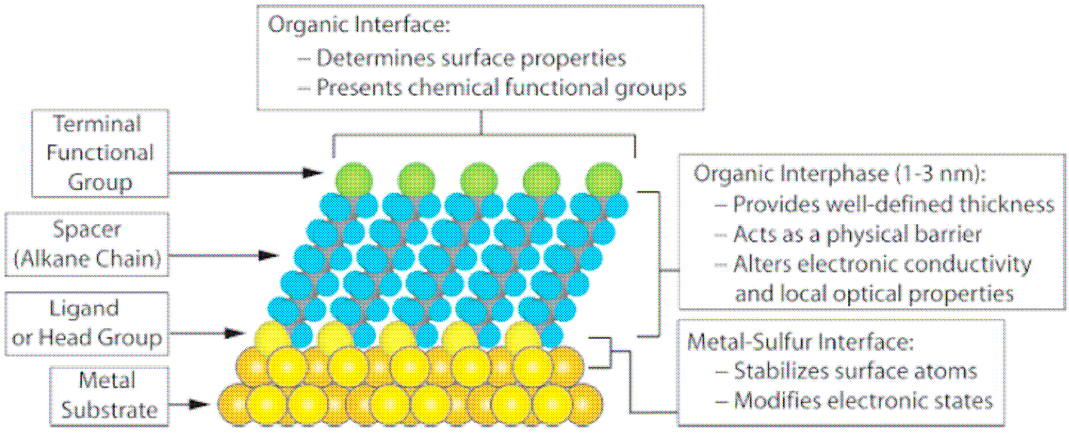

Figure 5.1: A self assembled monolayer forms by bonding to all sites on a substrate, here metal. Taken from reference[72].

The hydrophobicity and/or surface free energy of a surface may be tailored by choice of the functional group of a SAM[71]. Patterning can be performed in conjunction with any of these techniques to yield a wide range of applications in molecular electronics, optical devices, and sensing[71].

In our studies, SAMs have been used to alter the morphological, chemical, vibrational, and energetic properties of a 300 nm SiO_2 substrate for use with graphene field effect transistors. Graphene is difficult to find on most surfaces due to its height and transparency causing low optical contrast. For this reason, graphene is typically mechanically exfoliated onto 300 nm silicon oxide because it is one of few surfaces that provides maximum contrast[25]. Because graphene is only fabricated and measured on one type of surface, it is difficult to conclusively know which properties are intrinsic to the graphene and not caused by the oxide. Altering the oxide's properties provides one way of determining which properties are intrinsic to graphene. For example, Chen has shown graphene mobilities are dramatically decreased at room temperature due to SiO_2 phonon scattering[73]. Also, some critical degree of curvature in a graphene FET should adversely affect electrical performance. Altering SiO_2 morphology will begin to illuminate the role substrate morphology plays in shaping graphene.

The SAMs for this procedure require a functional group at one end that bonds strongly to SiO_2. Trichlorosilanes were chosen since many varieties of trichlorosilanes are available from commercial chemical retailers and some studies of their properties have been previously reported[74].

5.2 Experimental Procedure

The trichlorosilanes studied were 11-cyanoundecyltrichlorosilane (CUTS), 3-aminopropyltriethoxysilane (APTES), phenyltrichlorosilane (PTS), and 1H,1H,2H,2H-perfluorodecyltrichlorosilane (FDTS), shown in Fig 5.2. FDTS, CUTS, and PTS were taken as received from the manufacturer (Sigma Aldrich and Gelest)

and moved into a nitrogen glove box. Plastic syringes and glass ampules from Chemglass were also moved into the glove box. The syringes were used to transfer the trichlorosilane to the glass ampules, which were then sealed in the nitrogen environment and removed from the glove box. The nitrogen and trichlorosilane filled ampules were then evacuated using a mechanical pump.

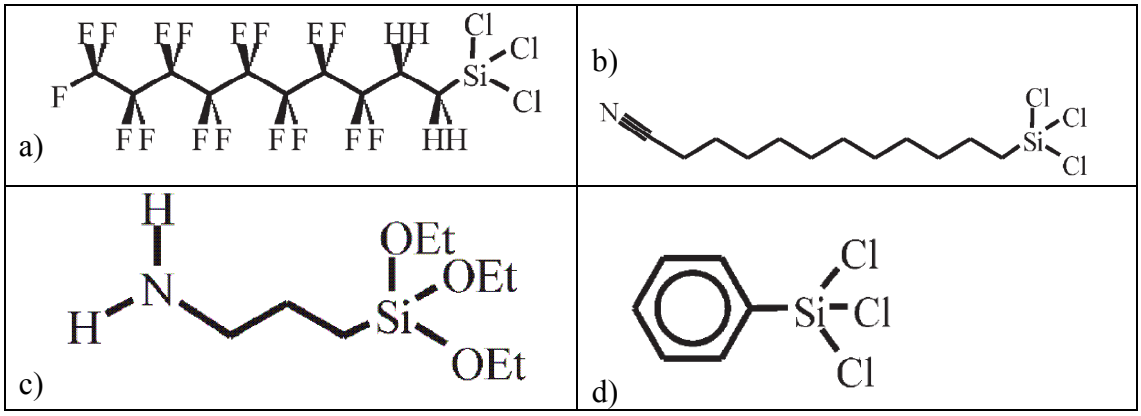

Figure 5.2: The chemical structure of the SAM used in this work reproduced from Janssen et al[74]. SAMs are a) FTDS, b) CUTS, c) APTES, and d) PTS.

Commercial 300 nm SiO_2 wafers were purchased from Silicon Quest International and cleaned in acetone, methanol, and isopropyl alcohol. Wafers were placed in a home-made chamber and the previously evacuated, air-tight glass ampule filled with a liquid trichlorosilane was attached to this chamber. The chamber was sealed and evacuated to a pressure of 50 mTorr using a mechanical pump. The chamber was isolated from the pump and the pump was stopped. Then the ampule was opened to the chamber so the trichlorosilane vapor filled the chamber and coated the SiO_2 wafer. The ampule remained open for two hours to encourage formation of a full monolayer.

APTES was deposited according to the manufacturer's recommended procedure [67]. APTES was mixed in air in a ratio of 1:50 with acetone. SiO_2 wafers

were soaked in the solution for 2 minutes immediately following solution preparation. Soaked wafers were rinsed two times in de-ionized water and allowed to dry overnight. SAM coverage for all SAMs was studied with contact angles and x-ray photospectroscopy and atomic force microscopy.

Graphene was mechanically exfoliated onto all SAM covered wafers according to the following procedure. A very small piece of Kish graphite or highly ordered pyrolytic graphite (HOPG) (highest grade) was attached to a piece of scotch tape parallel to the hexagonally bound crystal orientation. Another piece of scotch tape was attached to this ensemble, sticky sides touching, and removed. Peeling tape apart one or more times gives the graphite a static charge that yields better results upon exfoliation. When the graphite has been charged by this procedure fine point tweezers are used to pull a very small piece of graphite from the bulk graphite on the tape. This piece of graphite is placed on a piece of 300 nm SiO_2 wafer in a gel pack. Another 300 nm SiO_2 wafer piece is placed on top of it and they are pressed together firmly using plastic tipped tweezers. Finally, force is applied to the top wafer using plastic tip tweezers in a direction perpendicular to the wafer and the angle between the force and the wafer face is decreased until the top wafer slides off the bottom one. An optical microscope is then used to search both wafers for high quality graphene pieces. Raman microscopy is used to confirm the graphene identification.

Characterization of the samples was carried out using contact angle measurement, XPS, AFM and (for graphene) Raman spectroscopy and transport measurements. Results for each of these approaches are presented in the following sections.

5.3 Contact Angle Background

Consider a drop of liquid on a surface surrounded by a vapor as shown in Fig. 5.3. If these three phases can be considered to be in thermodynamic equilibrium, as proposed by Thomas Young[75], they would be described by

$$\sum F = \gamma_{SL} - \gamma_{SV} + \gamma_{LV}\cos\theta = 0 \qquad (5.1)$$

where γ_{lv} is the liquid-vapor surface tension, γ_{sl} is the solid-liquid surface tension, and γ_{sv} is the solid-vapor surface tension also defined as the surface free energy. The contact angle, θ, is defined as the angle formed between the solid and the tangent to the surface of the liquid.

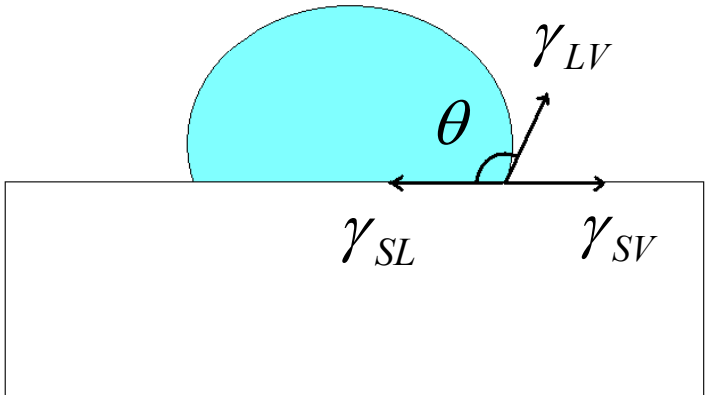

Figure 5.3: Contact angle in equilibrium with surrounding vapor on solid surface with the labeled interfacial tensions.

The surface free energy of the surface may be a quantity of interest since it predicts adhesiveness of the surface. When the two other surface tensions and the contact angle are known, the surface free energy may be determined. However, γ_{sl}, the solid-liquid surface tension, is not a readily known quantity for most solid-liquid combinations.

Crucial advances in this problem were made by Fowkes in 1964[76]. He proposed that all materials are made up of polar and dispersive components[76].

$$\gamma = \gamma^d + \gamma^p \tag{5.2}$$

The forces acting on a molecule at an interface between two surfaces are the sum of the attractive force to other molecules in the bulk and the London dispersive force. The interfacial tension on one liquid is the sum of these forces.

$$\gamma = \gamma_2 - \sqrt{\gamma_1^d \gamma_2^d} \tag{5.3}$$

Therefore the total interfacial tension is the sum of these two tensions.

$$\gamma_{12} = \gamma_1 + \gamma_2 - 2\sqrt{\gamma_1^d \gamma_2^d} \tag{5.4}$$

This analysis can be applied to the liquid-solid interface[76].

$$\gamma_{SL} = \gamma_S + \gamma_L - 2\sqrt{\gamma_S^d \gamma_L^d} \tag{5.5}$$

If the previous analysis is applied to the solid-vapor or liquid-vapor interface, one finds that $\gamma_{SV} = \gamma_S$ and $\gamma_{LV} = \gamma_L$. When equation (5.5) and (5.1) are combined they yield

$$\gamma_S - \gamma_L \cos\theta = \gamma_S + \gamma_L - 2\sqrt{\gamma_S^d \gamma_L^d}$$

$$\gamma_L (1 + \cos\theta) = 2\sqrt{\gamma_S^d \gamma_L^d} \tag{5.6}$$

This theory was later expanded by Owens and Wendt to include polar forces in the analysis[77]. They account for polar forces across interfaces changing equation (5.3) to

$$\gamma = \gamma_2 - \sqrt{\gamma_1^d \gamma_2^d} - \sqrt{\gamma_1^p \gamma_2^p} \tag{5.7}$$

and, therefore, equation (5.6) to

$$\gamma_L(1+\cos\theta) = 2\sqrt{\gamma_S{}^d \gamma_L{}^d} + 2\sqrt{\gamma_S{}^p \gamma_L{}^p} \ . \qquad (5.8)$$

Using this approach, a number of test liquids of known polar and dispersive components may be dropped on a surface being studied, and the dispersive and polar components of the solid interfacial tension, or surface free energy, may be determined. The total surface free energy of the solid is merely the sum of these two components, by equation (5.2). Typically the polar and dispersive components are determined by re-writing equation (5.8) as

$$(1+\cos\theta)\frac{\gamma_L}{2\gamma_L{}^p} = \sqrt{\gamma_S{}^d}\,\frac{\sqrt{\gamma_L{}^d}}{\sqrt{\gamma_L{}^p}} + \sqrt{\gamma_S{}^p}$$

and fitting a line to all data points, each created by a different liquid, that yields a slope of $\sqrt{\gamma_S{}^d}$ and an intercept of $\sqrt{\gamma_S{}^p}$.

A variant on this description has been developed by Lifshitz, who attributes interfacial forces as a mostly dispersive component and two components that account for the chemical nature of the materials[78]. The dispersive component differs from that of Fowkes and Owens in that it takes into account small contributions from orientational and induction terms[78]. The other components of the surface free energy are terms due to acidic and basic (or donor and acceptor) interactions[78]. In this Lifshitz-van der Waals (LW) description, the interfacial energy may be written as

$$\gamma = \gamma^{LW} - 2\sqrt{\gamma^- \gamma^+} \qquad (5.9)[79]$$

where the superscript '–' refers to the Lewis-base (electron-donor) component and '+' refers to the Lewis-acid (electron-acceptor) component of the surface free energy[79].

The relationship between the contact angle and surface free energy components of liquid and solid is therefore

$$\gamma_L(1+\cos\theta) = 2\sqrt{\gamma_S{}^{LW}\gamma_L{}^{LW}} + 2\sqrt{\gamma_S{}^{-}\gamma_L{}^{+}} + 2\sqrt{\gamma_S{}^{+}\gamma_L{}^{-}} \,. \qquad (5.10)^{79}$$

In theory, a contact angle description of a surface is highly informative, but in reality many factors complicate this description. For example, all real surfaces have some roughness at some height scale. Obviously, an extremely rough surface will not result in the equilibrium shown in Fig. 5.3 and will not be described by Eq. 5.1, but at what roughness does this description deviate significantly? Furthermore, is the assumption that the liquid-vapor-solid system reaches equilibrium a valid one? It has been shown that contact angles behave hysteretically on a variety of surfaces[80,81] especially on polymer[82] or chemical monolayer substrates[83] due to chemical or structural changes within the surface and/or substrate roughness[81]. Using contact angles as a formal means of describing physical properties of a substrate presents some challenges. However, the surface free energies extracted from the contact angle measurements in this study will provide a good comparison with each other. We will use these values to determine the changes to the silicon oxide that are caused by the self-assembled monolayers.

5.4 Contact Angle Results

Immediately after SAM deposition, as described in section 5.2, contact angles were measured. For each SAM and for bare SiO_2, the wafer was diced into 15 pieces and cleaned with pressurized N_2 only. One drop of test liquid, in ambient temperature and humidity, was placed on the SAM of study. Three pictures of the drop were taken immediately at different focuses; the drop, the substrate, and the best focus of both

together. This step was repeated for three different drops for each liquid/SAM combination. Five total liquids were used; water, ethylene glycol, glycerol, diiodomethane, and formamide. Literature values for the total, dispersive, polar, lifshitz-van der Waals, acid, and base components of each liquid are summarized in Table 5.1. The camera and stage level system used are part of a commercial Rame-Hart goniometer.

Liquid	γ_L	γ_L^d	γ_L^p	γ_L^{LW}	γ_L^-	γ_L^+
Water	72.8	21.8	51.0	21.8	25.5	25.5
Ethylene glycol	48.0	29.0	19.0	29.0	1.92	47.0
Glycerol	63.4	37.0	26.4	34.0	3.92	57.4
Diiodomethane	50.8	48.5	2.3	50.8	0	0
Formamide	59.2	39.5	18.7	39.0	2.28	39.6

Table 5.1: All surface free energy components of the five test liquids are presented in units mN/m. All Lifshitz model surface energy components are from Radelczuk et al[79]. All Fowkes model surface free energy components are from Kaeble[84].

Both contact angles for each drop were measured and averaged using an IDL program which outputs texts files containing the contact angle for all of the nine total measurements (pictures) taken for each liquid/SAM combination. These text files are then used to compute the surface free energy components of the solid for both the Fowkes and Lifshitz models. For each model the 243 different possible combinations of 9 data points for each of the 5 liquids are computed for each SAM. The average and standard deviation of these combinations is reported. This calculation was automated with Matlab programs for the Fowkes and Lifshitz models. A summary of the measured results compared with literature values for each SAM (where possible) is shown in Table 5.2 for the Fowkes model and Table 5.3 for the Lifshitz model.

	γ_S	γ_S^d	γ_S^p	Literature γ_S
300 nm SiO_2	45.3 ± 0.2	20.3 ± 0.6	25.0 ± 0.6	77.36 ± 0.02[74]
FDTS	12.3 ± 1.0	2.1 ± 1.0	10.2 ± 1.9	13.50 ± 0.12[74]
PTS	37.6 ± 0.2	9.7 ± 0.5	27.9 ± 0.6	37.64 ± 0.04[74]
CUTS	34.4 ± 0.7	15.0 ± 2.0	19.4 ± 1.4	41.33 ± 0.04[74]
APTES	40.3 ± 0.5	17.1 ± 0.3	23.2 ± 0.5	45.25 ± 0.03[74] - 50.7 (on mica)[85]

Table 5.2: Surface free energy components in mJ/m^2 for each SAM calculated using the Fowkes model. Literature values have been calculated using the same method.

	γ_S	γ_S^{LW}	γ_S^-	γ_S^+	Literature γ_S
300 nm SiO_2	45.5 ± 0.4	36.4 ± 0.8	1.0 ± 0.1	21.6 ± 0.7	77.36 ± 0.02[74]
FDTS	16.6 ± 1.1	15.5 ± 0.6	0.1 ± 0.1	3.0 ± 1.0	13.50 ± 0.12[74]
PTS	40.6 ± 0.3	38.0 ± 0.5	0.1 ± 0.0	12.5 ± 0.8	37.64 ± 0.04[74]
CUTS	34.5 ± 0.5	29.7 ± 0.4	0.3 ± 0.1	18.1 ± 3.3	41.33 ± 0.04[74]
APTES	40.8 ± 0.7	34.7 ± 0.5	0.5 ± 0.1	19.9 ± 0.7	45.25 ± 0.03[74] - 50.7 (on mica)[85]

Table 5.3: Surface free energy components in mJ/m^2 for each SAM calculated using the Lifshitz model.

No reference data for silicon oxide is provided because the surface free energy of a silicon oxide surface depends on many factors including the thickness of the oxide[86], the surface cleaning procedures[87], and oxide roughness[86]. For example, Thomas grew silicon oxide substrates of various thicknesses and found that the advancing contact angle of water on these surfaces increased from 35° – 52° for oxide thicknesses of 3 – 500 nm[86]. Our contact angle for water on our 300 nm silicon oxide surface is about 56°. However, Williams finds that contact angles of water on thermally grown silicon oxide substrates ranges from 90° – 0° with a sharp transition in angles occurring at an oxide thickness of 3 nm[88]. In this study, oxide thickness has been varied by growing a 300 nm oxide and then etching it away with hydrofluoric acid (HF) to the desired thickness[88]. Frieser studied the effect of different surface treatments on silicon oxide substrates and found that boiling the oxide in deionized

water decreases the water contact angle 50° – 10°[87]. A variety of unsystematic chemical surface treatments have also been performed on silicon oxide substrates and studied with contact angle measurements[87,89]. Stoneham suggested that the contact angle will depend on the location and number of trapped charges in the silicon oxide, but he only considers the data generated by Williams, not oxides that were exposed to different surface treatments[90].

Our thermally grown 300 nm silicon oxide sample is comparable to those studied by Thomas. His home grown samples have a water contact angle of about 50° which is similar to the water contact angle on our sample. Our cleaning procedure of organic solvents differs from his lack of cleaning procedure and may account for the slight difference in our measurements. Some cleaning procedures for silicon have been previously studied by ellipsometery[91] and other techniques, but no systematic study has been performed using contact angle measurements. A systematic study of surface cleaning procedures needs to be performed to understand the effect they have on the surface free energy of a substrate.

Results show that the surface free energy for all SAMs is lower than the surface free energy of the original oxide. Therefore, it should be more difficult to mechanically exfoliate graphene onto any of the SAMs studied than onto the original oxide surface. However, adhesion and friction between two surfaces will likely depend on additional factors like electrostatic forces between the surfaces as well as the surface energy of each.

5.5 XPS Results

X-ray photospectroscopy (XPS) is a technique that detects the chemical composition on the surface 1-10 nm of a material. X-rays with energy $h\upsilon$ are directed at a sample in vacuum at a shallow angle[92]. These photons induce the ejection of a core level electron from the material as shown in Fig. 5.4[92]. The kinetic energy, E_K, of the photoelectron is measured, but the binding energy, an intrinsic property of each element, may be determined by conserving energy,

$$E_B = h\upsilon - E_K - \phi \tag{5.11}$$

where ϕ is the work function of the spectrometer[92]. XPS was performed at the University of Maryland, Department of Chemistry XPS facility. XPS technique can not detect hydrogen and it always detects adventitious carbon due to its presence in the vacuum chamber at all times. A control spectrum obtained for bare SiO_2 indicated that oxygen was 45% of the surface composition, silicon was 25%, and (adventitious) carbon was 30%.

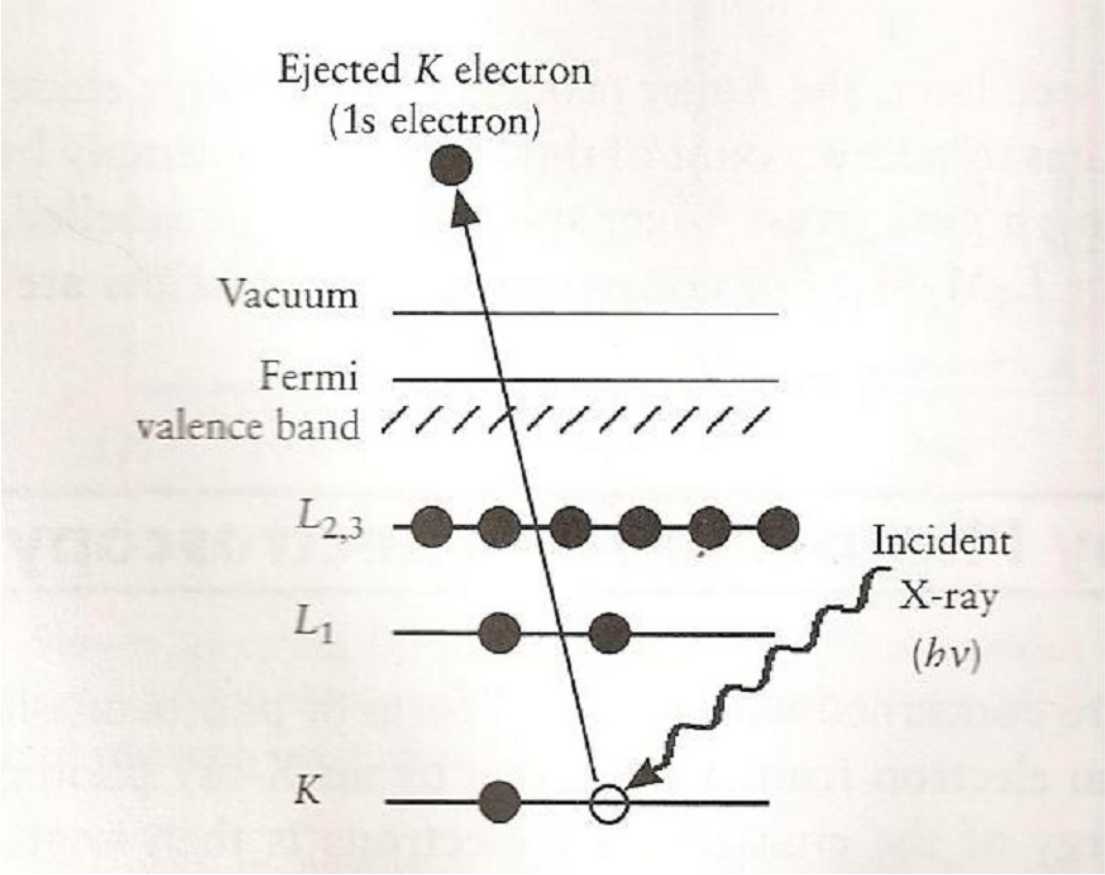

Figure 5.4: Schematic of XPS where a 1s photoelectron is ejected[92].

The results of the XPS are shown in Fig. 5.5. For 3 of 4 SAMs some signature of the monolayer was observed, confirming the monolayer's presence. The strongest signal was observed for FDTS; 20% of the surface atoms were fluorine in this case. The other atoms present in the FDTS sample were O (*1s*) 36%, C (*1s*) 24%, and Si (*2p*) 19%. Given the 10 nm maximum probe depth of the XPS technique and the 1.8 nm length of the FDTS molecule[93], we expect to measure a large signal from the silicon and oxygen. The relative concentrations of F to O (0.55) or F to Si (1.05) does not suggest we have less than a full monolayer of coverage. Flourine's signal strength is expected due the flourination of the entire carbon chain (Fig. 5.2 (a)), whereas

other monolayers have detectable functional groups only at the end of the carbon chain.

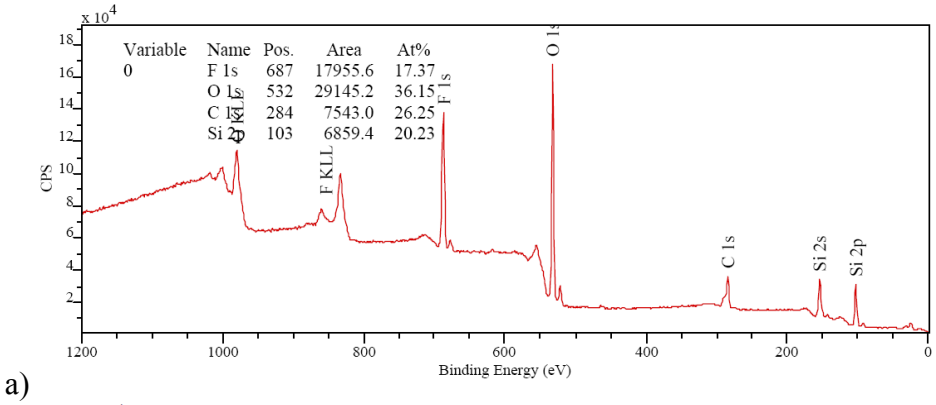

a)

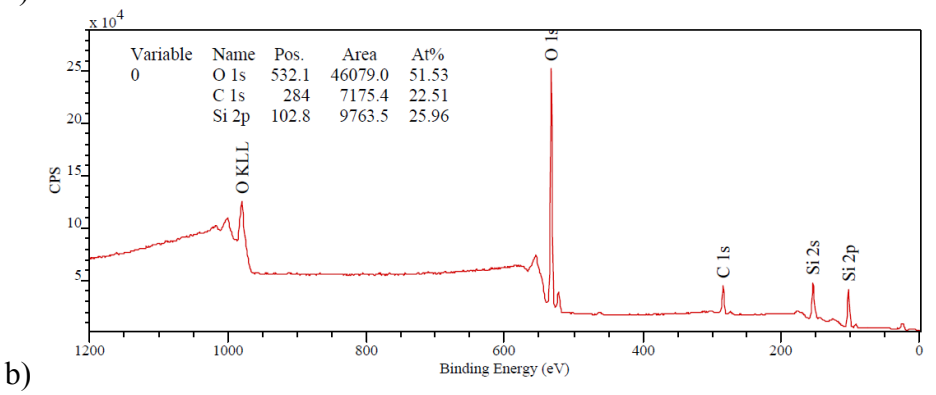

b)

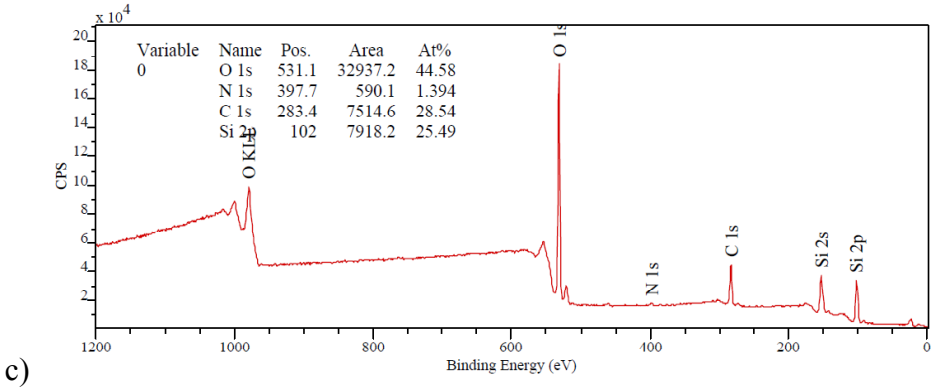

c)

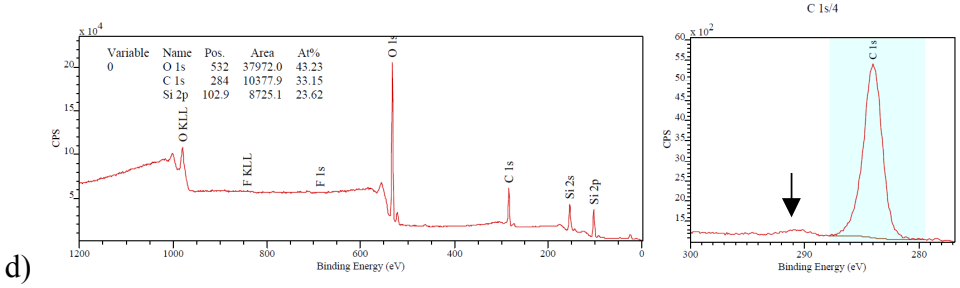

d)

Figure 5.5: XPS data for monolayers a) FDTS, b) CUTS, c) APTES, and d) PTS. All data was taken by the University of Maryland Department of Chemistry XPS facility.

APTES is an example of such a monolayer; the nitrogen is the only element expected to have an XPS signature and only one nitrogen exists per molecule, so nitrogen is found to be only 1.4% of the surface composition (Fig. 5.5 (c)). PTS is the third SAM that gives an XPS signature. The PTS monolayer is composed of only carbons and hydrogens that individually would not be detectable by XPS. However, when H and C form a phenyl group, as they do here (Fig. 5.5 (d)), they have a weak pi-pi shake-up satellite signal[94]. Shake-up satellites are found at slightly higher binding energies than the C *1s*, O *1s*, and Si *2p* peaks[94]. We observe a shake-up satellite signal for the PTS monolayer around 290 eV, near the C *1s* peak, as shown in Fig. 5.5 (d). The monolayer CUTS was not detected by XPS (Fig. 5.5 (b)). Similarly to APTES, nitrogen is the only molecule that should be detectable with this technique but no there is no count increase near 400 eV, the N *1s* binding energy[95].

5.6 AFM Measurement and Scaling Analysis

Morphological changes to the SiO_2 substrate caused by SAM deposition were studied extensively using the same analysis outlined in Chapter 3. Many AFM images of each surface were taken after SAM deposition and corrected using SPIP software in the same way described in Chapter 3. A representative image of each is shown in Fig. 5.6. The 2D height-height correlation function for corrected images on each SAM was computed and is shown in Fig. 5.7. The RMS roughness, σ, correlation length, ξ, and scaling exponent, 2H, were computed from these correlation functions for all SAMs and these values compared to the values for the original silicon oxide substrate are shown in Table 5.4.

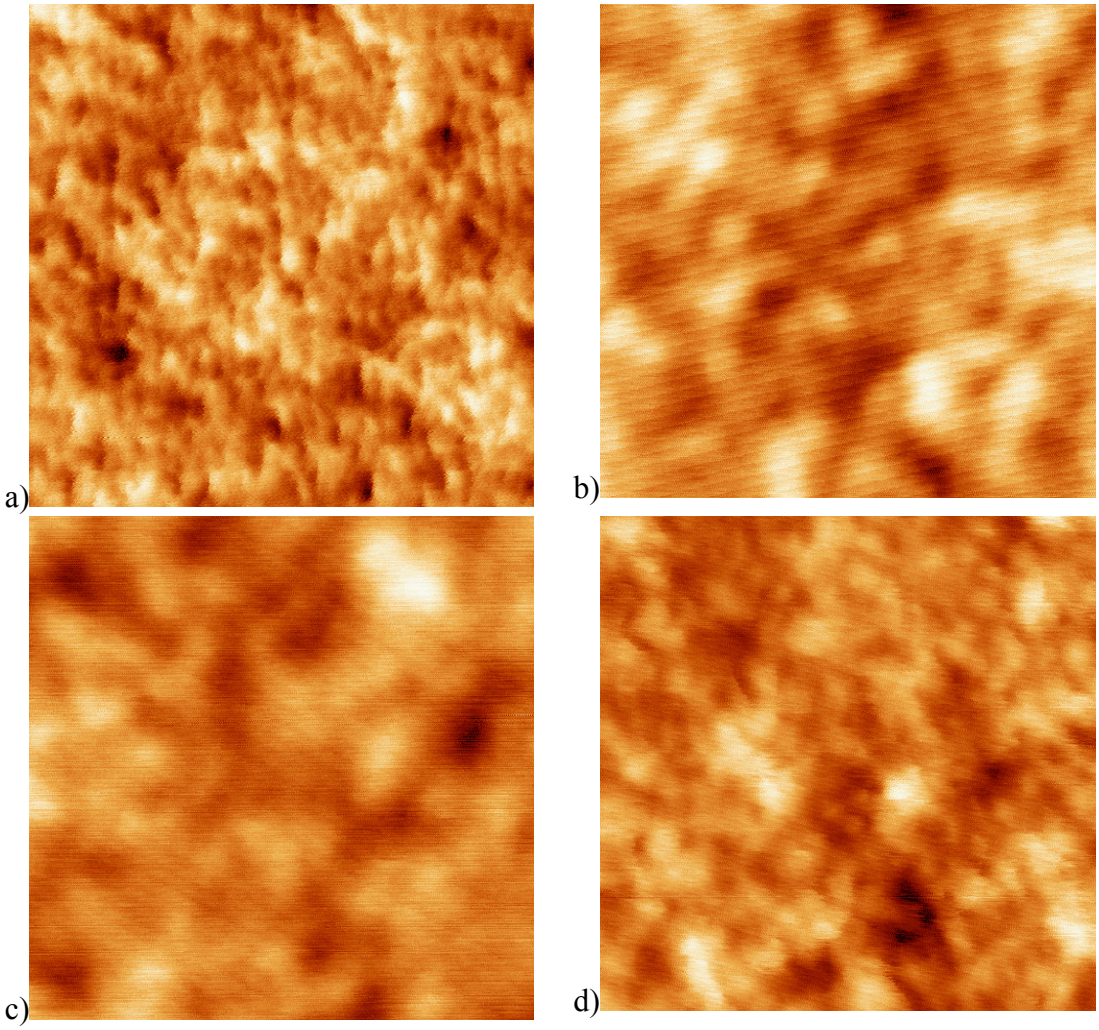

Figure 5.6: Corrected AFM image of a) FDTS, b) CUTS, c) APTES, and d) PTS on SiO_2. Each image size is 200 nm x 200 nm taken at 512 lines and 512 points per line.

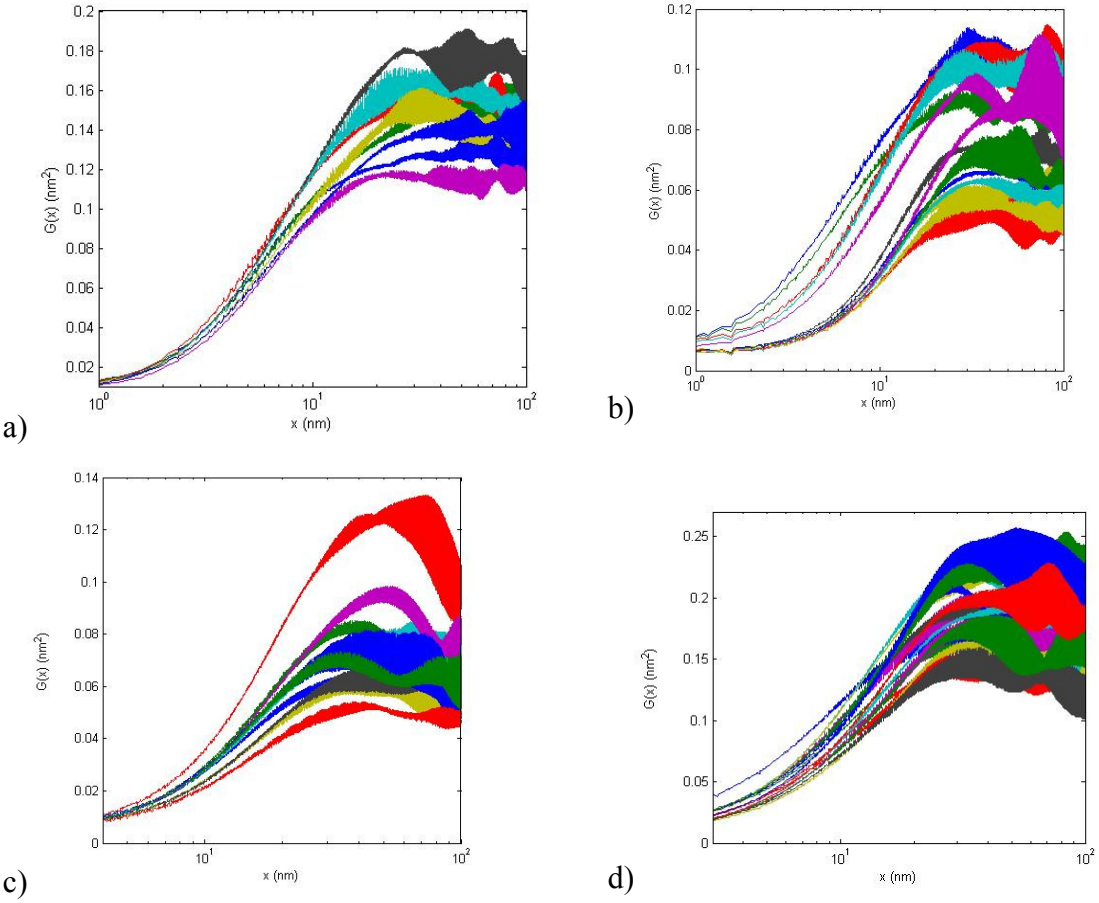

Figure 5.7: Height-Height correlation functions of corrected AFM images on a) FDTS, b) CUTS, c) APTES, and d) PTS on SiO_2. Colors correspond to different, arbitrary AFM images.

	2H	ξ (nm)	σ (nm)
300 nm SiO_2	0.97 ± 0.11	15.9 ± 2.8	0.18 ± 0.03
FDTS	1.12 ± 0.03	10.2 ± 0.7	0.27 ± 0.02
PTS	0.78 ± 0.14	21.0 ± 1.4	0.29 ± 0.02
CUTS	0.65 ± 0.19	20.7 ± 1.7	0.19 ± 0.02
APTES	0.99 ± 0.09	22.9 ± 0.7	0.18 ± 0.02

Table 5.4: Scaling exponent, correlation length, and RMS roughness for SiO_2 and all SAMs.

The morphology of the silicon oxide substrate is altered by some SAMs. For FDTS and PTS, the RMS roughness is increased. For FDTS only does the scaling exponent, *2H*, increase. FDTS literature does not provide scaling analysis information, but FDTS thickness and roughness have been studied through

ellipsometry, FTIR, AFM, and TEM measurements[93,96]. For FDTS monolayers dip-coated onto tetrahedral amorphous carbon films, the RMS roughness of the original substrate was about 10% smaller than a monolayer coverage of FDTS on the substrate[93]. Partial coverage of the carbon film substrate by the FDTS resulted in RMS roughness up to 46% larger than the original substrate. We measure the FDTS layer which also has a 50% higher roughness than the original substrate, suggesting FDTS has only partially covered the silicon oxide. However, the magnitude of our FDTS roughness is smaller than the roughness of the original carbon film substrate in the work by Zhang and our substrates and preparation methods are not identical.

I have performed a simulation to model the RMS roughness of FDTS as a function of percent coverage. I began with a real AFM image of 300 nm silicon oxide that I measured as described previously. I assumed an FDTS molecule can be located at each pixel of the AFM image, so each pixel either retains its original value or is 1.8 nm greater than its original value. I systematically varied the number of FDTS molecules and plotted the resulting RMS roughness as function of FDTS coverage in Fig. 5.8. I varied the SiO_2 AFM image and observed that the minimum RMS roughness always occurs at 0 and 100% coverage and the values are equivalent. Also, the curve shape remains the same and the maximum RMS roughness occurs at 50% coverage and has a value of ~0.75 nm greater than the RMS roughness of the silicon oxide (0% coverage). We have experimentally measured FDTS layers with RMS roughness 0.05 nm greater than that of the original silicon oxide substrate. In the model system, an RMS roughness of 0.05 nm occurs at 1 or 99% coverage. If the height of the FDTS is only 0.9 nm, then a difference in RMS roughness of 0.05 nm

occurs at 3 or 97% coverage. In reality, molecular assembly may not be ideal; some molecules may occur at intermediate heights. Therefore this roughness is a lower bound to the true roughness of the surface.

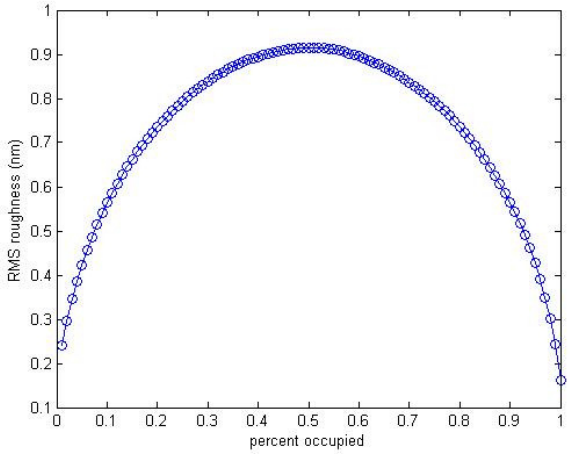

Figure 5.8: RMS roughness is computed as a function of percent coverage of a silicon oxide substrate of RMS roughness 0.162 nm as it is covered by ideal FDTS molecules of height 1.8 nm.

Roughness studies of PTS monolayers formed on Mo sputtered on glass substrates showed the PTS monolayer decreased the substrate roughness from 1.66 to 1.00 nm[97]. Comparison of our results with the ones reported in this study is difficult since our original substrate is about 1 order of magnitude smaller in RMS roughness. The same numerical simulation can be applied to PTS molecules, of length 0.428 nm[98], as they cover the same silicon oxide substrates. We find the maximum RMS roughness of 0.107 nm for a PTS layer occurs at 50% coverage. Our experimentally measured RMS roughness for a PTS layer is 0.11 nm larger than the roughness of the original substrate. This calculation indicates that we probably have a partial layer of PTS whose coverage is approximately 50%.

The mean grain size of APTES films on a SiO_2 substrate has been measured as 0.47 nm in height and 20 nm in width and its average roughness, R_a, is reported to be 0.5 nm[99]. The average roughness and the RMS roughness are defined as

$$R_a = \frac{1}{n}\sum_{i=1}^{n}|h_i| \tag{5.12}$$

$$R_{RMS} = \sqrt{\frac{1}{n}\sum_{i=1}^{n}h_i^2} \tag{5.13}$$

respectively, where h_i is the height from the mean at one (x,y). A relationship can be determined between the RMS and the average roughness to assist in comparing the literature results with measured data. Starting with the Cauchy-Schwarz inequality,

$$(\mathbf{x}\cdot\mathbf{y})^2 \le (\mathbf{x}\cdot\mathbf{x})(\mathbf{y}\cdot\mathbf{y}), \tag{5.14}$$

where **x** and **y** are two vectors of length n. Then, if we define we define $\mathbf{y} = [1,1,...1]$ and $\mathbf{x} = [h_1, h_2, ...h_n]$ the Cauchy-Schwarz inequality becomes

$$\left(\sum_{i=1}^{n}h_i\right)^2 \le \left(\sum_{i=1}^{n}h_i^2\right)(n)$$

$$(nR_a)^2 \le \frac{1}{n}\sum_{i=1}^{n}h_i^2 n^2$$

$$R_a \le \sqrt{\frac{1}{n}\sum_{i=1}^{n}h_i^2}$$

$$R_a \le R_{RMS} \tag{5.15}$$

Despite this relationship, the average roughness measured by Gu is 0.5 nm[99] and is not smaller than our measured RMS roughness of about 0.2 nm. However, the resolution limit of the images taken by Gu was large (0.1 nm) and the scan size was 1 micron, in comparison to our instrument resolution limit 1 pm and images taken with

a scan size of 200 nm. There are no reports on the morphology of CUTS surfaces at this time.

For all SAMs the FFT was computed on one sample image. The Fourier amplitudes and exponents (*A* and *b* defined in Chapter 3) were similar to those reported for the commercial silicon oxide substrate with *A* ranging from 0.0035 to 0.0166 nm and *b* ranging from *–0.95* to *–1.32*. The lower limit of the radius of curvature, which is computed by $\rho_{ll} = 1/A_{\min} q^2$ at maximum *q* and corresponding *A*, as outlined in Chapter 3, ranges from 3.4 nm for APTES to 4.1 nm for FDTS. These values are similar to those for the original oxide surface and are not likely small enough to affect graphene transport properties. Therefore, we may infer that any alterations in graphene transport behavior are due to the changed chemical environment caused by the presence of the terminal functional group of each SAM.

5.7 Raman Spectroscopy of Graphene on SAMs

As discussed in Chapter 4.3, the graphene G peak which occurs around 1580 cm^{-1} is caused by scattering of two degenerate phonon modes near the Brillouin zone center, Γ. Two groups have observed the G peak to narrow and upshift when gated, or when the graphene Fermi energy is changed[100,101],[101]. The FWHM of the G peak in pristine graphene is widened by the Kohn anomaly, in which an electron-hole pair is created in the absorption of a phonon or destroyed in the creation of a phonon[50]. The absorption and creation of these phonon modes significantly alters both the frequency and lifetime of the mode (which should be centered sharply around ~1583 cm^{-1}, see Fig 4.2) widening the G peak[50]. The Pauli exclusion principle requires phonons involved in this process move an electron from the conduction to the valence band (creating an electron-hole pair)[50]. This statement is equivalent to the condition that the Fermi energy be less than half of the phonon energy; $\varepsilon_F < \frac{\hbar\omega_{phonon}}{2}$, as shown in

Fig. 5.9 [50]. Therefore, increasing the Fermi energy reduces the number of phonons involved in the process and increases the energy (frequency) of allowed phonon participants. This is observed as a narrowing and upshifting of the G peak as previously reported by Yan[100] and Pisana[101].

Subsequent work by Das using a top-gated transistor geometry shows the large magnitude of the changes in the G peak correspond to electron concentrations of $\sim 1.5 \times 10^{13}$ cm^{-2} (see Fig. 5.10)[102]. These electron concentrations are much higher than those achievable using the traditional graphene transistor geometry involving a Si back gate separated from graphene by a 300 nm silicon oxide.

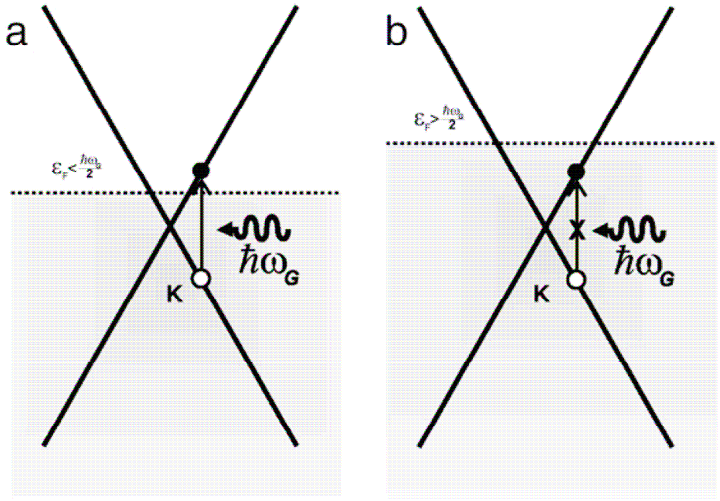

Figure 5.9: a) The creation of an electron-hole pair occurs when the shift in graphene's Fermi energy is less than half the energy of the absorbed phonon. b) The Pauli exclusion principle prohibits the creation of an electron hole pair entirely within the conduction band. Taken from Malard[50].

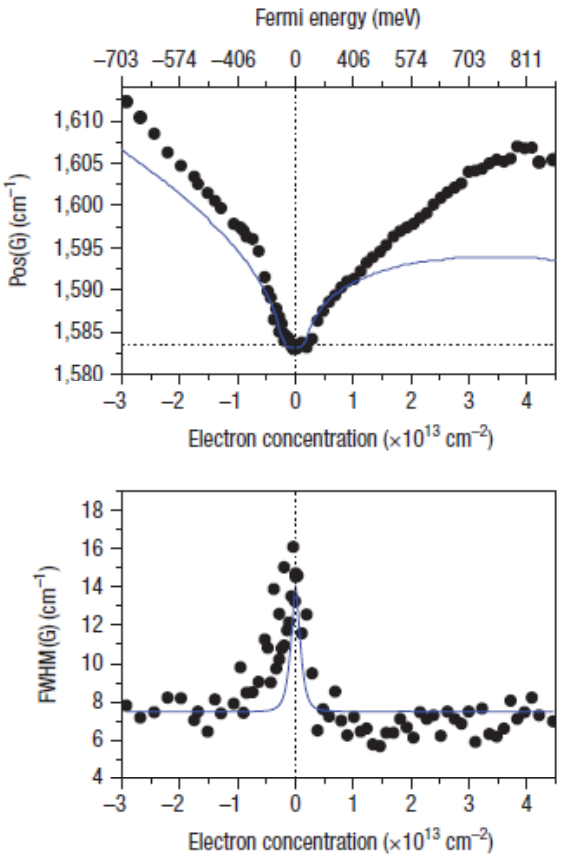

Figure 5.10: The change in position (a) and FWHM (b) of the graphene G peak as a function of carrier density as tuned by a polymer top gate[102]. The blue lines are the predicted non-adiabatic trends. Taken from Das[102].

Graphene has been exfoliated on all SAMs and identified using Raman microscopy. The Raman signatures of graphene on silicon oxide and on all SAMs are shown in Table 5.5. Optical images and corresponding Raman signatures of graphene on SAMs are shown in Fig. 5.11. 5 flakes of graphene were found on FDTS, 1 flake was found on CUTS, 1 flake was found on APTES, 17 flakes were found on PTS, and 7 flakes were found on SiO_2 for comparison. For most SAMs, the graphene Raman signal is unaltered by the presence of the monolayer. However, for FDTS, the G peak and the G' peak are shifted to higher wavenumbers than those of graphene on SiO_2 by 12 and 7 wavenumbers respectively. Also, the full width half max (FWHM) of the G peak for graphene on FDTS is about half of its value on SiO_2, see Table 5.5.

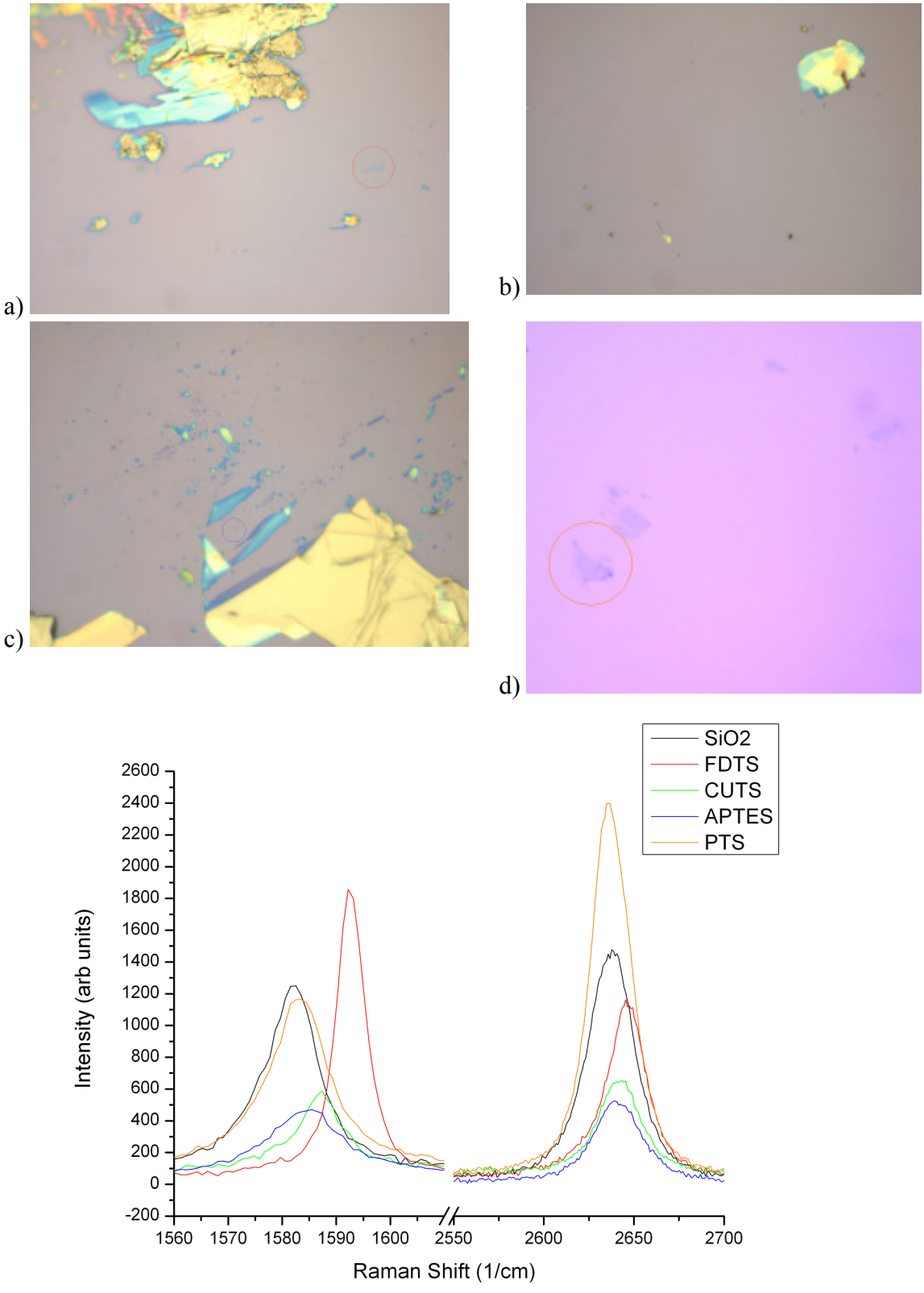

Figure 5.11: Optical images of graphene on a) FDTS, b) CUTS, c) APTES, and d) PTS and e) corresponding Raman spectra.

	G peak position (1/cm)	G peak FWHM (1/cm)	G' peak position (1/cm)	G' peak FWHM (1/cm)
300 nm SiO_2	1581.1 ± 1.7	19.9 ± 6.4	2636.9 ± 4.3	17.8 ± 8.2
FDTS	1593.1 ± 1.8	8.0 ± 2.2	2644.1 ± 3.2	29.7± 5.4
PTS	1583.5 ± 1.4	15.6 ± 1.7	2638.2 ± 1.5	26.0 ± 1.6
CUTS	1587	15.6	2641	30.2
APTES	1584	18.9	2641	30.2

Table 5.5: Statistics compiled on Raman spectra for graphene on SAMs. Lorentzian function was fit to G and G' peaks to find peak location, the error is the standard deviation. No statistics are available for CUTS and APTES since only one piece of graphene was identified on each of these monolayers.

SAM	Similar molecule	Electron affinity (eV)
SiO_2	SiO_2	0.95
FDTS	CF_3 or F_2	1.82 or 3.01
PTS	C_6H_6	-1.14
CUTS	C_6N_4	2.88
APTES	NH_2	0.77

Table 5.6: Electron affinities of molecules similar to the terminal group of each SAM.

The electron affinities of molecules similar to the terminal groups of each self assembled monolayer are listed in Table 5.6. We expect the magnitude of the electron affinity corresponding to each monolayer to follow the same trend that the shift in G peak follows. The two SAMs with the highest electron affinities, FDTS and CUTS, also have the highest position G peaks, though only FDTS exhibits significant narrowing of the FWHM. The other monolayers have electron affinities with similar magnitude to that of SiO_2 and we do not see a significant shift in G peak position or FWHM for these monolayers.

The upshift and narrowing of the G peak observed for graphene on FDTS is dramatic compared to results seen by Yan and Pisana but comparable to the results measured by Das. His top gate uses a solid polymer dielectric to create a strong local field at the graphene. This field causes a large shift in graphene's Fermi energy which changes the width and frequency of the G band. The changes we measure in

graphene's G band on FDTS substrates indicate that FDTS has a strong electron withdrawing characteristic that creates a similar local field at the graphene.

5.8 Transport Characterization

Graphene transport has been reviewed in Chapter 4.2. The dispersion relation, Eq. 4.1, plotted in Fig. 4.2, governs transport. When a gate voltage is applied to graphene, it shifts graphene's Fermi energy and creates an excess of holes or electrons which participate in conduction. We expect graphene's transport behavior on FDTS to be similar to transport of graphene measured by Das at large top-gate voltages since both seem to shift the Fermi energy dramatically. It is difficult to speculate how an additional gate voltage would alter the local field on graphene on FDTS and therefore how the entire device would behave. Since normal graphene device geometry allows induction of charge carrier densities an order of magnitude smaller than the density induced by the FDTS, it is possible gating such a device using the universal silicon gate would be ineffective.

Though the surface free energy of all SAMs allowed exfoliation of graphene, photoresist could not be spun evenly on all monolayers. Since PMMA could not be spun on FDTS, no metal contacts could be fabricated on this monolayer. Therefore, to further investigate the electric properties of graphene on this monolayer, a different device geometry will have to be employed.

A limited number of graphene 2-probe devices were fabricated on CUTS, APTES and PTS and graphene 4-probe devices were fabricated on PTS and APTES. Though 2-probe measurements have contact resistance incorporated, they allow measurement of a lower conductivity limit (or mobility limit) as well as the gate

voltage at which graphene's conductivity minimum occurs. 2-probe measurements taken on graphene on SAMs are shown in Figure 5.12 (a). All measurements are shown for CUTS and APTES, but more than 3 devices were measured on PTS so a representative group is shown. All 2-probe measurements were taken in air at ambient pressure. The best mobilities for APTES, PTS, and CUTS monolayers are 1000 cm^2/Vs, 1400 cm^2/Vs, and 700 cm^2/Vs. These mobilities are low compared to 4-probe graphene mobilities measured in ambient conditions on SiO_2 which range from ~1000-10000 cm^2/Vs. The point of minimum conductivity, or Dirac point, for APTES, CUTS, and PTS occurs at approximately 7, 10, and 15 V respectively. This trend follows the trend in the magnitude of each molecules electron affinity as shown in Table 5.7.

Graphene 2 probe devices	Electron Affinity (eV)	Dirac point (V)	Highest Mobility (cm^2/Vs)
APTES	0.77	7	1000
CUTS	1.14	10	1400
PTS	2.28	15	700

Table 5.7: Location of point of minimum conductivity follows the same trend as the electron affinity of graphene devices.

4-probe graphene devices on PTS were measured in ambient conditions and their conductivities are shown in Figure 5.12 (b). Device electron mobilities are 1300, 2300, 4700, and 6000 cm^2/Vs and Dirac points occur between gate voltages ranging from 6 to 15 V with lower mobility devices having higher shifts in Dirac points. This trend is suggestive of charged impurity scattering, a phenomenon that has been investigated thoroughly by Chen[63]. Though Chen deposited controlled potassium impurities on graphene in UHV, charged impurity scattering is very commonly caused by trapped charges in the silicon oxide substrate. Graphene transport on PTS

resembles graphene transport on SiO_2 and is consistent with charged impurity scattering.

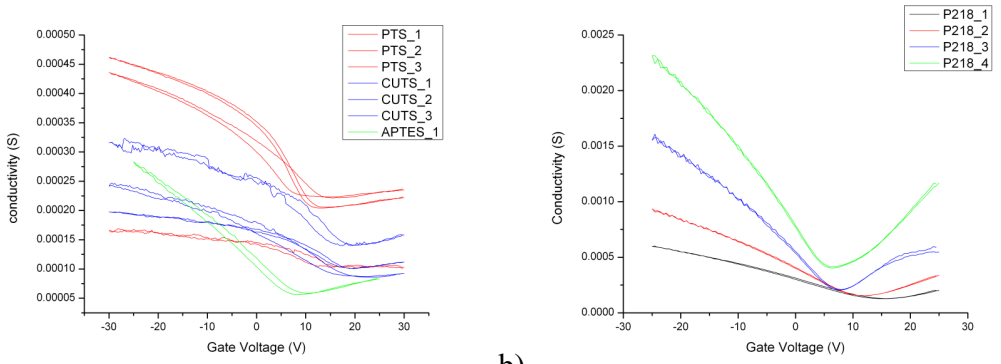

a) b)

Figure 5.12: (a) Two-probe graphene conductivity on certain SAMs is shown. (b) Multiple graphene devices on PTS are measured in 4-probe configuration.

The RMS roughness of the PTS layer suggests that we have partial coverage of the substrate but does not yield any information about the size of the islands. Each PTS molecule has a diameter of approximately 0.28 nm[98] and could be assembling on the substrate in large islands or a by maximizing space between molecules. There will be a gradient in the local field at the edge of each island. If the PTS island size is smaller than the exfoliated graphene, gradients in the field should be analogous to trapped charges in the silicon oxide substrate. This random Coulomb potential causes electron-hole puddles in the graphene layer that are only observable at low carrier densities. This creates a minimum conductivity plateau in graphene (instead of the sharp point predicted by the dispersion relation) near the charge neutrality point[65,103]. The minimum conductivity plateaus measured on PTS layers (Fig 5.12 (b)) are comparable in width to those measured for graphene devices on silicon oxide.

Finally, 4-probe graphene devices have been measured on SiO_2, PTS, and APTES as a function of temperature. These devices were measured in a vacuum of 1x 10^{-6} Torr using a low temperature probe station. Graphene devices were not annealed

in Ar/H for any length of time because SAMs are not stable at temperatures above 200 degrees C. Control devices on SiO_2 were also not annealed to provide a true control. Measurements of conductivity as a function of gate voltage and temperature are shown in Figure 5.12. Two separate control devices are shown in Fig. 5.13 (a) and (b). The gate voltage location of the Dirac point and the minimum conductivity value both shift significantly in one of these control devices, contrary to observations made by Chen[73] and Morovoz[104] in separate studies of graphene conductivity as a function of temperature. Both found that gate voltage location of the Dirac point did not change as a function of temperature[104,73]. Both also found that conductivity decreases with increasing temperature, unlike the data shown here. The two control devices measured here have PMMA residue which may be contributing to molecular absoption and desorption with temperature changes. The graphene device measured on PTS has a dramatically shifted Dirac point, which may be attributed to its age of approximately 3 months. The stability of graphene devices fabricated on the SAMs may be an interesting future experiment. The graphene device on APTES shows less variation as a function of temperature possibly because it was measured over a smaller temperature range. In Chen's study, there was little variation of any parameter over the temperature range 4-80K.

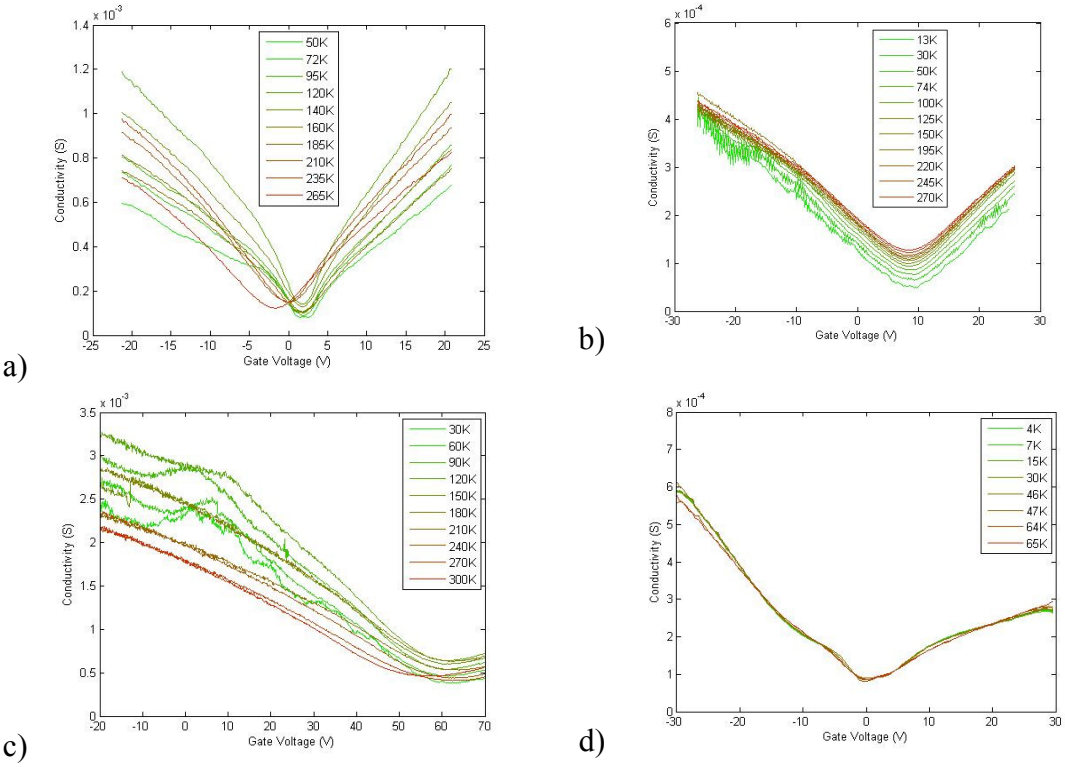

Figure 5.13: 4-probe conductivity as a function of gate voltage and temperature has been measured for graphene on (a-b) 300 nm SiO_2, (c) PTS, and (d) APTES.

5.9 Conclusions

In this chapter, we performed a preliminary survey of the effects of surface polarity on graphene transport by mechanically exfoliating graphene on silicon oxide coated with self-assembled monolayers. The terminal group of the monolayers were chosen to give a range of polarities. A vapor deposition process was developed to deposit the self-assembled monolayers.

SAM surfaces were characterized by XPS, contact angle, and AFM measurements. Contact angle measurements confirmed the presence of a SAM layer. XPS was used to confirm the molecular species of the SAM. Finally, AFM measurements suggested that most layers were in fact monolayers, but PTS layers were most likely a partial layer.

Graphene was mechanically exfoliated onto all surfaces, even the least adhesive, without using additional chemical processing. The Raman fingerprint of graphene was altered by the presence of SAMs with higher electron affinities suggesting that surface polarity has a similar effect to that of a strong gate. The Raman spectra of FDTS monolayers demonstrate this effect most conclusively. However, alternative device fabrication methods need to be developed in order to confirm this effect with transport measurements. Transport in graphene devices on PTS has been measured in four-probe device configuration. Rough PTS substrates with probable patchiness have a strong effect similar to that of charged impurity scattering, possible due to incomplete layer with field variation at edges of patches.

Preliminary measurements in G peak shift for FTDS show evidence that graphene behavior can be strongly modified by surface polarization. However, a more rigorous control of SAM continuity is needed to isolate polarization behavior from effects of film discontinuity. Alternate device geometries for building FDTS transistors would also help distinguish the effect of film discontinuity from surface polarization. Further study of surface modification may result in control of graphene properties.

Chapter 6: Low Frequency Noise in Graphene

Graphene is a promising semiconductor replacement for future low power consumption electronics. Due to graphene's atomic thickness, signal to noise ratio will be an important limiting parameter of such electronics.

In this chapter I discuss measurements I performed of the low frequency (1/*f*) noise in several graphene transistors in a four probe geometry. I found that the inverse of the noise magnitude has an anomalous "W" shaped dependence on carrier density, which differs from the predictions of traditional 1/f noise models of carrier number fluctuations and mobility fluctuations. Instead I found agreement with numerical simulations, carried out by Dr. Enrico Rossi of the University of Maryland, of resistance fluctuations due to random configurations of charged impurities near graphene.

6.1 Introduction to Different Types of Electrical Noise

For a simple circuit consisting of a constant current source and a resistor in series, the voltage across the resistor can be measured. This voltage will vary with time about an average voltage, <V>,

$$V(t) = \langle V \rangle + v(t) .$$

The power spectral density, or noise power, S_V, of this signal is given by the cosine transform of the voltage-voltage autocorrelation function, C_V, of this signal

$$C_V(t) = \langle V(t)V(0) \rangle - \langle V \rangle^2$$

$$S_V(f) \equiv 4\int_0^\infty C_V(t)\cos(2\pi ft)dt \ [^{105}]. \qquad (6.1)$$

This power spectral density behaves differently in different frequency regimes. In higher frequency regimes, shot noise or Johnson-Nyquist noise are likely to dominate the spectrum. Shot noise is caused by fluctuations in the number of discrete charge carriers and has the form $S_I = 2qI$, where q is the elementary charge[106]. Johnson-Nyquist noise, or thermal noise, is caused by thermal fluctuations of charge carriers[106]. This may also be thought of as scattering of charge carriers resulting in randomized velocities of the carriers[106]. The form of the power spectral density of the thermal noise is $S_V = 4kTR$

for a material with a resistance R at a temperature T [[106]]. Both of these forms are white, meaning they average to zero over long times[106].

Generation-recombination (GR) noise is a type of noise observed only in semiconductors, which may occur at a wide range of frequencies including low frequencies[107]. GR noise is caused by the recombination or generation of an electron and hole, or the trapping of an electron or hole by an electronic state located in the gap between the valence and conduction bands[106]. GR noise has power spectral density of the Lorentzian form $S_N(f) = 4\left\langle \Delta N^2 \right\rangle \frac{\tau}{1+(2\pi f)^2\tau^2}$ where τ is the time constant of the transitions (generation, recombination, or trapping)[106]. For a certain distribution of (traps with different) time constants GR can produce a 1/*f* noise power[106]. The noise spectra from individual traps may only be calculated separately and summed if the traps are isolated so they do not interact and if the number of carriers is larger than the number of traps[106]. Random-telegraph-signal noise is a

specific case of GR noise involving very few traps that cause the current signal to switch randomly between two levels. The power spectral density for this type of noise is also Lorentzian.

Low frequency, flicker, or *1/f* noise has a power spectral density that takes the form

$$\frac{S_V}{V^2} = \frac{A}{f^\beta} \tag{6.2}$$

where V is the average voltage at a given source-drain current, A is a dimensionless constant referred to as noise magnitude, f is the frequency, and β is a constant ranging from 0.9-1.4. A lower limit to this type of noise is expected to avoid infinite power at zero frequency but has never been experimentally observed[108]. Low frequency noise is observed to be a bulk effect (inversely proportional to volume) and resistance fluctuations occur in equilibrium (in the absence of driving current)[109].

Many materials are found to obey an empirical relationship between the constant A and the number of carriers called Hooge's law. Hooge's law is

$$A = \frac{\alpha}{N_c} \tag{6.3}$$

where N_c is the number of carriers and α is an intrinsic, material dependent constant. Though Hooge's law describes low frequency noise behavior in many materials including most metals, insulators, semiconductors, and novel materials like carbon nanotubes, the law is strictly empirical[109],[105].

In some semiconductors, low-frequency noise appears to be better described by fluctuations in carrier number[110]. In the case of constant mobility, carrier number fluctuations give $S_R \sim 1/N^2$. Carrier-number fluctuations can be generalized to any

system with a conductivity dependent on carrier number. For a system with a gate-voltage-dependent conductivity $G(V_g)$, a random signal applied to the gate with magnitude S_g will produce noise described by

$$A = \gamma^2 S_g^{\,2} \left(\frac{d \ln G}{dV_g} \right)^2 . \qquad (6.4)$$

where γ is a constant. This result was derived by Tersoff[111] to describe the contact noise in ballistic carbon nanotube transistors whose contact conductance was gate-voltage dependent, however it could apply to any system with a $G(V_g)$; notably for constant mobility (i.e. $G \sim V_g$), one recovers the classic result that $A \sim 1/V_g^{\,2} \sim 1/N^2$.

6.2 Low-frequency Noise in Graphene: Previous Work

Graphene is a distinct new type of electronic material, a zero-gap semiconductor with vanishing density of states at the charge neutrality point (CNP). Experimentally, graphene exhibits a finite conductivity σ at all carrier densities, including the CNP. This apparent "conductivity without carriers" has been explained as arising from disorder which induces a spatially inhomogeneous carrier density. The question arises: What is the noise magnitude at the CNP? Application of Hooge's phenomenological model (Eqn. 6.3) would predict divergent noise as the carrier density is reduced to zero at the CNP, while the carrier number fluctuation model (Eqn. 6.4) would predict zero noise at the CNP, since at the minimum conductivity point the conductivity is not dependent on carrier density (i.e. $d\sigma/dN = 0$).

Low frequency noise in graphene has been the subject of several previous studies. Graphene nanoribbons were first studied by Lin and Avouris[112]. They performed two probe low frequency noise measurements on graphene and bilayer nanoribbons. They found that graphene nanoribbons of 30 nm width exhibited typical low frequency noise behavior following Hooge's empirical law, $A \propto \frac{1}{N_C}$. They observed the noise power was maximum and finite at lowest carrier densities and a Hooge parameter of $\alpha = 1x10^{-3}$ was extracted for graphene nanoribbons. However, bilayer nanoribbons demonstrated an unexpected suppression in noise power at low charge carrier densities. Avouris observed bilayer noise power to be an order of magnitude lower than graphene noise power and to increase monotonically with carrier density[112]. They conclude that the suppression in noise magnitude that is observed in bilayer is due to screening of the trapped charges in the oxide by the first graphene layer but call for a more rigorous theoretical description. Other groups have since performed two-probe low frequency noise measurements on mechanically exfoliated graphene and bilayer with different gate geometries and observed little variation in noise as a function of charge carrier density[113]. We are aware of only one study of low frequency noise in mechanically exfoliated graphene measured in a four-probe configuration performed by Pal et al[114]. The authors measured the noise power, S, using a custom detection technique. They observed a low frequency noise response of one graphene device to be similar to the response observed by Lin and Avouris for graphene nanoribbons; graphene noise magnitude proportional to $1/N_c$[114].The authors suggest more charge carriers allow for greater screening of the trapped charges in the oxide and which causes a decrease in noise power.

More recently, a non-monotonic dependence of the 1/*f* noise on carrier density around the CNP was reported by two groups: Heller et al[115] studying liquid-gated and back-gated graphene devices in a two-probe geometry, and Xu et al.[116] studying back-gated graphene devices in a four-probe configuration. Heller et al. interpreted their observations in terms of number fluctuations (Eqn. 6.4) with an additional unidentified gate-independent series resistance, while Xu et al. interpreted the results qualitatively within Hooge's model (Eqn. 6.3) accounting for charge inhomogeneity in the graphene[65,117]

6.3 Measurement of Low Frequency Noise in Graphene

Graphene devices were prepared by mechanical exfoliation in the manner previously described in Chapter 5. Raman spectroscopy was used to confirm that the devices studied here are single graphene layers[70]. Scanning electron microscope images of devices after measurement and raman spectra of graphene used for identification are shown in Fig. 6.1. All measurements were performed in a vacuum of 10^{-6} Torr. Back gate voltages were applied using batteries and a variable resistive divider (potentiometer). Source-drain currents of 30 nA were used between the outer probes. A low noise voltage amplifier whose noise floor was 4e-9 V/√Hz was used to amplify the voltage signal detected between the source-drain inner probes before the signal was sent to a Stanford research systems FFT spectrum analyzer (model 760). Each recorded spectrum was the running average of 2000 or more spectra. Spectra were recorded from 1-400 Hz in 1 Hz intervals.

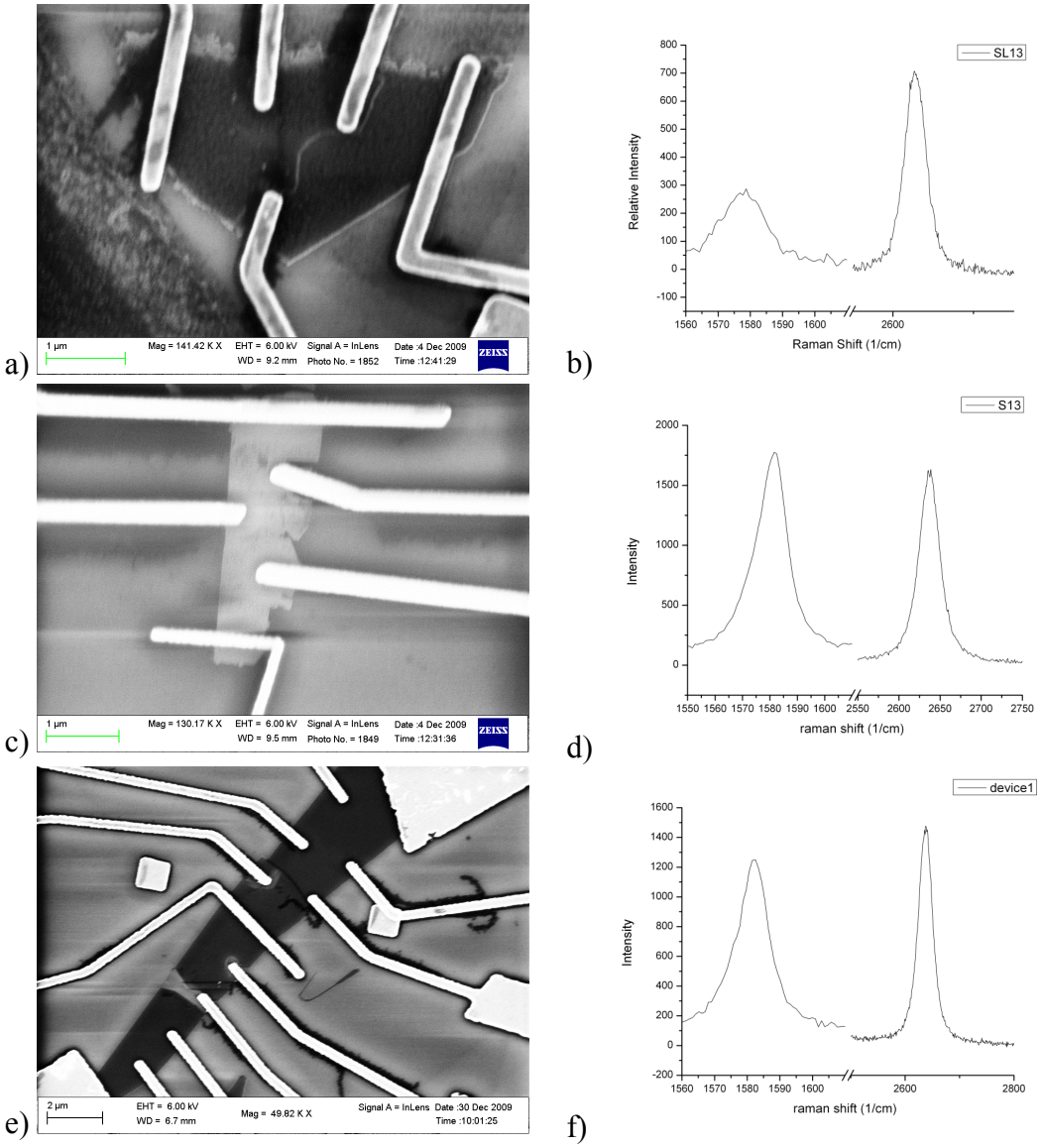

Figure 6.1: SEM images and Raman spectra of graphene devices with mobilities (a-b) 500, (c-d) 3400, (e-f) and 6800 cm^2/Vs.

Fig. 6.2 shows the four-probe conductivity $\sigma = GL/W$ as a function of gate voltage for all graphene devices studied. Three devices were studied; the mobilities of Samples 1-3 were approximately 500, 3400, and 6800 cm^2/Vs, respectively. The CNP occurs at a gate voltage $V_{g,CNP}$ of 11, 3, and 1 V for Samples 1-3 respectively. We verified that the noise is proportional to V^2 by measuring S and the average voltage V at multiple source-drain currents for all devices as shown in Fig. 6.3.

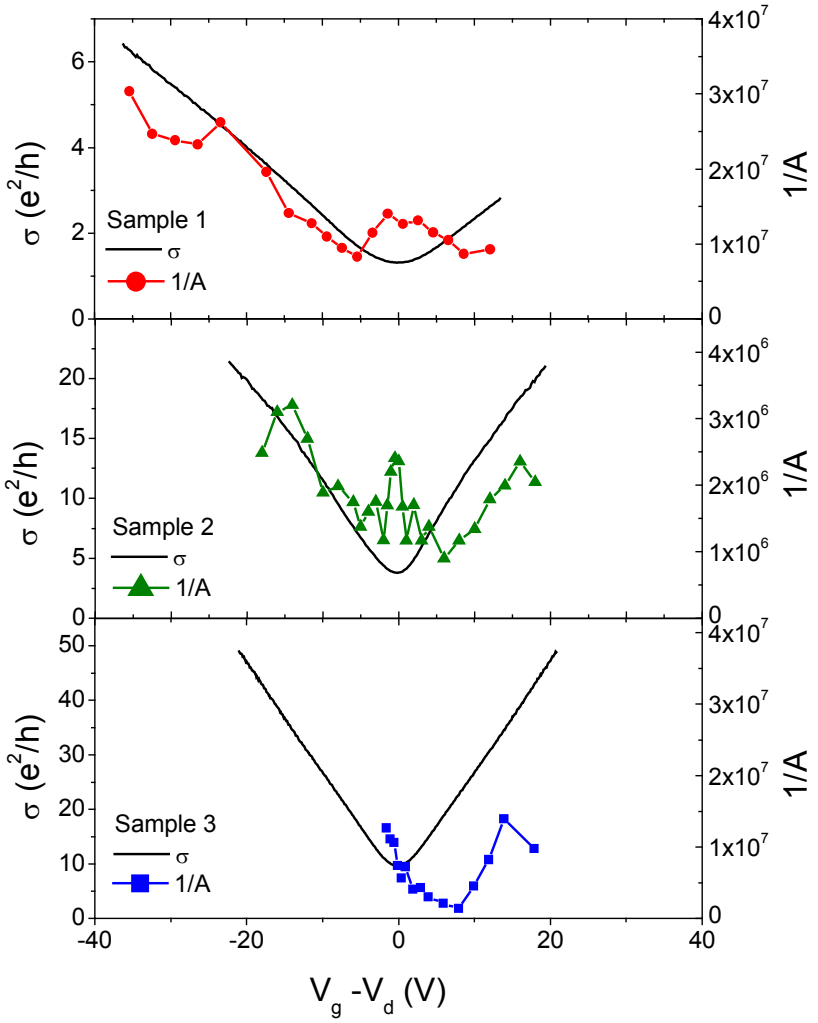

Figure 6.2: Four probe measurements of the conductivity (black line) and inverse of the noise magnitude (colored dashed line) graphene devices. Corresponding device mobilities are (a) 500 cm^2/Vs, (b) 3400 cm^2/Vs, and (c) 6800 cm^2/Vs.

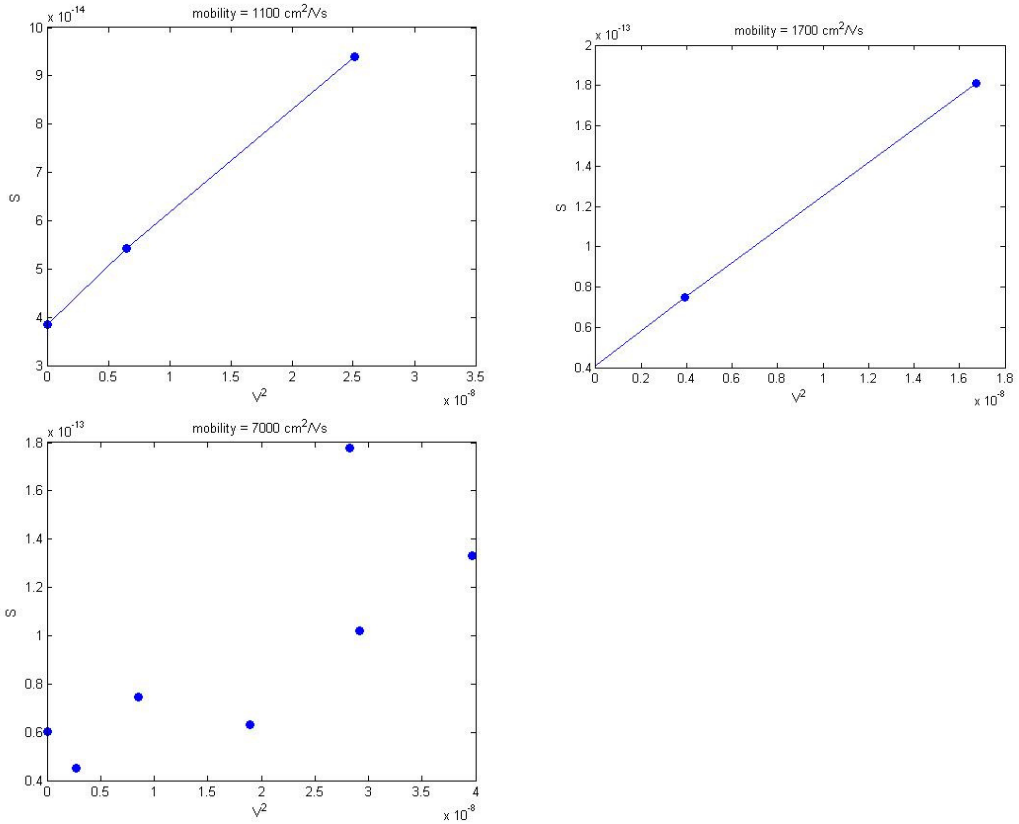

Figure 6.3: Power spectral density and average source-drain voltage were measured at different source-drain currents for each device. The y-axis, *S*, is *S(0 Hz)* or A, as explained in the text.

Since the noise was not zero at $V = 0$ as seen in Fig. 6.3, a noise spectrum was measured at source drain currents of 30 nA and 0 nA at each gate voltage, and the difference was taken to be $S_V(f)$. The average voltage V was measured simultaneously and used to normalize the noise power to obtain S_V/V^2. The noise floor of the experimental setup is reached at frequencies greater than approximately 100 Hz. The noise power A was found by fitting the data in the range of 1-50 Hz to equation 6.1 with the exponent $\beta = 1$ to ensure all A had the same units.

6.4 Discussion of Low Frequency Noise in Graphene at Room Temperature

Figure 6.2 shows the inverse of the noise magnitude $1/A$ as a function of gate voltage measured from the CNP, $V_g - V_{g,CNP}$, for all three graphene devices as well as

the conductivity of each device (black line). All devices show the same trend in 1/A; a "W" shaped curve with a local maximum centered at the $V_g = V_{g,CNP}$. For all devices, at high carrier concentration the inverse noise magnitude is linear. Hooge's law (Eqn. 6.3) accurately describes this linear behavior that occurs at approximately $|V_g - V_{g,CNP}| > 5$ V. At these carrier concentrations the mechanism dominating conduction is charged impurity scattering, which is also the mechanism in most semiconductors and metals.

At low carrier concentrations all devices have a finite peak in inverse noise magnitude at the CNP. Though Hooge's law describes high carrier concentration behavior well, it predicts that as $V_g - V_{g,CNP} \Rightarrow 0$, $1/A \Rightarrow 0$. Carrier-number fluctuations (Eqn. 6.4) predict $1/A \Rightarrow \infty$ as $V_g \Rightarrow 0$, since $\frac{d \ln G}{dV_g} = 0$ by definition at the CNP. This is in contrast to the finite noise magnitude *1/A* measured at all carrier densities in all devices. Eqn. 6.3 also predicts a stronger dependence of *1/A* on V_g than is observed away from the CNP, i.e. for $|V_g - V_{g,CNP}| > 5$ V. Neither description explains the peak in *1/A* at low carrier concentration.

In Fig. 6.4, Hooge's constant, $\alpha = A * N$, is calculated as a function of gate voltage using the relationship $N = WLc_g|V_g - V_{g,CNP}|$ where W is the device width, L the device length, and $c_g = 1.15 \times 10^{-8}$ F/cm^2 is the gate capacitance per unit area.. At high carrier concentrations agreement with Hooge's law (Eqn. 6.3) can easily be observed. In fact, for lower mobility samples, Hooge's constant at these concentrations is similar to Hooge's proposed canonical constant value of 2×10^3. At lower carrier concentrations Hooge's constant no longer fluctuates around an average value and disagreement with this description is again evident.

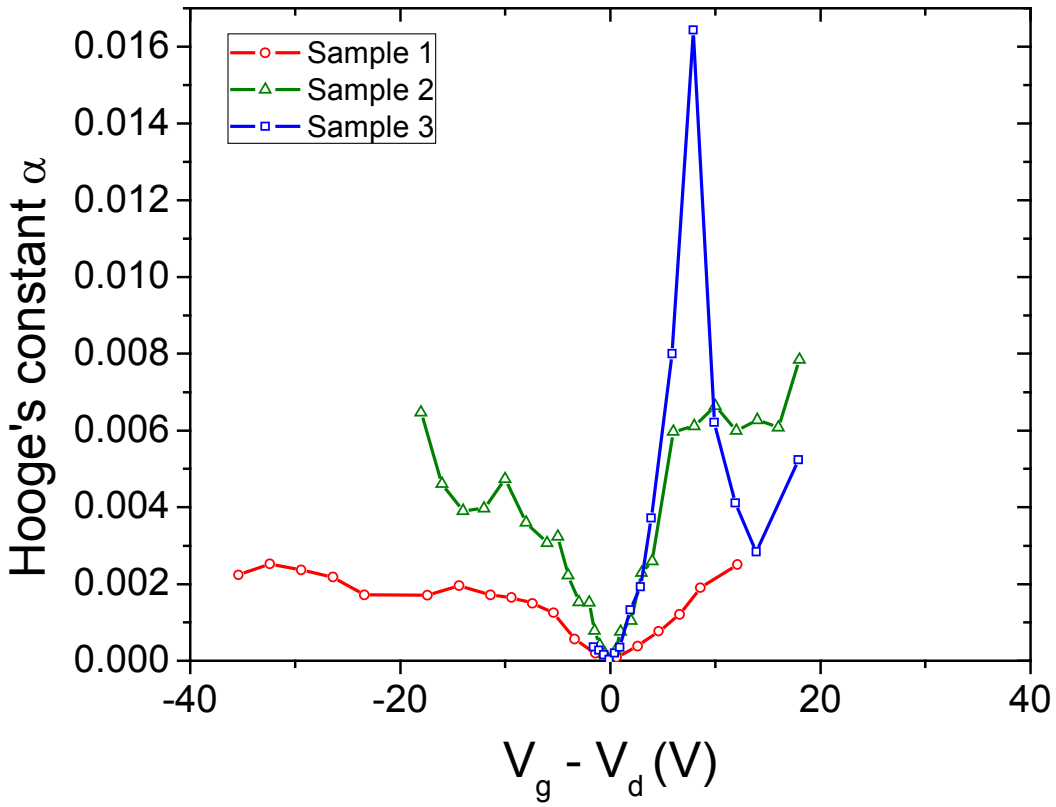

Figure 6.4: Hooge's constant as a function of gate voltage, or carrier density, for all graphene devices.

Graphene's conductivity at low carrier concentrations also differs from theoretical expectations. A number of physical descriptions have been proposed to explain the unexpected finite minimum conductivity of graphene. These descriptions rely on a finite carrier concentration induced by disorder in graphene. Disorder due to charged impurities at the SiO_2 surface[118] can explain the magnitude of the mobility in graphene[63,119], the minimum conductivity value[63,120],and the fluctuations in surface potential in graphene observed in scanned probe experiments[121],[122],[123] . Lin and Avouris[112] attempted to understand the non-divergent noise amplitude in graphene by assuming that the conductivity G was proportional to the carrier number N; then $A \sim$

$1/G$ which is not divergent since G remains non-zero at all Vg. However, this cannot explain the non-monotonic behavior of A(Vg).

I explore the possibility that the $1/f$ noise arises from random redistributions of the charged impurities near graphene; this is reasonable since even at room temperature graphene's resistivity is dominated by charged impurity scattering[73]. Rossi et al. have done extensive simulations to provide a microscopic description of the electron-hole puddles in graphene that accurately predict graphene's minimum conductivity at the CNP[124]. The simulation is performed on a piece of graphene on a 300 nm SiO_2 substrate with a back gate[124]. A random charge distribution is created a distance d below the graphene, in the SiO_2, and many charge distributions are averaged to determine general graphene behavior[124]. The charge distribution yields a potential, V_{sc}, which is used in the Thomas-Fermi-Dirac approximation to calculate the ground state carrier density $n(r)$ [124]. The conductance, G, can be calculated by solving the Schrodinger equation for the Dirac Hamiltonian defined by V_{sc}[124].

The RMS resistance for different random charge configurations, $(\delta R)^2 \equiv \langle R^2 \rangle - \langle R \rangle^2$, may be calculated using this simulation result. Here I assume that the resistance noise, S_R is proportional to $(\delta R)^2$, and A is proportional to $(\delta R)^2/R^2$. $(\delta R)^2/R^2$ was simulated by Rossi using this electron-hole puddle model for charge impurity densities of 6.8×10^{11} and 4.3×10^{12} cm^{-2}, which corresponds to the mobilities of 3200 and 1200 cm^2/Vs respectively. The simulated conductivity and the simulated $[(\delta R)^2/R^2]^{-1}$ (which we identify with the inverse noise power) are shown in Figure 6.5 (a) and (b). The simulations reproduce qualitatively the main features of the experimental data: $[(\delta R)^2/R^2]^{-1}$ is roughly linear in carrier number at high carrier

number, and $[(\delta R)^2/R^2]^{-1}$ shows a deviation from Hooge's law behavior at low carrier number in a region of V_g that is larger than the minimum conductivity region. For higher mobility simulations, a clear peak in $1/A$ is observed at the CNP similar to the measured results.

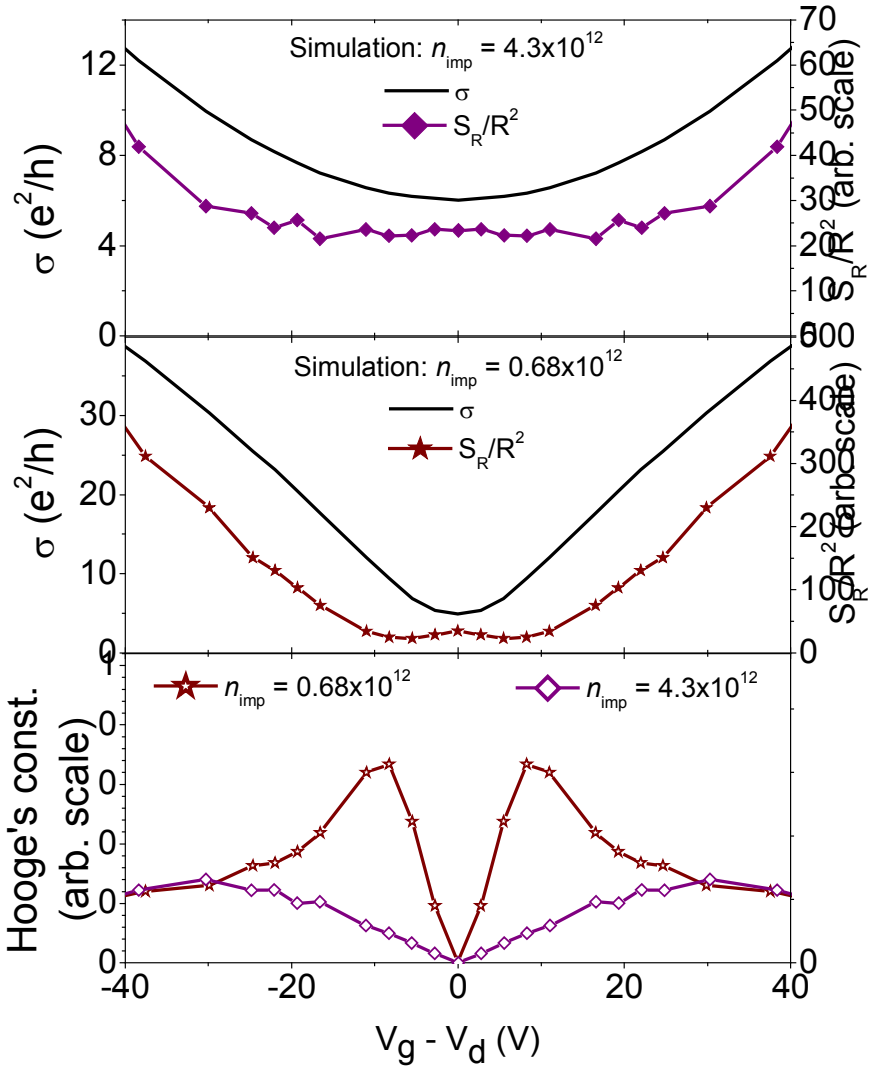

Figure 6.5: Electron-hole puddle simulation results for conductivity and $(\delta R)^2 \equiv \langle R^2 \rangle - \langle R \rangle^2$ which is equated to noise magnitude, A, for devices with mobilities (a) 1200 cm^2/Vs and (b) 3200 cm^2/Vs. (c) Hooge's constant calculated for simulated devices shown in (a) and (b).

Fig. 6.5 (c) shows the simulated gate voltage dependence of $[(\delta R)^2/R^2]n$, where n is the carrier density in the simulation, which I hypothesize should be proportional to Hooge's constant A/N. Again the simulations shows the same major features as the experiment (Fig. 6.2). $[(\delta R)^2/R^2]/n$ is depressed around the CNP, and almost constant at higher carrier concentrations. For the higher mobility simulation a peak in $[(\delta R)^2/R^2]/n$ is observed at intermediate carrier concentration, similar to the experimental data for high mobility Sample 3.

The results suggest that the major features of the experimental dependence of the $1/f$ noise magnitude on gate voltage are reproduced by the simulated fluctuations in the resistance due to random charged impurity positions in graphene. This naturally explains the finite noise magnitude at the CNP. We have also performed semi-classical simulations[64] of the resistance fluctuations due to different random charged impurity potentials using effective medium theory, with qualitatively similar results. However, the semi-classical simulations fail to reproduce the peak in $1/A$ at the CNP. This indicates that charge inhomogeneity alone cannot explain the non-monotonic dependence of noise magnitude on carrier density[116]. Surprisingly, this suggests that quantum interference effects within the puddle length scale could be important in determining the details of the noise at low carrier concentrations. The importance of quantum interference at room temperature is surprising, however phase coherent transport in graphene over the puddle length scale (~20 nm) is expected at room temperature given the low-electron-phonon and electron-electron scattering rates[125].

6.4 Temperature Dependence of the Noise

Power spectral density was measured at temperatures from 4-296 K for Sample 2, the 3400 cm^2/Vs mobility graphene device. All measurements were performed in high vacuum of 10^{-6} Torr or less (at lower temperatures pressures were as low as 10^{-7} Torr). Electronics setup and measurements were performed in the same manner as room temperature setup and measurements.

To verify the noise was *1/f* in form at all temperatures, S was compared to V^2 (at zero gate voltage) as shown in Fig. 6.6 (a). Fig. 6.6 (a) indicates that there is less scatter in the linear relationship between S and V^2 and a general decrease in noise magnitude as temperature increases. A linear fit was performed to all data sets shown in Fig. 6.6 (a). Some fit parameters are compared in Fig. 6.6 (b). At temperatures below 50 K the background noise, or noise at zero source-drain current as given by the fit, was found to be orders of magnitude larger than noise at higher temperatures. The sum of the deviation of all measured power spectral density from the best fit value, $\sum (S(0Hz)_{fit} - S(0Hz)_{measured})^2$, is shown on the right y-axis of Fig. 6.6 (b) and can be used to evaluate the goodness of the linear fit. This distribution more rigorously confirms the observation that there is more scatter in the data taken at temperatures below 50 K.

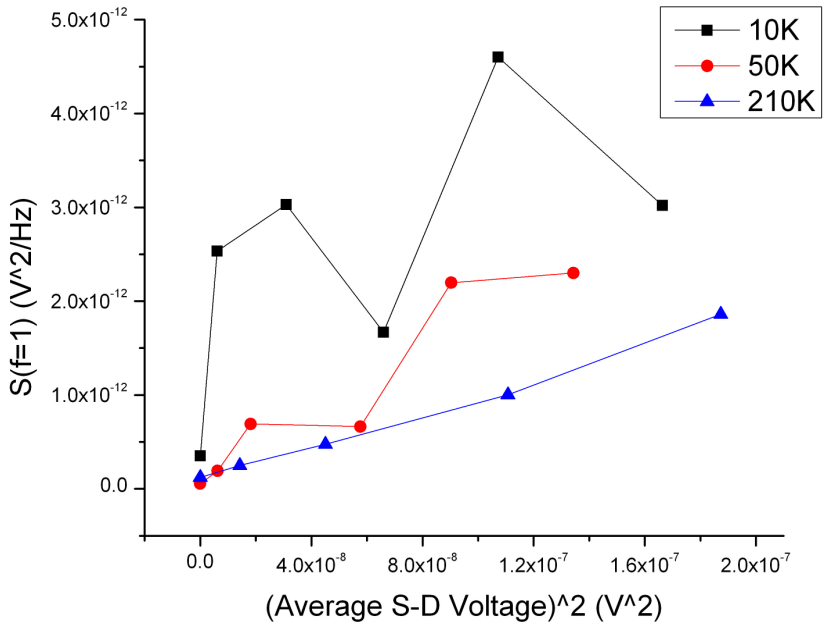

a)

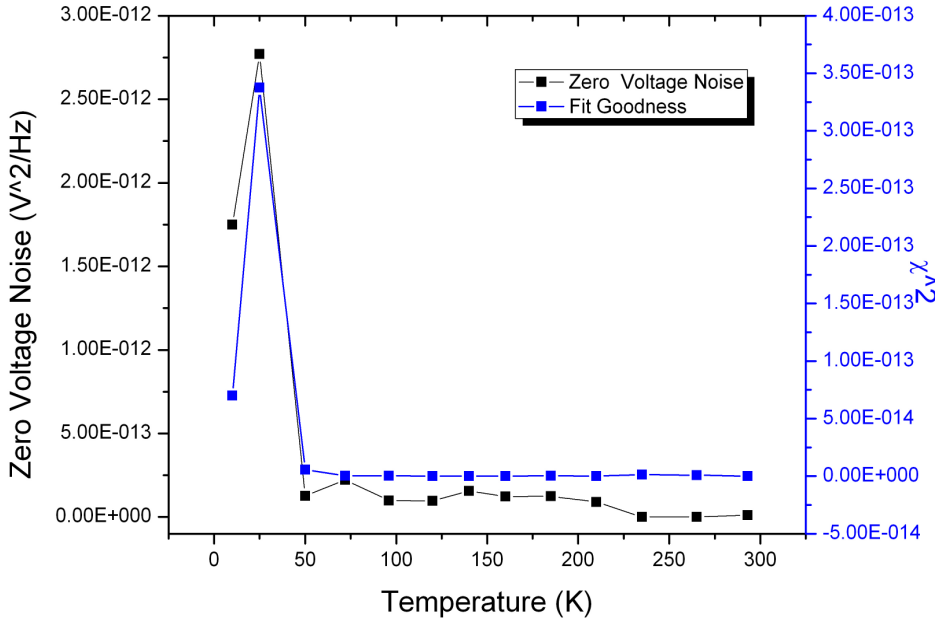

b)

Figure 6.6: (a) Four-probe measurement of power spectral density and average voltage at 10 nA current intervals for graphene device with 3400 cm^2/Vs mobility. (b) Linear fits were performed on data shown in (a) and the intercepts and total deviation of data from fit, $\sum (S(0Hz)_{fit} - S(0Hz)_{measured})^2$, are plotted as a function of temperature as the black and blue data respectively

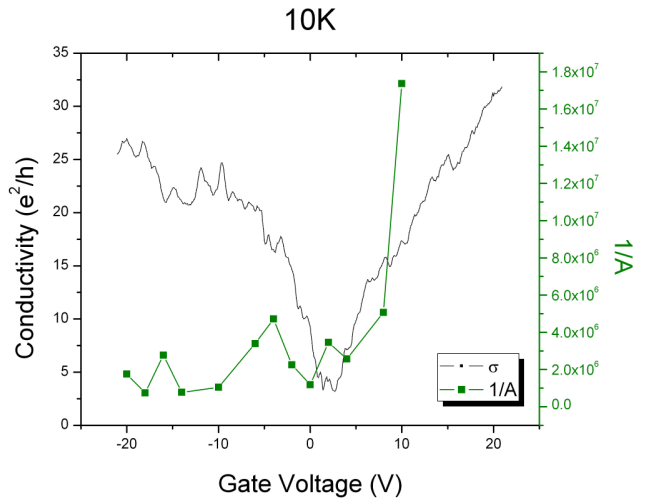

a)

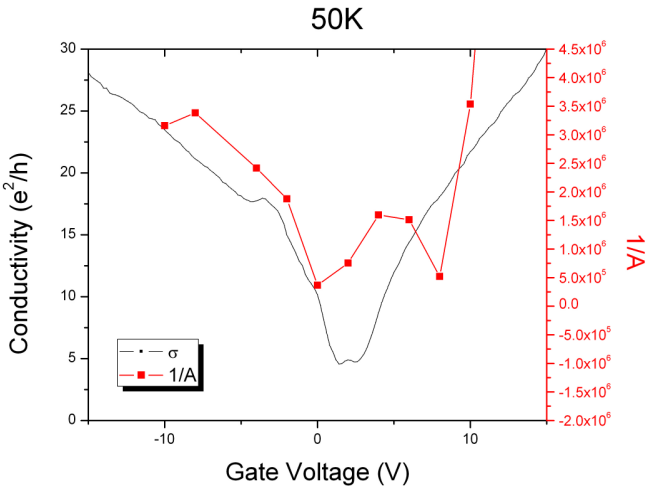

b)

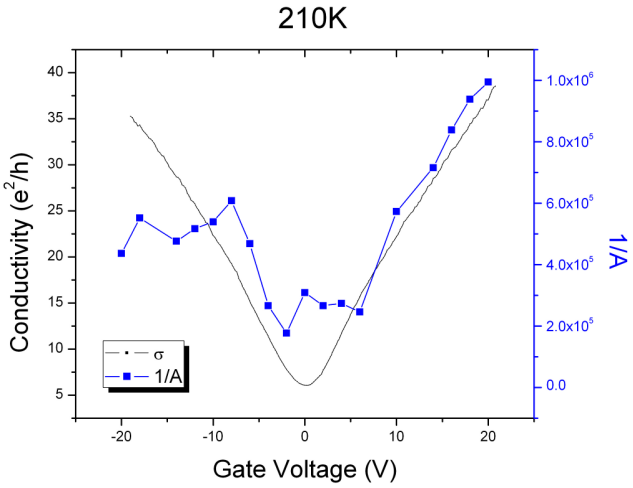

c)

Figure 6.7: Four probe measurements of the conductivity (black line) and inverse of the noise magnitude (colored dashed line) for graphene with mobility 3400 cm^2/Vs at temperatures (a) 10 K, (b) 50 K, and (c) 210 K.

In Figure 6.7 graphene conductivity is compared to inverse noise magnitude as a function of carrier number for 3 different temperatures for the 3400 cm^2/Vs mobility device. For measurements taken at 50 K and higher, the relationship between inverse noise magnitude and conductivity remains the same as it is at room temperature. The noise magnitude deviates from Hooge's law over a larger gate voltage range (approximately 10 V) than does the minimum conductivity plateau (approximately 3 V). At high carrier concentrations, or high gate voltages, the inverse noise magnitude is proportional to conductance, $1/A \sim G$, as it is at room temperature. There is no trend between noise magnitude at the CNP and temperature; the average minimum noise magnitude over all temperatures is 6×10^5 for this device. A trend may appear if noise is measured at closer intervals than 2 gate volts since dA/dV_g is large near the CNP. Simulations have not been performed at a variety of temperatures.

Both noise and conductivity data (Fig 6.7 and 5.12) taken below 50 K are significantly noisier than data taken at higher temperatures. Therefore, these measurement errors are most likely systematic. The probes in the low temperature probestation are on long arms that are mounted to the sample stage. The metal stage is cooled by liquid nitrogen flowing below it. The arms of the probes may exhibit temperature fluctuations that cause physical motion and make it impossible to perform sensitive measurements. Data below 50 K is not considered reliable.

6.5 Conclusions

In this chapter, we have measured power spectral density in multiple graphene FETs in four-probe configuration at low frequencies. The noise magnitude's

dependence on number of carriers cannot be explained by mobility fluctuations (Hooge's law) or carrier-number fluctuations. Instead, we find that a microscopic model of fluctuating charged impurities accurately depicts the non-monotonic dependence of the noise magnitude on carrier density. This observation provides additional evidence that electronic transport in graphene near the charge neutrality point is characterized by electron and hole puddles caused by the random Coulomb potential due to trapped charges near the surface of silicon dioxide.

Appendix A - Abbreviations

Bibliography

1

2 (Pew's Charitable Trust), Vol. 2010.

3 L. D. Whitmire and F. R. Brotzen, "Effects of Deformation on Electrical Resistivity of Molybdenum Single Crystals," Transactions of the Metallurgical Society of Aime **239** (6), 824-& (1967).

4 C. D. Cheng, R. K. Gonela, Q. Gu et al., "Self-assembly of metallic nanowires from aqueous solution," Nano Lett. **5** (1), 175-178 (2005).

5 Y. Naitoh, M. Horikawa, T. Yatabe et al., "A simple procedure for fabricating molecular-sized gap junctions using conventional photolithography," Nanotechnology **17** (9), 2406-2410 (2006).

6 F. Q. Fan and K. J. Stebe, "Assembly of colloidal particles by evaporation on surfaces with patterned hydrophobicity," Langmuir **20** (8), 3062-3067 (2004).

7 S. Valizadeh, M. Abid, F. Hernandez-Ramirez et al., "Template synthesis and forming electrical contacts to single Au nanowires by focused ion beam techniques," Nanotechnology **17** (4), 1134-1139 (2006).

8 P. A. Smith, C. D. Nordquist, T. N. Jackson et al., "Electric-field assisted assembly and alignment of metallic nanowires," Appl. Phys. Lett. **77** (9), 1399-1401 (2000).

9 J. J. Boote and S. D. Evans, "Dielectrophoretic manipulation and electrical characterization of gold nanowires," Nanotechnology **16** (9), 1500-1505 (2005).

10 Y. L. Liu, J. H. Chung, W. K. Liu et al., "Dielectrophoretic assembly of nanowires," J. Phys. Chem. B **110** (29), 14098-14106 (2006).

11 H. H. Cheng, C. N. Andrew, and M. M. Alkaisi, "The fabrication and characterisation of metallic nanotransistors," Microelectron. Eng. **83** (4-9), 1749-1752 (2006).

12 M. Paunovic, *Fundamentals of Electrochemical Deposition*. (Wiley-Interscience, Hoboken NJ, 2006).

13 G. Sauer, G. Brehm, S. Schneider et al., "Highly ordered monocrystalline silver nanowire arrays," Journal of Applied Physics **91** (5), 3243-3247 (2002).

14 J. G. Wang, M. L. Tian, T. E. Mallouk et al., "Microtwinning in template-synthesized single-crystal metal nanowires," J. Phys. Chem. B **108** (3), 841-845 (2004).

15 Neil; Mermin Ashcroft, N. David, *Solid State Physics*. (Thomson Learning Inc., 1976), pp.481-486.

16 Vol. 2006.

17 S. M. Sze, *VLSI Technology*. (McGraw Hill, New York, 1983).

18 S. Iijima, "Helical Microtubules of Graphitic Carbon," Nature **354** (6348), 56-58 (1991).

19 *Science of Fullerenes and Carbon Nanotubes*. (Academic Press, San Diego, 1996).

20 E. N. Konyushenko, J. Stejskal, M. Trchova et al., "Multi-wall carbon nanotubes coated with polyaniline," Polymer **47** (16), 5715-5723 (2006); S. A.

Curran, D. H. Zhang, W. T. Wondmagegn et al., "Dynamic electrical properties of polymer-carbon nanotube composites: Enhancement through covalent bonding," J. Mater. Res. **21** (4), 1071-1077 (2006).

[21] M. J. O'Connell, P. Boul, L. M. Ericson et al., "Reversible water-solubilization of single-walled carbon nanotubes by polymer wrapping," Chem. Phys. Lett. **342** (3-4), 265-271 (2001).

[22] W. G. Cullen, B.R Conrad, B. C. Riddick, E. D. Williams, Surf. Sci. (2008).

[23] S. E. Fritz, T. W. Kelley, and C. D. Frisbie, "Effect of dielectric roughness on performance of pentacene TFTs and restoration of performance with a polymeric smoothing layer," J. Phys. Chem. B **109** (21), 10574-10577 (2005).

[24] M. Ishigami, J. H. Chen, W. G. Cullen et al., "Atomic structure of graphene on SiO2," Nano Lett. **7** (6), 1643-1648 (2007).

[25] P. Blake, E. W. Hill, A. H. C. Neto et al., "Making graphene visible," Appl. Phys. Lett. **91** (6) (2007).

[26] A. Cortijo and M. A. H. Vozmediano, "Electronic properties of curved graphene sheets," Epl **77** (4), 47002-p47001:47002-p47005 (2007); F. de Juan, A. Cortijo, and M. A. H. Vozmediano, "Charge inhomogeneities due to smooth ripples in graphene sheets," Phys. Rev. B **76** (16) (2007); M. H. Gass, U. Bangert, A. L. Bleloch et al., "Free-standing graphene at atomic resolution," Nat. Nanotechnol. **3** (11), 676-681 (2008).

[27] N. Abedpour, M. Neek-Amal, R. Asgari et al., "Roughness of undoped graphene and its short-range induced gauge field," Phys. Rev. B **76** (19), 195407-195401:195407-195405 (2007).

[28] F. Guinea, B. Horovitz, and P. Le Doussal, "Gauge field induced by ripples in graphene," Phys. Rev. B **77** (20), 205421-205421:205421-205428 (2008).

[29] M. I. Katsnelson and A. K. Geim, "Electron scattering on microscopic corrugations in graphene," Philos. Trans. R. Soc. A-Math. Phys. Eng. Sci. **366** (1863), 195-204 (2008).

[30] M. Moura R.C. Thompson-Flagg, and M. Marder, "Rippling of Graphene," (2008); O. Pierre-Louis, "Adhesion of membranes and filaments on rippled surfaces," Phys. Rev. E **78** (2), 021603-021601:021603-021614 (2008).

[31] P. O. Hahn and M. Henzler, "The Si-Sio2 Interface - Correlation of Atomic-Structure and Electrical-Properties," J. Vac. Sci. Technol. A-Vac. Surf. Films **2** (2), 574-583 (1984); O. Jusko, P. Marienhoff, and M. Henzler, "Regular Step Arrays at the Sio2/Si(111) Interface," Appl. Surf. Sci. **40** (4), 295-302 (1990); Y. Homma, M. Suzuki, and N. Yabumoto, "Observation of Atomic Step Morphology on Silicon-Oxide Surfaces," J. Vac. Sci. Technol. A-Vac. Surf. Films **10** (4), 2055-2058 (1992); M. Gotoh, K. Sudoh, H. Itoh et al., "Analysis of SiO2/Si(001) interface roughness for thin gate oxides by scanning tunneling microscopy," Appl. Phys. Lett. **81** (3), 430-432 (2002).

[32] L. Brugemann, R. Bloch, W. Press et al., "Surface and Interface Topography of Amorphous Sio2 Crystalline Si(100) Studied by X-Ray-Diffraction," J. Phys.-Condes. Matter **2** (45), 8869-8879 (1990).

[33] M. Suzuki, Y. Kudoh, Y. Homma et al., "Monoatomic Step Observation on Si(111) Surfaces by Force Microscopy in Air," Appl. Phys. Lett. **58** (20), 2225-2227 (1991); M. Suzuki, Y. Homma, Y. Kudoh et al., "Roughness

Evaluation of Thermally Oxidized Si(111) Surfaces by Scanning Force Microscopy," Jpn. J. Appl. Phys. Part 1 - Regul. Pap. Short Notes Rev. Pap. **32** (3B), 1419-1422 (1993); R. Hasunuma, J. Okamoto, N. Tokuda et al., "Nommiformity in ultrathin SiO2 on Si(111) characterized by conductive atomic force microscopy," Jpn. J. Appl. Phys. Part 1 - Regul. Pap. Short Notes Rev. Pap. **43** (11B), 7861-7865 (2004).

[34] G. J. Pietsch, U. Kohler, O. Jusko et al., "Structure of the Stepped Si/Sio2 Interface after Thermal-Oxidation - Investigations with Scanning Tunneling Microscopy and Spot-Profile Analysis of Low-Energy Electron-Diffraction," Appl. Phys. Lett. **60** (11), 1321-1323 (1992).

[35] V. Tsai, X. S. Wang, E. D. Williams et al., "Conformal oxides on Si surfaces," Appl. Phys. Lett. **71** (11), 1495-1497 (1997).

[36] J. L. Goldberg, X. S. Wang, N. C. Bartelt et al., "Surface Height Correlation-Functions of Vicinal Si(111) Surfaces Using Scanning Tunneling Microscopy," Surf. Sci. **249** (1-3), L285-L292 (1991).

[37] M. S. Hoogeman, M. A. J. Klik, D. C. Schlosser et al., "Real-space measurement of surface roughening," Phys. Rev. Lett. **82** (8), 1728-1731 (1999); M. S. Hoogeman, M. A. J. Klik, D. C. Schlosser et al., "An experimental verification of the theory of surface roughening from a quantitative STM study," Surf. Sci. **448** (2-3), 142-154 (2000).

[38] H. Minoda, I. Morishima, M. Degawa et al., "Time evolution of DC heating-induced in-phase step wandering on Si(111) vicinal surfaces," Surf. Sci. **493** (1-3), 487-493 (2001); P. D. Szkutnik, D. Sander, F. Dulot et al., "Scanning tunneling microscopy study of the stability of nanostructures on Si(111) at elevated temperature," Surf. Sci. **507**, 615-618 (2002); P. D. Szkutnik, D. Sander, F. Dulot et al., "Controlled tuning of periodic morphologies on vicinal Si(111) surfaces," J. Vac. Sci. Technol. B **20** (3), 960-963 (2002).

[39] Y. N. Yang and E. D. Williams, "The Role of Carbon in the Faceting of Silicon Surfaces on the (111) to (001) Azimuth," J. Vac. Sci. Technol. A-Vac. Surf. Films **8** (3), 2481-2488 (1990).

[40] W. G. Cullen B.R Conrad, B. C. Riddick, E. D. Williams, Surf. Sci. (2008).

[41] K. Thurmer, E. D. Williams, and J. E. Reutt-Robey, "Dewetting dynamics of ultrathin silver films on Si(111)," Phys. Rev. B **68** (15) (2003).

[42] J. Krim and G. Palasantzas, "Experimental-Observations of Self-Affine Scaling and Kinetic Roughening at Submicron Lengthscales," Int. J. Mod. Phys. B **9** (6), 599-632 (1995).

[43] K. R. Bray and G. N. Parsons, "Surface transport kinetics in low-temperature silicon deposition determined from topography evolution," Phys. Rev. B **65** (3) (2002).

[44] G. Palasantzas and J. Krim, "Effect of the Form of the Height-Height Correlation-Function on Diffuse-X-Ray Scattering from a Self-Affine Surface," Phys. Rev. B **48** (5), 2873-2877 (1993).

[45] J. Krim, I. Heyvaert, C. Vanhaesendonck et al., "Scanning Tunneling Microscopy Observation of Self-Affine Fractal Roughness in Ion-Bombarded Film Surfaces," Phys. Rev. Lett. **70** (1), 57-60 (1993).

[46] E.A. Kim and A.H. Castro Neto, "Graphene as an electronic membrane," (2007); F. Guinea, M. I. Katsnelson, and M. A. H. Vozmediano, "Midgap states and charge inhomogeneities in corrugated graphene," Phys. Rev. B **77** (7) (2008).

[47] K. Sudoh, H. Iwasaki, and E. D. Williams, "Facet growth due to attractive step-step interactions on vicinal Si(113)," Surf. Sci. **452** (1-3), L287-L292 (2000).

[48] S. P. Garcia, H. L. Bao, and M. A. Hines, "Etchant anisotropy controls the step bunching instability in KOH etching of silicon," Phys. Rev. Lett. **93** (16) (2004); F. S. S. Chien, W. F. Hsieh, S. Gwo et al., "Characterization of prototype silicon pitch artifacts fabricated by scanning probe lithography and anisotropic wet etching," J. Vac. Sci. Technol. B **23** (1), 66-71 (2005).

[49] T. Kwon, R. J. Phaneuf, and H. C. Kan, "Length-scale dependence of the step bunch self-organization on patterned vicinal Si(111) surfaces," Appl. Phys. Lett. **88** (7) (2006).

[50] L. M. Malard, M. A. Pimenta, G. Dresselhaus et al., "Raman spectroscopy in graphene," Phys. Rep.-Rev. Sec. Phys. Lett. **473** (5-6), 51-87 (2009).

[51] K. S. Novoselov, A. K. Geim, S. V. Morozov et al., "Electric field effect in atomically thin carbon films," Science **306** (5696), 666-669 (2004).

[52] Y. B. Zhang, Y. W. Tan, H. L. Stormer et al., "Experimental observation of the quantum Hall effect and Berry's phase in graphene," Nature **438** (7065), 201-204 (2005).

[53] C. Berger, Z. M. Song, T. B. Li et al., "Ultrathin epitaxial graphite: 2D electron gas properties and a route toward graphene-based nanoelectronics," J. Phys. Chem. B **108** (52), 19912-19916 (2004).

[54] K. S. Kim, Y. Zhao, H. Jang et al., "Large-scale pattern growth of graphene films for stretchable transparent electrodes," Nature **457** (7230), 706-710 (2009).

[55] X. S. Li, W. W. Cai, J. H. An et al., "Large-Area Synthesis of High-Quality and Uniform Graphene Films on Copper Foils," Science **324** (5932), 1312-1314 (2009).

[56] P. W. Sutter, J. I. Flege, and E. A. Sutter, "Epitaxial graphene on ruthenium," Nat. Mater. **7** (5), 406-411 (2008).

[57] L. Y. Jiao, L. Zhang, X. R. Wang et al., "Narrow graphene nanoribbons from carbon nanotubes," Nature **458** (7240), 877-880 (2009).

[58] M. S. Fuhrer, C. N. Lau, and A. H. MacDonald, "Graphene: Materially Better Carbon," MRS Bull. **35** (4), 289-295.

[59] A. H. Castro Neto, F. Guinea, N. M. R. Peres et al., "The electronic properties of graphene," Rev. Mod. Phys. **81** (1), 109-162 (2009).

[60] P. R. Wallace, "The Band Theory of Graphite," Physical Review **71** (9), 622-634 (1947).

[61] R. Saito, G. Dresselhaus, and M. S. Dresselhaus, *Physical properties of carbon nanotubes*. (Imperial College Press, London, 1998).

[62] S. Y. Zhou, G. H. Gweon, and A. Lanzara, "Low energy excitations in graphite: The role of dimensionality and lattice defects," Ann. Phys. **321** (7), 1730-1746 (2006).

[63] J. H. Chen, C. Jang, S. Adam et al., "Charged-impurity scattering in graphene," Nat. Phys. **4** (5), 377-381 (2008).
[64] E. Rossi, S. Adam, and S. Das Sarma, "Effective medium theory for disordered two-dimensional graphene," Phys. Rev. B **79** (24), 245423 (2009).
[65] S. Adam, E. H. Hwang, V. M. Galitski et al., "A self-consistent theory for graphene transport," Proc. Natl. Acad. Sci. U. S. A. **104** (47), 18392-18397 (2007).
[66] J. C. Meyer, A. K. Geim, M. I. Katsnelson et al., "The structure of suspended graphene sheets," Nature **446** (7131), 60-63 (2007).
[67] H. Hibino, H. Kageshima, M. Kotsugi et al., "Dependence of electronic properties of epitaxial few-layer graphene on the number of layers investigated by photoelectron emission microscopy," Phys. Rev. B **79** (12) (2009).
[68] A. C. Ferrari, J. C. Meyer, V. Scardaci et al., "Raman spectrum of graphene and graphene layers," Phys. Rev. Lett. **97** (18) (2006).
[69] Claude; Dupont-Roc Cohen-Tannoudji, Jacques; Grynberg, Gilbert *Atom-Photon Interactions*. (John Wiley & Sons Inc., New York, NY, 1992), pp.88-90.
[70] A. C. Ferrari, J. C. Meyer, V. Scardaci et al., "Raman spectrum of graphene and graphene layers," Phys. Rev. Lett. **97** (18), 187401 (2006).
[71] L. Yan, W. T. S. Huck, and G. M. Whitesides, "Self-assembled monolayers (SAMS) and synthesis of planar micro- and nanostructures," J. Macromol. Sci.-Polym. Rev **C44** (2), 175-206 (2004).
[72] J. C. Love, L. A. Estroff, J. K. Kriebel et al., "Self-assembled monolayers of thiolates on metals as a form of nanotechnology," Chem. Rev. **105** (4), 1103-1169 (2005).
[73] J. H. Chen, C. Jang, S. D. Xiao et al., "Intrinsic and extrinsic performance limits of graphene devices on SiO2," Nat. Nanotechnol. **3** (4), 206-209 (2008).
[74] D. Janssen, R. De Palma, S. Verlaak et al., "Static solvent contact angle measurements, surface free energy and wettability determination of various self-assembled monolayers on silicon dioxide," Thin Solid Films **515** (4), 1433-1438 (2006).
[75] William A Zisman, in *Contact Angle Wettability and Adhesion*, edited by Robert F. Gould (Washington DC, 1964), pp. 1-51.
[76] F. M. Fowkes, "Attractive Forces at Interfaces," Industrial and Engineering Chemistry **56** (12), 40-& (1964).
[77] D. K. Owens and R. C. Wendt, "Estimation of Surface Free Energy of Polymers," J. Appl. Polym. Sci. **13** (8), 1741-& (1969).
[78] M. K. Chaudhury, "Interfacial interaction between low-energy surfaces," Mater. Sci. Eng. R-Rep. **16** (3), 97-159 (1996).
[79] H. Radelczuk, L. Holysz, and E. Chibowski, "Comparison of the Lifshitz-van der Waals/acid-base and contact angle hysteresis approaches for determination of solid surface free energy," J. Adhes. Sci. Technol. **16** (12), 1547-1568 (2002).

[80] Y. L. Chen, C. A. Helm, and J. N. Israelachvili, "Molecular Mechanisms Associated with Adhesion and Contact-Angle Hysteresis of Monolayer Surfaces," J. Phys. Chem. **95** (26), 10736-10747 (1991).

[81] G.T. and Gentle Barnes, I.R., *Interfacial Science*. (Oxford University Press, New York, 2005).

[82] R. V. Sedev, J. G. Petrov, and A. W. Neumann, "Effect of swelling of a polymer surface on advancing and receding contact angles," J. Colloid Interface Sci. **180** (1), 36-42 (1996); S. Varennes and H. P. Schreiber, "On origins of time-dependence in contact angle measurements," J. Adhes. **76** (4), 293-306 (2001).

[83] S. D. Evans, R. Sharma, and A. Ulman, "Contact-Angle Stability - Reorganization of Monolayer Surfaces," Langmuir **7** (1), 156-161 (1991).

[84] D. H. Kaelble, "Dispersion-Polar Surface Tension Properties of Organic Solids," J. Adhes. **2**, 66-& (1970).

[85] M. Sasou, S. Sugiyama, T. Ishida et al., "Influence of the surface free energy of silane-coupled mica substrate on the fixing and straightening of DNA," Thin Solid Films **517** (15), 4425-4431 (2009).

[86] R. R. Thomas, F. B. Kaufman, J. T. Kirleis et al., "Wettability of polished silicon oxide surfaces," J. Electrochem. Soc. **143** (2), 643-648 (1996).

[87] R. G. Frieser, "Characterization of Thermally Grown Sio2 Surfaces by Contact Angle Measurements," J. Electrochem. Soc. **121** (5), 669-672 (1974).

[88] R. Williams and A. M. Goodman, "Wetting of Thin-Layers of Sio2 by Water," Appl. Phys. Lett. **25** (10), 531-532 (1974).

[89] A. A. Bergh, "Correlation between Water Contact Angle and Kpr Adherence on Sio2 Surfaces," J. Electrochem. Soc. **112** (4), 457-& (1965); R. O. Lussow, L. H. Wirtz, and H. A. Levine, "Wettability Measurements on Rough High-Energy Surfaces," J. Electrochem. Soc. **114** (8), 877-& (1967).

[90] A. M. Stoneham and P. W. Tasker, "The wetting of oxide films on silicon and the monitoring of fixed charge," Semicond. Sci. Technol. **1** (1), 93-96 (1986).

[91] D. E. Aspnes and A. A. Studna, "Chemical Etching and Cleaning Procedures for Si, Ge, and Some Iii-V Compound Semiconductors," Appl. Phys. Lett. **39** (4), 316-318 (1981).

[92] John F; Wolstenholme Watts, John, *Introduction to Surface Analysis by XPS and AES*. (Wiley, New York, NY, 2003).

[93] H. Y. Zhang, M. L. Tan, Z. Y. Zhu et al., "Growth of self-assembled monolayer on tetrahedral amorphous carbon film coated magnetic head," Surf. Coat. Technol. **202** (15), 3451-3456 (2008).

[94] J. A. Gardella, S. A. Ferguson, and R. L. Chin, "Pi-Star[-Pi Shakeup Satellites for the Analysis of Structure and Bonding in Aromatic Polymers by X-Ray Photoelectron-Spectroscopy," Appl. Spectrosc. **40** (2), 224-232 (1986).

[95] Charles D; Naumkin Wagner, Alexander V; Kraut-Vass, Anna; Allison, Juanita W; Powell, Cedric J; and Rumble, John R. Jr. , (2003).

[96] M. Fujii, S. Sugisawa, K. Fukada et al., "Packing of Hydrocarbon and Perfluorocarbon Chains Planted on Oxidized Surface of Silicon as Studied by Ellipsometry and Atomic-Force Microscopy," Langmuir **10** (4), 984-987 (1994).

[97] D. J. Yun and S. W. Rhee, "Self-assembled monolayer formation on molybdenum with octadecyltrichlorosilane and phenethyltrichlorosilane and measurement of molybdenum-pentacene interface properties," J. Electrochem. Soc. **155** (6), H357-H362 (2008).
[98] *CRC Handbook of Chemistry and Physics*, 91st ed. (2011).
[99] Q. L. Gu and X. H. Cheng, "Tribological behaviors of self-assembled 3-aminopropyltriethoxysilane films on silicon," Curr. Appl. Phys. **8** (5), 583-588 (2008).
[100] J. Yan, Y. B. Zhang, P. Kim et al., "Electric field effect tuning of electron-phonon coupling in graphene," Phys. Rev. Lett. **98** (16) (2007).
[101] S. Pisana, M. Lazzeri, C. Casiraghi et al., "Breakdown of the adiabatic Born-Oppenheimer approximation in graphene," Nat. Mater. **6** (3), 198-201 (2007).
[102] A. Das, S. Pisana, B. Chakraborty et al., "Monitoring dopants by Raman scattering in an electrochemically top-gated graphene transistor," Nat. Nanotechnol. **3** (4), 210-215 (2008).
[103] E. Rossi and S. Das Sarma, "Ground State of Graphene in the Presence of Random Charged Impurities," Phys. Rev. Lett. **101** (16), 166803 (2008).
[104] S. V. Morozov, K. S. Novoselov, M. I. Katsnelson et al., "Giant intrinsic carrier mobilities in graphene and its bilayer," Phys. Rev. Lett. **100** (1) (2008).
[105] P. Dutta and P. M. Horn, "Low-Frequency Fluctuations in Solids - 1-F Noise," Rev. Mod. Phys. **53** (3), 497-516 (1981).
[106] Martin von Haartman, *Low-Frequency Noise in Advanced MOS Devices*. (Springer, Dordrecht, 2007).
[107] M. Ishigami, J. H. Chen, E. D. Williams et al., "Hooge's constant for carbon nanotube field effect transistors," Appl. Phys. Lett. **88** (20) (2006).
[108] D. A. Bell, "A Survey of 1-F Noise in Electrical Conductors," Journal of Physics C-Solid State Physics **13** (24), 4425-4437 (1980).
[109] M. B. Weissman, "1/F Noise and Other Slow, Nonexponential Kinetics in Condensed Matter," Rev. Mod. Phys. **60** (2), 537-571 (1988).
[110] L. K. J. Vandamme, X. S. Li, and D. Rigaud, "1/F Noise in Mos Devices, Mobility or Number Fluctuations," IEEE Trans. Electron Devices **41** (11), 1936-1945 (1994).
[111] J. Tersoff, "Low-frequency noise in nanoscale ballistic transistors," Nano Lett. **7** (1), 194-198 (2007).
[112] Y. M. Lin and P. Avouris, "Strong suppression of electrical noise in bilayer graphene nanodevices," Nano Lett. **8** (8), 2119-2125 (2008).
[113] Q. H. Shao, G. X. Liu, D. Teweldebrhan et al., "Flicker Noise in Bilayer Graphene Transistors," IEEE Electron Device Lett. **30** (3), 288-290 (2009); G. Liu, W. Stillman, S. Rumyantsev et al., "Low-frequency electronic noise in the double-gate single-layer graphene transistors," Appl. Phys. Lett. **95** (3), 033103 (2009); G. Liu, W. Stillman, S. Rumyantsev et al., "Low-frequency electronic noise in the double-gate single-layer graphene transistors," Appl. Phys. Lett. **95** (3) (2009).
[114] A. N. Pal and A. Ghosh, "Ultralow noise field-effect transistor from multilayer graphene," Appl. Phys. Lett. **95** (8), 082105 (2009).

[115] J. Mannik, I. Heller, A. M. Janssens et al., "Charge noise in liquid-gated single-wall carbon nanotube transistors," Nano Lett. **8** (2), 685-688 (2008).
[116] Guangyu Xu, Carlos M Torres, Yuegang Zhang et al., "Effect of Spatial Charge Inhomogeneity on 1/f Noise Behavior in Graphene," Nano Lett. **10** (9) (2010).
[117] E. H. Hwang, S. Adam, and S. Das Sarma, "Carrier transport in two-dimensional graphene layers," Phys. Rev. Lett. **98** (18), 186806 (2007).
[118] S. Adam and S. Das Sarma, "Transport in suspended graphene," Solid State Commun. **146** (9-10), 356-360 (2008).
[119] C. Jang, S. Adam, J. H. Chen et al., "Tuning the effective fine structure constant in graphene: Opposing effects of dielectric screening on short- and long-range potential scattering," Phys. Rev. Lett. **101** (14), 146805 (2008).
[120] J. H. Chen, W. G. Cullen, C. Jang et al., "Defect Scattering in Graphene," Phys. Rev. Lett. **102** (23) (2009).
[121] J. Martin, N. Akerman, G. Ulbricht et al., "Observation of electron-hole puddles in graphene using a scanning single-electron transistor," Nat. Phys. **4** (2), 144-148 (2008).
[122] J. C. Meyer, C. Kisielowski, R. Erni et al., "Direct Imaging of Lattice Atoms and Topological Defects in Graphene Membranes," Nano Lett. **8** (11), 3582-3586 (2008).
[123] A. Deshpande, W. Bao, F. Miao et al., "Spatially resolved spectroscopy of monolayer graphene on SiO2," Phys. Rev. B **79** (20), 205411 (2009).
[124] E. Rossi, J. H. Bardarson, P. W. Brouwer et al., "Signatures of Klein tunneling in disordered graphene p-n-p junctions," Phys. Rev. B **81** (12), 121408 (2009).
[125] W. K. Tse, E. H. Hwang, and D. S. Sarma, "Ballistic hot electron transport in graphene," Appl. Phys. Lett. **93** (2), 023128 (2008).